Computational and Experimental Study of Instrumented Indentation

by

Nuwong Chollacoop

B.S., Materials Science and Engineering,
Brown University (1999)

Submitted to the Department of Materials Science and Engineering
in partial fulfillment of the requirements for the degree of

Doctor of Philosophy in Materials Science and Engineering

at the

MASSACHUSETTS INSTITUTE OF TECHNOLOGY

February 2004

Author .....
Department of Materials Science and Engineering
December 16, 2003

Certified by .....
Subra Suresh
Ford Professor of Engineering
Thesis Supervisor

Accepted by .....
Harry L. Tuller
Professor of Ceramics and Electronic Materials
Chair, Departmental Committee on Graduate Students

Computational and Experimental Study of Instrumented Indentation

by

Nuwong Chollacoop

Submitted to the Department of Materials Science and Engineering
on December 23, 2003, in partial fulfillment of the
requirements for the degree of
Doctor of Philosophy in Materials Science and Engineering

Abstract

The effect of characteristic length scales, through dimensional and microstructural miniaturizations, on mechanical properties is systematically investigated by recourse to instrumented micro- and/or nanoindentation. This technique is capable of extracting mechanical properties accurately down to nanometers, via rigorous interpretation of indentation response. Such interpretation requires fundamental understandings of contact mechanics and underlying deformation mechanisms. Analytical, computational and experimental approaches are utilized to elucidate specifically how empirical constitutive relation can be estimated from the complex multiaxial stress state induced by indentation. Analytical formulations form a framework for parametric finite element analysis. The algorithms are established to predict indentation response from a constitutive relation (hereafter referred to as "forward algorithms") and to extract mechanical properties from indentation curve (hereafter referred to as "reverse algorithms"). Experimental verifications and comprehensive sensitivity analysis are conducted. Similar approaches are undertaken to extend the forward/reverse algorithms to indentations using two ore more tip geometries.

Microstructural miniaturization leads to novel class of materials with a grain size smaller than 100 nm, hereafter referred to as "nanocrystalline" material. Its mechanical properties are observed to deviate greatly from the microcrystalline counterparts. In this thesis, experimental, analytical and computational approaches are utilized to elucidate the rate and size dependent mechanical properties observed in nanocrystalline materials. Indentations, as well as micro-tensile tests, are employed to attain various controllable deformation rates. A simple analytical model, hereafter referred to as Grain-Boundary-Affected-Zone (GBAZ) model, is proposed to rationalize possible rate-sensitivity mechanism. Systematic finite element analysis integrating GBAZ model is conducted with calibration against the experiments. The same GBAZ model, further utilized in the parametric finite element study, is capable of predicting the inverse Hall-Petch-type phenomenon (weakening with decreasing grain size) at the range consistent with the literature.

Thesis Supervisor: Subra Suresh
Title: Ford Professor of Engineering

Acknowledgments

"Only those who recognize help and support from others would succeed again."

my beloved parents

Every journey has to come to an end. And this is surely one of the most challenging and memorable journeys I have ever embarked on. It would not be completed without a considerable amount of help and support from everyone around me. I feel overwhelmingly grateful toward them, and this is the smallest thing I could perhaps do to show my appreciation.

First and foremost, I would like to thank my advisor, Professor Subra Suresh, for seeing the possibility in me and giving me the opportunity. His academic guidance, inspiration and consolation are well beyond my words. His endless patience and encouragement have kept me progressing throughout the up and down cycles till my success today.

Furthermore, I would like to thank Professor Merton Corson Flemings and Professor Lorna J. Gibson for dedicating their valuable times to serve on my thesis committee. Their suggestions and supports are greatly appreciated.

My former academic advisor during my undergraduate study at Brown University, Professor K. Sharvan Kumar, is the first person to expose me to this wonderfully amazing field of study and help me throughout my undergraduate study, both academically and personally. I would not be getting into MIT at the first place without him.

Next person who is solely responsible for sharpening my computer simulation skill is Dr. Ming Dao. His never-ending effort to teach me ABAQUS has never been less exciting. Long hour discussion, definitely not in the morning, has always been intellectually stimulating and challenging. He is simply the great person to work with, and it has been my pleasure to get to know and work closely with him all along my graduate study.

All members of Suresh Group (previously Laboratory for EXperimental and COmputation Micromechanics or LEXCOM) during my stay at MIT certainly make me welcomed and ever want to come to work everyday. Lab manager George LaBonte is the most knowledgeable person I have ever known when it comes down to anything hand-on. Try asking him anything and he will find the answer for you. Also, thanks for his home-grown tomatoes and occasionally home-made desserts from Doranna.

Kenneth E. Greene, Jr. is the man to ask when it comes down to administrative paper

work. He is probably the first person who can remember my long last name before my first name. His incredibly friendly personality has eased my initial transition to MIT. Our conversation prior to my meeting with Subra has been entertaining.

Professor Andrew Gouldstone is one of the most considerate, energetic and self-motivated persons I have ever known. He is not only my academic mentor but also my first and best lifting partner (except when he forces me to do squat). He has always been helping me out during my academic and personal hardships. He is the first non-Thai person that I think of when I need consultation.

Professor Krystyn J. Van Vliet has tremendously helped me with her experimental, presentation and writing skills. Her persistent academic enthusiasm and excitement have positively influenced my motivation. Also, it has been enjoyable exchanging Microsoft Excel tricks with her.

Dr. Tae-Soon Park and Dr. Yoonjoon Choi have proven my hypothesis that all Koreans work hard. Due to their typically late night staying, I often bother them with some academic questions and personal conversations. We have also shared the love for food and beer.

Timothy Hanlon is one of the most self-disciplined graduate students I have ever known. We have become so close after he has moved into the cubicle next to mine. His help in recent years is greatly appreciated, especially for making sure that I wake up in time for a morning meeting.

Professor Antonios E. Giannakopoulos, Professor T. A. Venkatesh, Dr. Yong-Nam Kwon, Dr. Benedikt Moser, Dr. Ruth Schwaiger and Professor Upadrasta Ramamurty have variously helped me in different parts of my thesis. Their intellectual contributions are greatly appreciated.

I would like to also thank Laurent Chambon, Dr. 1st Lt. Brett P. Conner, John Philip Mills, Simon C. Bellemare, Bruce Y. Wu and In-Suk Choi for their warm friendship in the basement office.

Within DMSE, Kathleen R. Farrell, Gloria Landahl, Angelita Mireles, Stephen J. Malley, Coleman Greene, Gerald Hughes, Jenna Picceri and Yinlin Xie have helped me throughout my study at MIT. Many thanks to my first year study group, Douglas Dale Cannon, Burke C. Hunsaker, Ashley P Predith and Marc Richard, who have helped me getting through all first-year courses and general written examination.

Thanks to all DMSE Thai folks−Dr. Pimpa Limthongkul, Dr. Ariya Akthakul, Dr. Yot Boontongkong, Jessada Wannasin, Panitarn Wanakamol, Ratchatee Techapiesancharoenkij, Wanida Pongsaksawad, Samerkhae Jongtammanurak and Yuttanant Boonyongmaneerat−−and other members of TSMIT (Thai Student at MIT), whose names cannot be listed here due to an insufficient space, for their moral supports throughout my graduate study.

I would like to extend my appreciation toward my Thai Scholars' 1994 friends, especially Peerapong Phimonwichayakit, Charatpong Chotigavanich, Songpon Deechongkit, Athicha Muthitacharoen, Namon Yuthavong, Mali Chivakul, Kittipitch Kuptavanich and Pitiporn Phanaphat, for making me feel warm and welcome during my first year in the United States. In addition, I would like to thank Royal Thai Government and my contract co-signers−Uncle Niwat Wachirawarakarn, Aunt Suree Khutaweekul and Arjan Komkum Deewongsa−for giving me an opportunity to study abroad.

There is no other support more meaningful than that from the family. With my deepest gratitude, I would like to thank my parents for everything they have ever done for me. Their beliefs in me have strongly encouraged me to strive for my seemingly impossible goals. They have shown me by their excellent examples of how to make everyday the best day to come, and over time have taught me how to be a better person. Their love, care and support are unconditionally abundant. They are always there throughout my miserable and exultant times. I am blessed and fortunate to have them as my parents. Mom and dad, I dedicate this thesis for you.

Next are my elder sister (P'Kung) and elder brother (P'Kai), who have always looked after me and not once hesitated to help me in any possible way. Had it not been P'Kung who spent hours after hours tutoring me during my early ages, I would not achieve this far. Her sacrifice and favor for two younger brothers have never stopped since I could remember. As for P'Kai, his astoundingly intrinsic talent and perseverance have effectively motivated me to try harder where I fail and make it happen. He is the perfect example for the phases, "Everything can be learned" or "Proper prioritization leads to success". Also, thanks to my great aunt (E'Po+) for making sure that I never go hungry with her presence.

Further thanks to Arjan Komkum Deewongsa, who is like a mother to me, for her enduring love and help since my high school year. I would never be awarded Royal Thai scholarship without her.

Last but certainly not least, I would like to specially thank my future wife, Jaturada Aksharanugraha (Bo), for allowing me to enter her life, accepting me for who I am and believing in me. Her love, understanding and sacrifice for me are beyond my words. She is every reason I open my eyes in the morning and close my eyes at night. And I am looking forward to sharing the future with her for many years to come. Also, thanks to her parents for raising such a wonderful daughter and embracing me into the family.

Contents

List of Figures

List of Tables

Chapter 1

Introduction

Current trends in the microelectronic, tribological coating and biomedical industries are driving characteristic dimensions and microstructures of engineered materials and systems down to the microscopic and nanoscopic size scales. The mechanical properties of such materials have been observed to deviate greatly from those of their conventional counterparts, ostensibly due to confined dimensions (e.g. in coating) and confined microstructures (e.g in ultra-fine crystalline and nanocrystalline materials with grain sizes of 100-1000 nm and less than 100 nm, respectively). To design the devices at this length scales against mechanical failure during fabrication and operation, their mechanical properties need to be accurately determined in a systematic manner, both prior to and during their services. Among many other mechanical testing techniques, depth-sensing instrumented indentation provides a convenient method to precisely assess the mechanical behavior of such materials, by recourse to careful interpretation of a force-depth ($P - h$) response.

Over the past few decades, indentation has rapidly gained its reputation for versatile property extraction due to its flexible specimen requirement, non-destructive testing and ability to probe localized properties. In particular, indentation has frequently proved to be the only means available to extract mechanical properties from sophisticated, constrained material systems (e.g. multilayered metallization in ultra large scale integration (ULSI) devices); novice material systems which are difficult, if not impossible, to produce in bulk quantities (e.g. nanocrystalline materials); or embedded feature in microstructure

(e.g. connecting ligaments in foam). Despite the extensive range of applications, precise interpretation of the indentation curves is necessary for this technique to become a viable method of mechanical property determination. Interpretation of such curves involves an understanding of contact mechanics and fundamental mechanisms which define the deformation behavior of the materials involved.

To this end, analytical, computational and experimental approaches are utilized to elucidate the contact mechanics complexity during indentation, specifically how empirical constitutive relation can be estimated from the intricate multiaxial stress state induced by indentation. An analytical expression for Young's modulus is further developed from solutions of an elastic half space being indented by a rigid, axially symmetric punch [1]. On the other hand, analytical expressions for plastic information rely on a self-similar solution of an elasto-plastic material under spherical indentation [2] and sharp (i.e. Vickers and Berkovich) indentation [3, 4]. Using dimensional analysis, closed-form analytical functions can be identified correlating empirical constitutive description to indentation response. Coefficients of these dimensionless functions are accurately determined by recourse to systematic finite element analysis of indentation computational modeling. Further rearrangements of these functions reveal

- forward algorithms that predict an indentation response from an empirical constitutive relation, and
- reverse algorithms that predict an empirical constitutive relations from an indentation response.

In addition, experimental indentations of materials, whose mechanical properties are known a priori, are conducted to verify the forward/reverse algorithms. Similar approaches are pursued to extend the algorithms to dual indenters or more.

In addition to dimensional miniaturization, indentation is often employed to analyze the effect of microstructural miniaturization (e.g. in ultra-fine crystalline and nanocrystalline materials). These novice material systems have been recognized for their appealing mechanical properties [5–21], such as increased yield strength/hardness/fracture strength,

superior resistance to wear/corrosion/crack initiation, and pronounced rate sensitivity (increased strength with increasing strain rate), among many others. Despite recent progress within the context of nanocrystalline materials, fundamental understandings of mechanisms underlying the mechanical properties are not clear, if not conflicting (e.g. experimental data on the strain-rate sensitivity of nanocrystalline metals by [7, 8]). Hence, quantitative conclusion cannot be drawn from the vast amount of literature data. Cautious analysis of the literature data reveals that inconsistency may arise from the different testing techniques chosen to attain various strain rates. To minimize the artifacts, rate-sensitive data should be collected from the same experimental setup.

To this end, experimental, analytical and computational approaches are utilized to elucidate the effect of rate sensitivity on the mechanical properties of nanocrystalline materials. In addition to the micro-tensile test, indentation has yet again proved ambidextrous due to its ability to vary controllable load/strain rate within the same experimental setup. A simple analytical model (called Grain-Boundary-Affected-Zone model, see Chapter 5), which is predicated upon the premise that grain boundary is atomically sharp and atoms nearby grain boundary are more likely to move, is proposed. Systematic finite element analysis integrating GBAZ model is conducted with calibration against the experiments. The properly configured GBAZ model is then rationalized for the possible mechanism governing rate-sensitivity in nanocrystalline materials. The same GBAZ model is further illustrated with the capability to predict the observed size effect, namely inverse Hall-Petch-type phenomenon (see Section 5.5), at the critical grain size range consistent with experimental and atomistic calculation results reported in the literature..

The main objective of this thesis is to use computational tool (within the context of finite element analysis), based on analytical formulations and guided by the relevant experiments, to quantify the effect of size scales on the mechanical properties. The computational modeling is focused on instrumented indentations with single or dual indenter(s), and deformation mechanism in nanocrystalline materials. The thesis is organized in the following manner:

§ Chapter 2 presents a systematic parameter study of indentation simulation within the context of finite element analysis and theoretical framework. Using dimensional

analysis, the forward and reverse algorithms are proposed with experimental verifications, and the comprehensive sensitivity analysis is conducted. Significant issues, e.g. representative strain and uniqueness of the prediction, are discussed in details.

§ Chapter 3 extends the proposed algorithms in Chapter 2 to indentation using two or more indenters, by recourse to similar approach. Improvement over single indentation algorithms is discussed with regard to uniqueness and sensitivity. Possible extension to multiple indenters algorithms is explored.

§ Chapter 4 presents the experimental assessment of the representative stresses estimated from the instrumented sharp indentation using previously proposed algorithms in Chapters 2 and 3. The representative stress concept may be utilized to construct the entire stress-strain curve, provided that multiple indentations are conducted on the target material with different levels of known plastic pre-strain.

§ Chapter 5 proposes the possible mechanism for rate-sensitivity observed in nanocrystalline materials, by recourse to systematic finite element analysis of newly developed Grain Boundary Affected Zone (GBAZ) model, whose parameters are calibrated against the experiments. The same GBAZ model is shown with consistency to size effect observed (namely inverse Hall-Petch-type phenomenon) in the literature.

§ Chapter 6 presents a summary of conclusions and discusses directions of the future work.

Chapter 2

Computational Modeling of the Forward and Reverse Problems in Instrumented Sharp Indentation

In this chapter*, a comprehensive computational study was undertaken to identify the extent to which elasto-plastic properties of ductile materials could be determined from instrumented sharp indentation and to quantify the sensitivity of such extracted properties to variations in the measured indentation data. Large deformation finite element computations were carried out for 76 different combinations of elasto-plastic properties that encompass the wide range of parameters commonly found in pure and alloyed engineering metals; Young's modulus, E, was varied from 10 to 210 GPa, yield strength, $\sigma_{\rm y}$, from 30 to 3000 MPa, and strain hardening exponent, n, from 0 to 0.5, and the Poisson's ratio, ν, was fixed at 0.3. Using dimensional analysis, a new set of dimensionless functions was constructed to characterize instrumented sharp indentation. From these functions and elasto-plastic finite element computations, analytical expressions were derived to relate indentation data to elasto-plastic properties. Forward and reverse analysis algorithms were thus established; the forward algorithms allow for the calculation of a unique indentation response for a given set of elasto-plastic properties, whereas the reverse algorithms enable the extraction

*This article is published in *Acta. Mater.*, Vol. 49 (2001), p. 3899, with co-authors: M. Dao, K. J. Van Vliet, T. A. Venkatesh and S. Suresh. [22]

of elasto-plastic properties from a given set of indentation data. A representative plastic strain ε_{r} was identified as a strain level which allows for the construction of a dimensionless description of indentation loading response, independent of strain hardening exponent n. The proposed reverse analysis provides a unique solution of the reduced Young's modulus E^*, a representative stress σ_{r}, and the hardness p_{ave}. These values are somewhat sensitive to the experimental scatter and/or error commonly seen in instrumented indentation. With this information, values of σ_{y} and n can be determined for the majority of cases considered here provided that the assumption of power law hardening adequately represents the full uniaxial stress-strain response. These plastic properties, however, are very strongly influenced by even small variations in the parameters extracted from instrumented indentation experiments. Comprehensive sensitivity analyses were carried out for both forward and reverse algorithms, and the computational results were compared with experimental data for two materials.

2.1 Introduction

The mechanical characterization of materials has long been represented by their hardness values [23, 24]. Recent technological advances have led to the general availability of depth-sensing instrumented micro- and nanoindentation experiments (e.g., [23–36]). Nanoindenters provide accurate measurements of the continuous variation of indentation load P down to micro-Newtons, as a function of the indentation depth h down to nanometers. Experimental investigations of indentation have been conducted on many material systems to extract hardness and other mechanical properties and/or residual stresses (e.g., [25–27, 31, 35–39, 43, 44], among many others).

Concurrently, comprehensive theoretical and computational studies have emerged to elucidate the contact mechanics and deformation mechanisms in order to systematically extract material properties from P versus h curves obtained from instrumented indentation (e.g., [3, 25, 27, 33, 34, 38–42]. For example, the hardness and Young's modulus can be obtained from the maximum load and the initial unloading slope using the methods suggested by Oliver and Pharr [27] or Doerner and Nix [25]. The elastic and plastic properties may be computed through a procedure proposed by Giannakopoulos and Suresh [41], and the

residual stresses may be extracted by the method of Suresh and Giannakopoulos [43, 44]. Thin film systems have also been studied using finite element computations [45–47].

Using the concept of self-similarity, simple but general results of elasto-plastic indentation response have been obtained. To this end, Hill *et al.* [2] developed a self-similar solution for the plastic indentation of a power law plastic material under spherical indentation, where Meyer's law[†] was given a rigorous theoretical basis. Later, for an elasto-plastic material, self-similar approximations of sharp (i.e., Berkovich and Vickers) indentation were computationally obtained by Giannakopoulos *et al.* [3] and Larsson *et al.* [4]. More recently, scaling functions were applied to study bulk [33, 34, 40] and coated material systems [47]. Kick's Law (i.e., $P = Ch^2$ during loading, where loading curvature C is a material constant) was found to be a natural outcome of the dimensional analysis of sharp indentation (e.g., [33]).

Despite these advances, several fundamental issues remain that require further examination:

1. A set of analytical functions, which takes into account the pile-up/sink-in effects and the large deformation characteristics of the indentation, needs to be established in order to avoid detailed FEM computations after each indentation test. These functions can be used to accurately predict the indentation response from a given set of elasto-plastic properties (forward algorithms), and to extract the elasto-plastic properties from a given set of indentation data (reverse algorithms). Giannakopoulos, Larsson and Vestergaard [3] and later Giannakopoulos and Suresh [41] proposed a comprehensive analytical framework to extract elasto-plastic properties from a single set of $P - h$ data. Their results, as will be shown later in this study, were formulated using mainly small deformation FEM results (although they performed a number of large deformation computations). Cheng and Cheng [33, 34, 40], using an included apex angle of the indenter of 68^o, proposed a set of universal dimensionless functions based on large deformation FEM computations, but did not establish a full set of closed-form analytical functions.

[†]Meyer's law for spherical indentation states that $P = \frac{Ka^m}{D^{m-2}}$, where m is a hardening factor, D is the indenter's diameter, a is the contact radius of the indenter, and K is a material constant.

2. Under what conditions and/or assumptions can a single set of elasto-plastic properties be extracted from a single $P-h$ curve with reasonable accuracy? Cheng and Cheng [40] and Venkatesh *et al.* [42] discussed this issue. However, without an accurate analytical framework based on large deformation theory, this issue can not be addressed.

3. What are the similarities and differences between the large and small deformation-based analytical formulations? Chaudhri [48] estimated that equivalent strains of 25% to 36% were present in the indented specimen near the tip of the Vickers indenter. These experimentally observed large strains justify the need for large deformation based theories in modeling instrumented sharp indentation tests.

In this paper, these issues will be addressed within the context of sharp indentation and continuum analysis.

2.2 Theoretical and Computational Considerations

2.2.1 Problem Formulation and Associated Nomenclature

Figure 2-1 shows the typical $P-h$ response of an elasto-plastic material to sharp indentation. During loading, the response generally follows the relation described by Kick's Law,

$$P = Ch^2 \tag{2.1}$$

where C is the loading curvature. The average contact pressure, $p_{\text{ave}} = \frac{P_{\text{m}}}{A_{\text{m}}}$ (A_{m} is the true projected contact area measured at the maximum load P_{m}), can be identified with the hardness of the indented material. The maximum indentation depth h_{m} occurs at P_{m}, and the initial unloading slope is defined as $\frac{\mathrm{d}P_{\text{u}}}{\mathrm{d}h}\big|_{h_{\text{m}}}$, where P_{u} is the unloading force. The W_{t} term is the total work done by load P during loading, W_{e} is the released (elastic) work during unloading, and the stored (plastic) work $W_{\text{p}} = W_{\text{t}} - W_{\text{e}}$. The residual indentation depth after complete unloading is h_{r}.

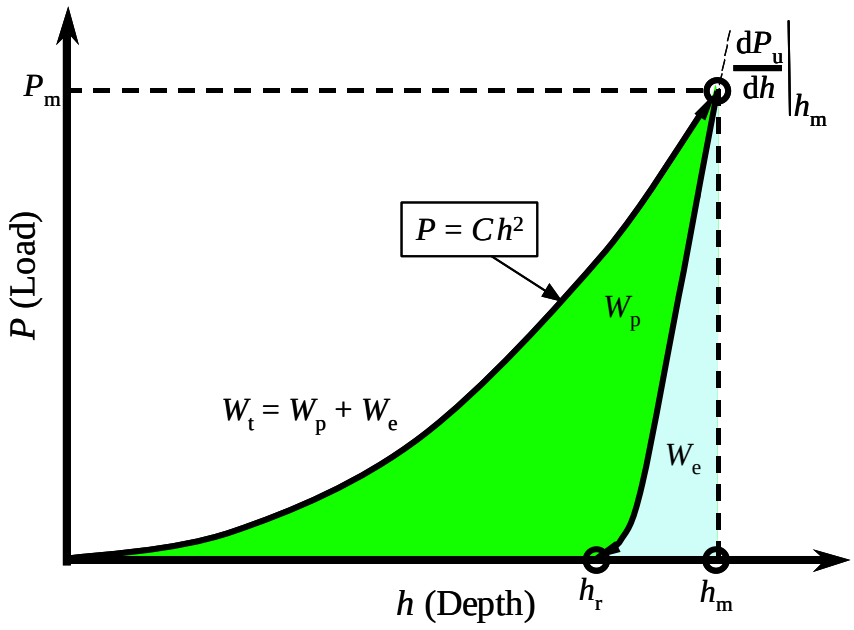

Figure 2-1: Schematic illustration of a typical $P-h$ response of an elasto-plastic material to instrumented sharp indentation.

As discussed by Giannakopoulos and Suresh [41], C, $\frac{\mathrm{d}P_\mathrm{u}}{\mathrm{d}h}\big|_{h_\mathrm{m}}$ and $\frac{h_\mathrm{r}}{h_\mathrm{m}}$ are three independent quantities that can be directly obtained from a single $P-h$ curve. The question remains whether these parameters are sufficient to uniquely determine the indented material's elasto-plastic properties.

Plastic behavior of many pure and alloyed engineering metals can be closely approximated by a power law description, as shown schematically in Fig. 2-2. A simple elasto-plastic, true stress-true strain behavior is assumed to be

$$\sigma = \begin{cases} E\varepsilon & \text{for } \sigma \leqslant \sigma_\mathrm{y} \\ R\varepsilon^n & \text{for } \sigma \geqslant \sigma_\mathrm{y} \end{cases} \tag{2.2}$$

where E is the Young's modulus, R a strength coefficient, n the strain hardening exponent, σ_y the initial yield stress and ε_y the corresponding yield strain, such that

$$\sigma_\mathrm{y} = E\varepsilon_\mathrm{y} = R\varepsilon_\mathrm{y}^n \tag{2.3}$$

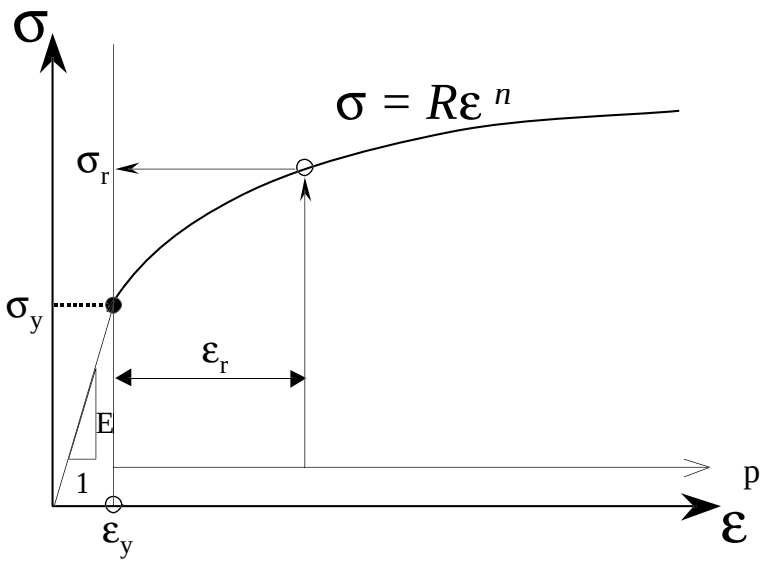

Figure 2-2: The power law elasto-plastic stress-strain behavior used in the current study.

Here the yield stress σ_{y} is defined at zero offset strain. The total effective strain, ε, consists of two parts, ε_{y} and ε_{p}:

$$\varepsilon = \varepsilon_{\mathrm{y}} + \varepsilon_{\mathrm{p}} \tag{2.4}$$

where ε_{p} is the nonlinear part of the total effective strain accumulated beyond ε_{y}. With Eqs. (2.3) and (2.4), when $\sigma > \sigma_{\mathrm{y}}$, Eq. (2.2) becomes

$$\sigma = \sigma_{\mathrm{y}} \left(1 + \frac{E}{\sigma_{\mathrm{y}}} \varepsilon_{\mathrm{p}} \right)^{n} \tag{2.5}$$

To complete the material constitutive description, Poisson's ratio is designated as ν, and the incremental theory of plasticity with von Mises effective stress (J_2 flow theory) is assumed.

With the above assumptions and definitions, a material's elasto-plastic behavior is fully determined by the parameters E, n, σ_{y} and n. Alternatively, with the constitutive law defined in Eq. (2.2), the power law strain hardening assumption reduces the mathematical description of plastic properties to two independent parameters. This pair could

be described as a representative stress σ_r (defined at $\varepsilon_p = \varepsilon_r$, where ε_r is a representative strain) and the strain-hardening exponent n, or as σ_y and σ_r.

2.2.2 Dimensional Analysis and Universal Functions

Cheng and Cheng [33, 34] and Tunvisut *et al.* [47] have used dimensional analysis to propose a number of dimensionless universal functions, with the aid of computational data points calculated via the Finite Element Method (FEM). Here, a number of new dimensionless functions are described in the following paragraphs.

As discussed in Section 2.2.1, one can use a material parameter set (E, ν, σ_y and n), (E, ν, σ_r and n) or (E, n, σ_y and σ_r) to describe the constitutive behavior. Therefore, the specific functional forms of the universal dimensionless functions are not unique (but different definitions are interdependent if power law strain hardening is assumed). For instrumented sharp indentation, a particular material constitutive description (e.g., power-law strain hardening) yields its own distinct set of dimensionless functions. One may choose to use any plastic strain to be the representative strain ε_r, where the corresponding σ_r is used to describe the dimensionless functions. However, the representative strain which best normalizes a particular dimensionless function with respect to strain hardening will be a distinct value.

The following section presents a set of universal dimensionless functions and their closed-form relationship between indentation data and elasto-plastic properties (within the context of the present computational results). This set of functions leads to new algorithms for accurately predicting the $P - h$ response from known elasto-plastic properties (forward algorithms) and new algorithms for systematically extracting the indented material's elasto-plastic properties from a single set of $P - h$ data (reverse algorithms).

For a sharp indenter (conical, Berkovich or Vickers, with fixed indenter shape and tip angle) indenting normally into a power law elasto-plastic solid, the load P can be written as

$$P = P(h, E, \nu, E_i, \nu_i, \sigma_y, n), \tag{2.6}$$

where E_i is Young's modulus of the indenter, and ν_i is its Poisson's ratio. This functionality is often simplified (e.g., [49]) by combining elasticity effects of an elastic indenter and an elasto-plastic solid as

$$P = P(h, E^*, \sigma_\mathrm{y}, n), \tag{2.7}$$

where

$$E^* = \left[\frac{1-\nu^2}{E} + \frac{1-\nu_\mathrm{i}^2}{E_\mathrm{i}}\right]^{-1} \tag{2.8}$$

Alternatively, Eq. (2.7) can be written as

$$P = P(h, E^*, \sigma_\mathrm{r}, n), \tag{2.9}$$

or

$$P = P(h, E^*, \sigma_\mathrm{y}, \sigma_\mathrm{r}), \tag{2.10}$$

Applying the Π theorem in dimensional analysis, Eq. (2.9) becomes

$$P = \sigma_\mathrm{r} h^2 \Pi_1 \left(\frac{E^*}{\sigma_r}, n\right) \tag{2.11}$$

and thus

$$C = \frac{P}{h^2} = \sigma_\mathrm{r} \Pi_1 \left(\frac{E^*}{\sigma_\mathrm{r}}, n\right) \tag{2.12}$$

where Π_1 is a dimensionless function. Similarly, applying the Π theorem to Eq. (2.10), loading curvature C may alternatively be expressed as

$$C = \frac{P}{h^2} = \sigma_\mathrm{y} \Pi_1^\mathrm{A} \left(\frac{E^*}{\sigma_\mathrm{y}}, \frac{\sigma_\mathrm{r}}{\sigma_\mathrm{y}}\right) \tag{2.13}$$

or

$$C = \frac{P}{h^2} = \sigma_{\mathrm{r}} \Pi_1^{\mathrm{B}} \left(\frac{E^*}{\sigma_{\mathrm{r}}}, \frac{\sigma_{\mathrm{y}}}{\sigma_{\mathrm{r}}} \right) \tag{2.14}$$

where Π_1^{A} and Π_1^{B} are dimensionless functions. The dimensionless functions given in Eqs. (2.11) to (2.14) are different from those proposed in [33, 34], where the normalization was taken with respect to E^* instead of σ_{r} or σ_{y}.

During nanoindentation experiments, especially when the indentation depth is about 100 to 1000 nm, size-scale-dependent indentation effects have been postulated (e.g., [30, 50, 51]). These possible size-scale-dependent effects on hardness have been modeled using higher order theories (e.g., [50, 51]). If the indentation is sufficiently deep (typically deeper than 1 μm), then the scale dependent effects become small and may be ignored. In the current study, any scale dependent effects are assumed to be insignificant. It is clear from Eqs. (2.11) to (2.14) that $P = Ch^2$ is the natural outcome of the dimensional analysis for a sharp indenter, and that it is independent of the specific constitutive behavior; loading curvature C is a material constant which is independent of indentation depth. It is also noted that, depending on the choices of (ε_{r}, σ_{r}), there are an infinite number of ways to define the dimensionless function Π_1. However, with the assumption of power-law strain hardening, it can be shown that one definition of Π_1 is easily converted to another definition.

If the unloading force is represented as P_{u}, the unloading slope is given by

$$\frac{\mathrm{d}P_{\mathrm{u}}}{\mathrm{d}h} = \frac{\mathrm{d}P_{\mathrm{u}}}{\mathrm{d}h}(h, h_{\mathrm{m}}, E, \nu, E_{\mathrm{i}}, \nu_{\mathrm{i}}, \sigma_{\mathrm{r}}, n) \tag{2.15}$$

or, assuming that elasticity effects are characterized by E^*, the unloading slope is given by

$$\frac{\mathrm{d}P_{\mathrm{u}}}{\mathrm{d}h} = \frac{\mathrm{d}P_{\mathrm{u}}}{\mathrm{d}h}(h, h_{\mathrm{m}}, E^*, \sigma_{\mathrm{r}}, n) \tag{2.16}$$

Dimensional analysis yields

$$\frac{\mathrm{d}P_\mathrm{u}}{\mathrm{d}h} = E^* h \Pi_2^0(\frac{h_\mathrm{m}}{h}, \frac{\sigma_\mathrm{r}}{E^*}, n) \tag{2.17}$$

Evaluating Eq. (2.17) at $h = h_\mathrm{m}$ gives

$$\left.\frac{\mathrm{d}P_\mathrm{u}}{\mathrm{d}h}\right|_{h_\mathrm{m}} = E^* h_\mathrm{m} \Pi_2^0(1, \frac{\sigma_\mathrm{r}}{E^*}, n) = E^* h_\mathrm{m} \Pi_2(\frac{E^*}{\sigma_\mathrm{r}}, n) \tag{2.18}$$

Similarly, P_u itself can be expressed as

$$P_\mathrm{u} = P_\mathrm{u}(h, h_\mathrm{m}, E^*, \sigma_\mathrm{r}, n) = E^* h^2 \Pi_\mathrm{u}(\frac{h_\mathrm{m}}{h}, \frac{\sigma_\mathrm{r}}{E^*}, n) \tag{2.19}$$

When $P_\mathrm{u} = 0$, the specimen is fully unloaded and, thus, $h = h_\mathrm{r}$. Therefore, upon complete unloading,

$$0 = \Pi_\mathrm{u}(\frac{h_\mathrm{m}}{h_\mathrm{r}}, \frac{\sigma_\mathrm{r}}{E^*}, n) \tag{2.20}$$

Rearranging Eq. (2.20),

$$\frac{h_\mathrm{r}}{h_\mathrm{m}} = \Pi_3(\frac{\sigma_\mathrm{r}}{E^*}, n) \tag{2.21}$$

Thus, the three universal dimensionless functions, Π_1, Π_2 and Π_3, can be used to relate the indentation response to mechanical properties.

2.2.3 Computational Model

Axisymmetric two-dimensional and full three-dimensional finite element models were constructed to simulate the indentation response of elasto-plastic solids. Figure 2-3(a) schematically shows the conical indenter, where θ is the included half angle of the indenter, h_m is the maximum indentation depth, and a_m is the contact radius measured at h_m. The true projected contact area A_m, with pile-up or sink-in effects taken into account, for a conical indenter is thus

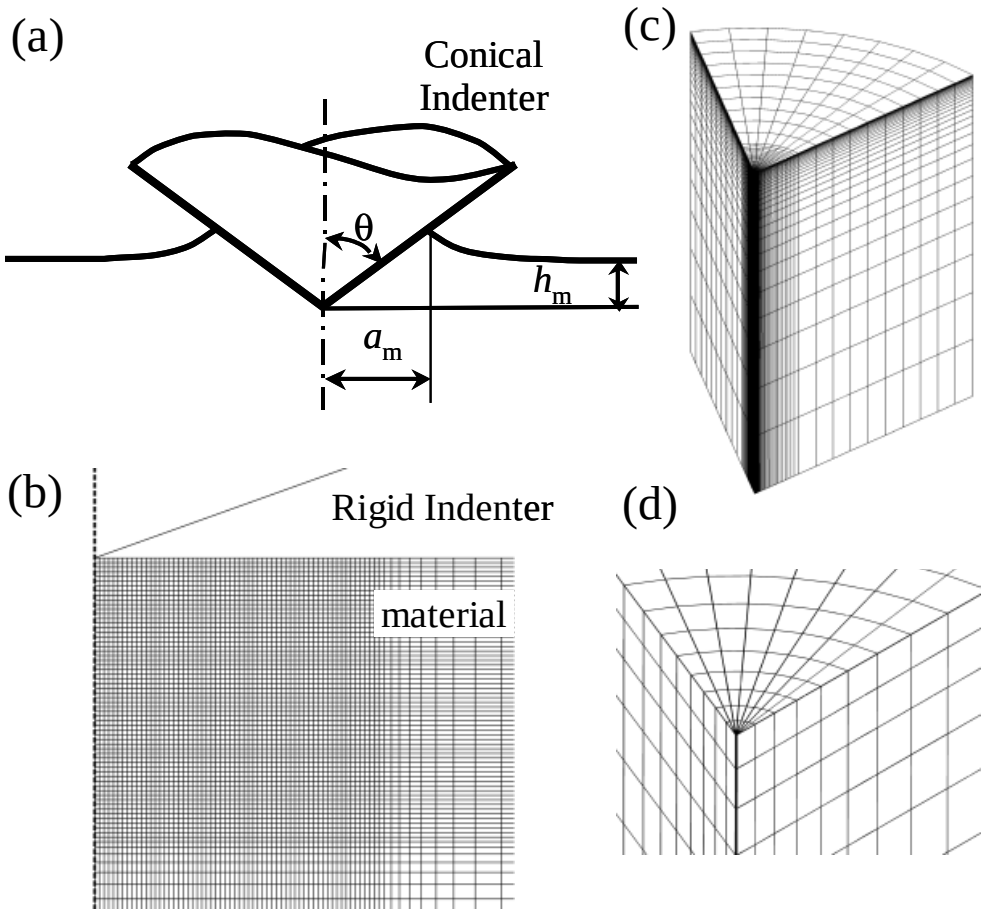

Figure 2-3: Computational modeling of instrumented sharp indentation. (a) Schematic drawing of the conical indenter, (b) mesh design for axisymmetric finite element calculations, (c) overall mesh design for the Berkovich indentation calculations, and (d) detailed illustration of the area that directly contacts the indenter tip in (c).

$$A_{\mathrm{m}} = \pi a_{\mathrm{m}}^2 \tag{2.22}$$

Figure 2-3(b) shows the mesh design for axisymmetric calculations. The semi-infinite substrate of the indented solid was modeled using 8100 four-noded, bilinear axisymmetric quadrilateral elements, where a fine mesh near the contact region and a gradually coarser mesh further from the contact region were designed to ensure numerical accuracy. At the maximum load, the minimum number of contact elements in the contact zone was no less than 16 in each FEM computation. The mesh was well-tested for convergence and was determined to be insensitive to far-field boundary conditions.

Three-dimensional finite element models incorporating the inherent six-fold or eight-fold symmetry of a Berkovich or a Vickers indenter, respectively, were also constructed. A total of 11,150 and 10,401 eight-noded, isoparametric elements was used for Berkovich and Vickers indentation, respectively. Figure 2-3(c) shows the overall mesh design for the Berkovich indentation, while Fig. 2-3(d) details the area that directly contacts the indenter tip. Computations were performed using the general purpose finite element package ABAQUS [52]. The three-dimensional mesh design was verified against the three-dimensional results obtained from the mesh used previously by Larsson *et al.* [4]. Unless specified otherwise, large deformation theory was assumed throughout the analysis.

For a conical indenter, the projected contact area is $A = \pi h^2 \tan^2 \theta$; for a Berkovich indenter, $A = 24.56h^2$; for a Vickers indenter, $A = 24.50h^2$. In this study, the three-dimensional indentation induced via Berkovich or Vickers geometries was approximated with axisymmetric two-dimensional models by choosing the apex angle θ such that the projected area/depth of the two-dimensional cone was the same as that for the Berkovich or Vickers indenter. For both Berkovich and Vickers indenters, the corresponding apex angle θ of the equivalent cone was chosen as 70.3^{o}. Axisymmetric two-dimensional computational results will be referenced in the remainder of the paper unless otherwise specified. In all finite element computations, the indenter was modeled as a rigid body, and the contact was modeled as frictionless. Detailed pile-up and sink-in effects were more accurately accounted for by the large deformation FEM computations, as compared to small deformation computations.

2.2.4 Comparison of Experimental and Computational Results

Two aluminum alloys were obtained for experimental investigation: 6061-T651 and 7075-T651 aluminum, both in the form of 2.54 cm diameter, extruded round bar stock. Two compression specimens (0.5 cm diameter, 0.75 cm height) were machined from each bar such that the compression axis was parallel to the extrusion direction. Simple uniaxial compression tests were conducted on a servo-hydraulic universal testing machine at a crosshead speed of 0.2 mm/min. Crosshead displacement was obtained from a calibrated LVDT (linear voltage-displacement transducer). As each specimen was compressed to 45% engineering strain, the specimen ends were lubricated with Teflon$^{\text{TM}}$ lubricant to prevent barreling. Intermittent unloading was conducted to allow for repeated measurement of Young's modulus and relubrication of the specimen ends. Recorded load-displacement data were converted to true stress-true strain data. Although the true stress-true strain responses were well approximated by power law fits, these experimental stress-strain data which were used as direct input for FEM simulations, rather than the mathematical approximations (see Fig. 2-4). For 7075-T651 aluminum, the measured Young's modulus was $E = 70.1$ GPa ($\nu = 0.33$); and for 6061-T651 aluminum, $E = 66.8$ GPa ($\nu = 0.33$).

Indentation specimens were machined from the same round bar stock as discs of the bar diameter (3 mm thickness). Each specimen was polished to 0.06 mm surface finish with colloidal silica. These specimens were then indented on a commercial nanoindenter (Micro-Materials, Wrexham, UK) with a Berkovich diamond indenter at a loading/unloading rate of approximately 0.2 N/min. For each of three maximum loads (3, 10, and 20 N), five tests were conducted on two consecutive days, for a total of ten tests per load in each specimen. Figure 2-5 shows the typical indentation responses of both the 7075-T651 aluminum and 6061-T651 aluminum specimens, respectively. The corresponding finite element computations using conical, Berkovich and Vickers indenters are also plotted in Fig. 2-5. Figure 2-6 shows the equivalent plastic strain (PEEQ) within the 7075-T651 aluminum near the tip of the conical indenter, indicating that the majority of the volume directly beneath the indenter experienced strains exceeding 15%. Assuming only the $\sigma - \varepsilon$ constitutive response obtained from experimental uniaxial compression, the computational $P - h$ curves agree well with the experimental curves, as shown in Fig. 2-5. The computational $P - h$ responses

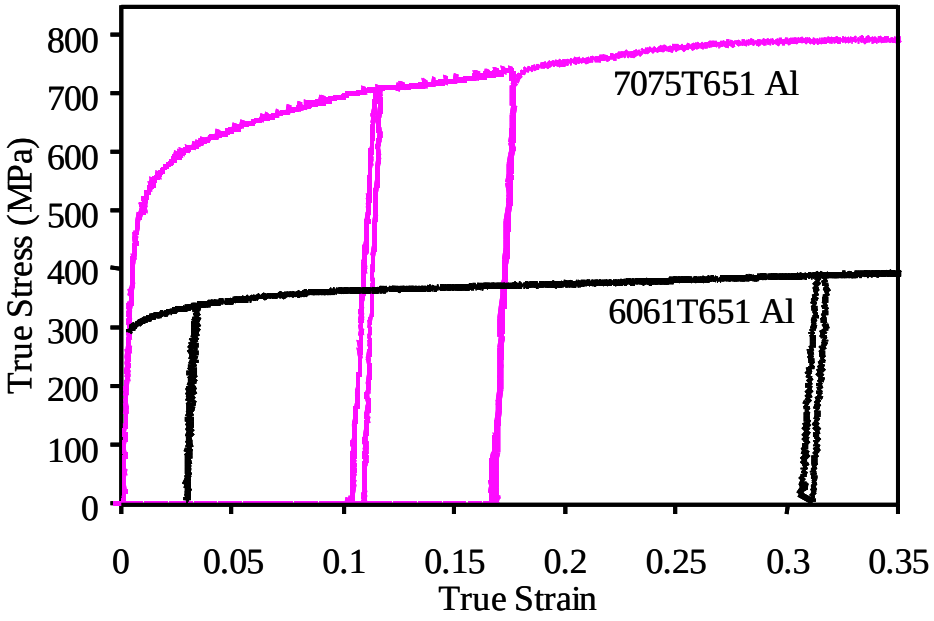

Figure 2-4: Experimental uniaxial compression stress-strain curves of both 6061-T651 aluminum and 7075-T651 aluminum specimens, respectively.

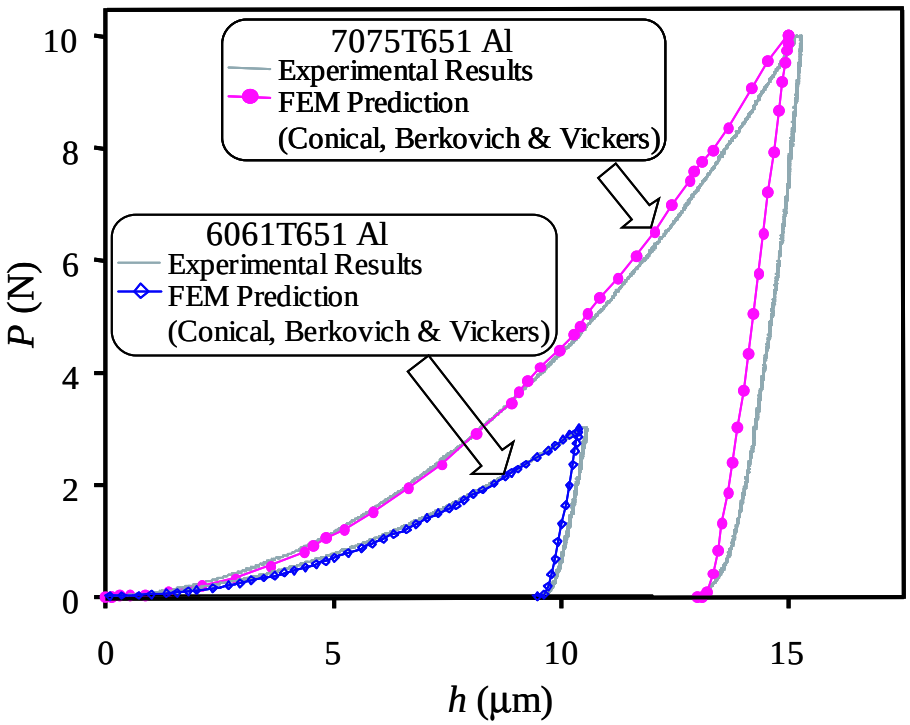

Figure 2-5: Experimental versus computational indentation responses of both the 7075-T651 aluminum and 6061-T651 aluminum specimens, respectively.

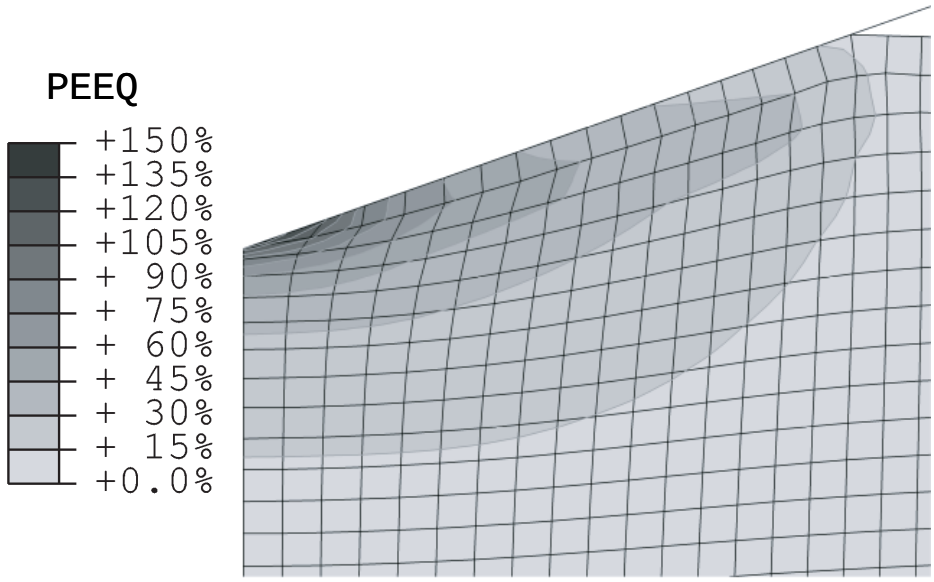

Figure 2-6: Contour plot of the equivalent plastic strain (PEEQ) within the 7075-T651 aluminum near the tip of the conical indenter, indicating that the majority of the volume directly beneath the indenter experienced strains exceeding 15%.

of the conical, Berkovich and Vickers indentations were found to be virtually identical.

2.2.5 Large Deformation vs. Small Deformation

Giannakopoulos *et al.* [3], Larsson *et al.* [4], Giannakopoulos and Suresh [41], and Venkatesh *et al.* [42] have proposed a systematic methodology to extract elasto-plastic properties from a single $P-h$ curve. The loading curvature C was given as

$$C = M_1 \sigma_{0.29} \left[1 + \frac{\sigma_y}{\sigma_{0.29}}\right] \left[M_2 + \ln\left(\frac{E^*}{\sigma_y}\right)\right] \tag{2.23}$$

where M_1 and M_2 are computationally derived constants which depend on indenter geometry. The representative stress $\sigma_{0.29}$ is defined as a true stress at true plastic strain of 29%. It is interesting to note that, after rewriting $\sigma_{0.29}\left(1+\frac{\sigma_y}{\sigma_{0.29}}\right)$ as $\sigma_y\left(1+\frac{\sigma_{0.29}}{\sigma_y}\right)$, Eq. (2.23) is consistent with Eq. (2.13).

Figure 2-7 shows the comparison between the large deformation solution, small deformation solution and the predictions from Eq. (2.23), using the four model materials

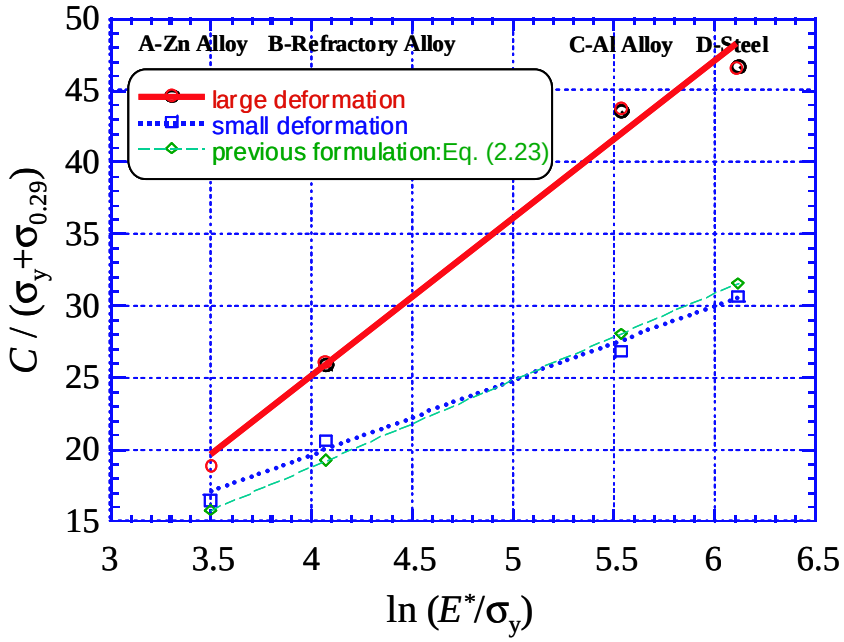

Figure 2-7: Comparison between the large deformation solution, small deformation solution and the previous formulation (Eq. (2.23)) using four model materials. For all four cases studied, large deformation theory always predicts a stiffer loading response.

listed in Venkatesh *et al.* [42] (see Table 2.1). From Fig. 2-7, it is evident that Eq. (2.23) agrees well with the small deformation results and that, for all four cases studied, large deformation theory always predicts a stiffer loading response.

In addition, 76 different cases covering material parameters of most engineering metals were studied computationally. Detailed examination showed that large deformation solutions are not readily described by Eq. (2.23), but rather are better approximated within $\pm 10\%$ (for the conical indenter with $\theta = 70.3^o$) by a new universal function given by

$$C = N_1 \sigma_{0.29} \left[1 + \frac{\sigma_y}{\sigma_{0.29}}\right] \left[N_2 + \ln\left(\frac{E^*}{\sigma_{0.29}}\right)\right] \tag{2.24}$$

where $N_1 = 9.4509$ and $N_2 = -1.2433$ are computationally derived constants specific to the indenter geometry. This expression is consistent with the dimensionless function shown in Eq. (2.14).

Table 2.1: Four cases studied to compare large vs small deformation theory.

Case	System	E (GPa)	Yield Strength (MPa)	n	ν
A	Zinc alloy	9	300	0.05	0.3
B	Refractory alloy	80	1500	0.05	0.3
C	Aluminum alloy	70	300	0.05	0.28
D	Steel	210	500	0.1	0.27

2.3 Computational Results

A comprehensive parametric study of 76 additional cases was conducted (see Table 2.2 for a complete list of parameters). These cases represented the range of parameters of mechanical behavior found in common engineering metals: that is, Young's modulus E ranged from 10 to 210 GPa, yield strength σ_{y} from 30 to 3000 MPa, strain hardening exponent n from 0 to 0.5, and Poisson's ratio ν was fixed at 0.3. The axisymmetric finite element model was used to obtain computational results unless otherwise specified.

2.3.1 Representative Strain and Universal Dimensionless Functions

The first dimensionless function of interest is Π_1 in Eq. (2.12). From Eq. (2.12),

$$\Pi_1\left(\frac{E^*}{\sigma_{\mathrm{r}}}, n\right) = \frac{C}{\sigma_{\mathrm{r}}} \tag{2.25}$$

The specific functional form of Π_1 depends on the choice of ε_{r} and σ_{r}. Figure 2-8 shows the computationally obtained results using three different values of ε_{r} (i.e., $\varepsilon_{\mathrm{p}} = 0.01$, 0.033 and 0.29) and the corresponding σ_{r}. The results in Fig. 2-8 indicate that for $\varepsilon_{\mathrm{r}} < 0.033$, Π_1 increased with increasing n; for $\varepsilon_{\mathrm{r}} > 0.033$, Π_1 decreased with increasing n. Minimizing the relative errors using a least squares algorithm, it is confirmed that when $\varepsilon_{\mathrm{r}} = 0.033$, a polynomial function $\Pi_1\left(\frac{E^*}{\sigma_{0.033}}, n\right) = \frac{C}{\sigma_{0.033}}$[‡] fits all 76 data points within a $\pm 2.85\%$ error (see

[‡]See Appendix A.1 for a complete listing of functions.

Table 2.2: Elasto-plastic parameters used in the present study (ν is fixed at 0.3) For each of the 19 cases below, strain-hardening exponent n is varied from 0, 0.1, 0.3 to 0.5, resulting a total of 76 different cases

Case	E [GPa]	σ_y [MPa]	σ_y/E
19 combinations of E and σ_{y}	10	30	0.003
	10	100	0.01
	10	300	0.03
	50	200	0.004
	50	600	0.012
	50	1000	0.02
	50	2000	0.04
	90	500	0.005556
	90	1500	0.01667
	90	3000	0.03333
	130	1000	0.007692
	130	2000	0.015385
	130	3000	0.023077
	170	300	0.001765
	170	1500	0.008824
	170	3000	0.017647
	210	300	0.001429
	210	1800	0.008571
	210	3000	0.014286

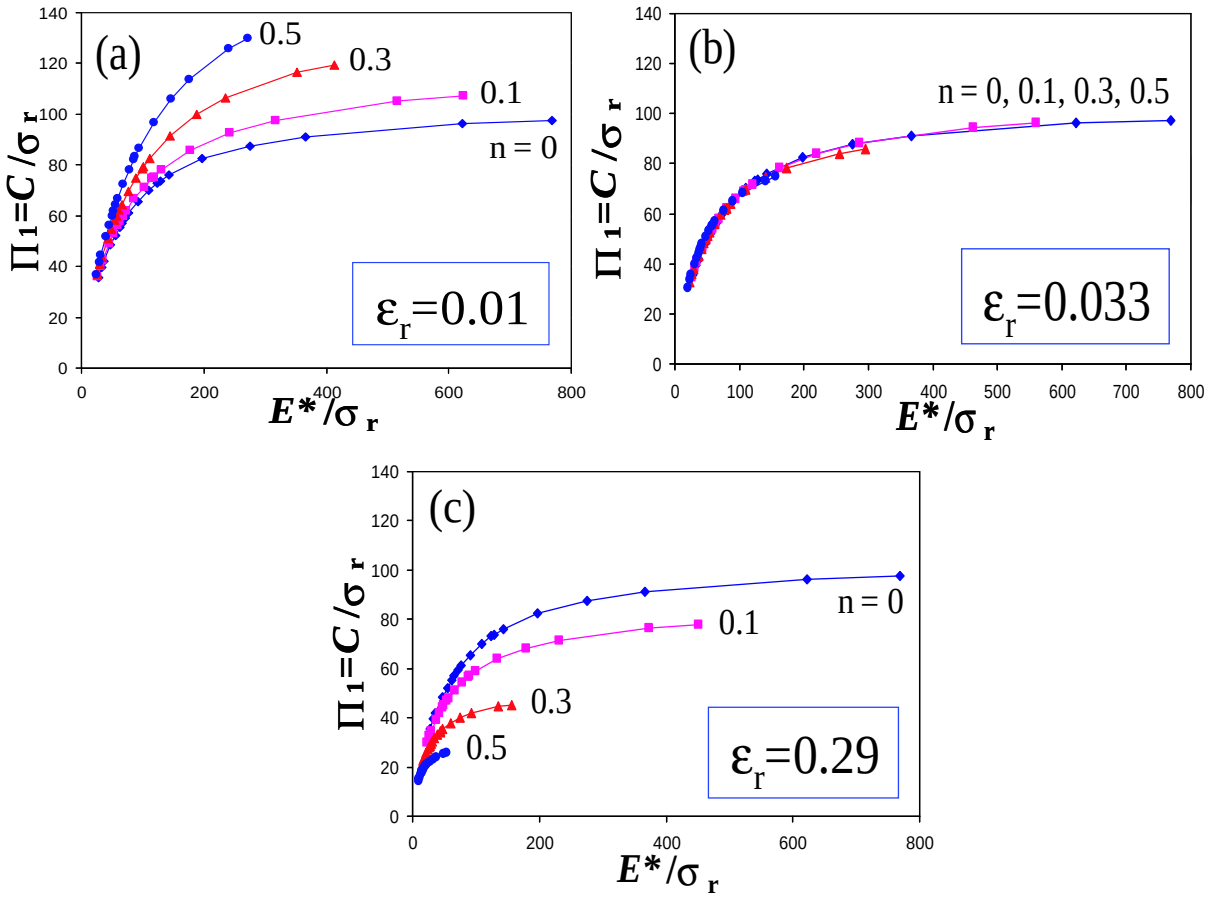

Figure 2-8: Dimensionless function Π_1 constructed using three different values of ε_r (i.e., ε_p = 0.01, 0.033 and 0.29) and the corresponding σ_r, respectively. For $\varepsilon_r < 0.033$, Π_1 increased with increasing n; for $\varepsilon_r > 0.033$, Π_1 decreased with increasing n. A representative plastic strain $\varepsilon_r = 0.033$ can be identified as a strain level which allows for the construction of Π_1 to be independent of strain hardening exponent n.

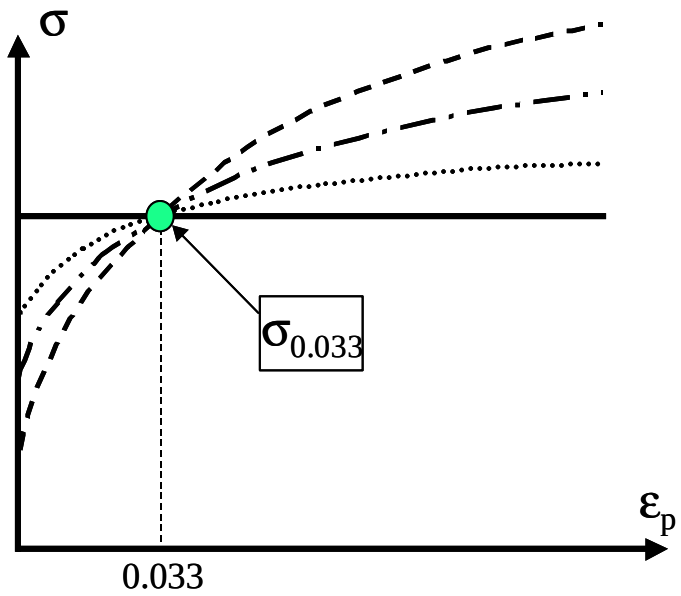

Figure 2-9: For a given value of E^*, all power law plastic, true stress-true strain responses that exhibit the same true stress at 3.3% true plastic strain give the same indentation loading curvature C. A collection of such plastic stress-strain curves are schematically illustrated in the figure.

Fig. 2-8(b)). A representative strain of $\varepsilon_{\rm r} = 0.033$ was thus identified. The corresponding dimensionless function Π_1 normalized with respect to $\sigma_{0.033}$ was found to be independent of the strain hardening exponent n. This result indicates that, for a given value of E^*, all power law plastic, true stress-true strain responses that exhibit the same true stress at 3.3% true plastic strain give the same indentation loading curvature C (see Fig. 2-9). It is noted that this result was obtained within the specified range of material parameters using the material constitutive behavior defined by Eq. (2.2).

Figure 2-10 show the dimensionless functions Π_2 and Π_3. Within a $\pm 2.5\%$ and a $\pm 0.77\%$ error, $\Pi_2\left(\frac{E^*}{\sigma_{\rm r}}, n\right) = \frac{1}{E^* h_{\rm m}} \frac{{\rm d}P_{\rm u}}{{\rm d}h}\big|_{h_{\rm m}}{}^{\ddagger}$ and $\Pi_3\left(\frac{\sigma_{\rm r}}{E^*}, n\right) = \frac{h_{\rm r}}{h_{\rm m}}{}^{\ddagger}$ fit all 76 sets of computed data shown in Figs. 2-10(a) and 2-10(b), respectively. Several other (approximate) dimensionless functions were also computationally derived. Figure 2-11(a) shows the dimensionless function $\Pi_4\left(\frac{h_{\rm r}}{h_{\rm m}}\right) = \frac{p_{\rm ave}}{E^*}{}^{\ddagger}$ within $\pm 13.85\%$ of the computationally obtained values for the 76 cases studied. It is noted that the verified range for Π_4 is $0.5 < \frac{h_{\rm r}}{h_{\rm m}} < 0.98$. Figure 2-11(b) shows dimensionless function $\Pi_5\left(\frac{h_{\rm r}}{h_{\rm m}}\right) = \frac{W_{\rm p}}{W_{\rm t}}{}^{\ddagger}$ within $\pm 2.38\%$ of the numerically computed values for the 76 cases. The verified range for function Π_5 is the same as that

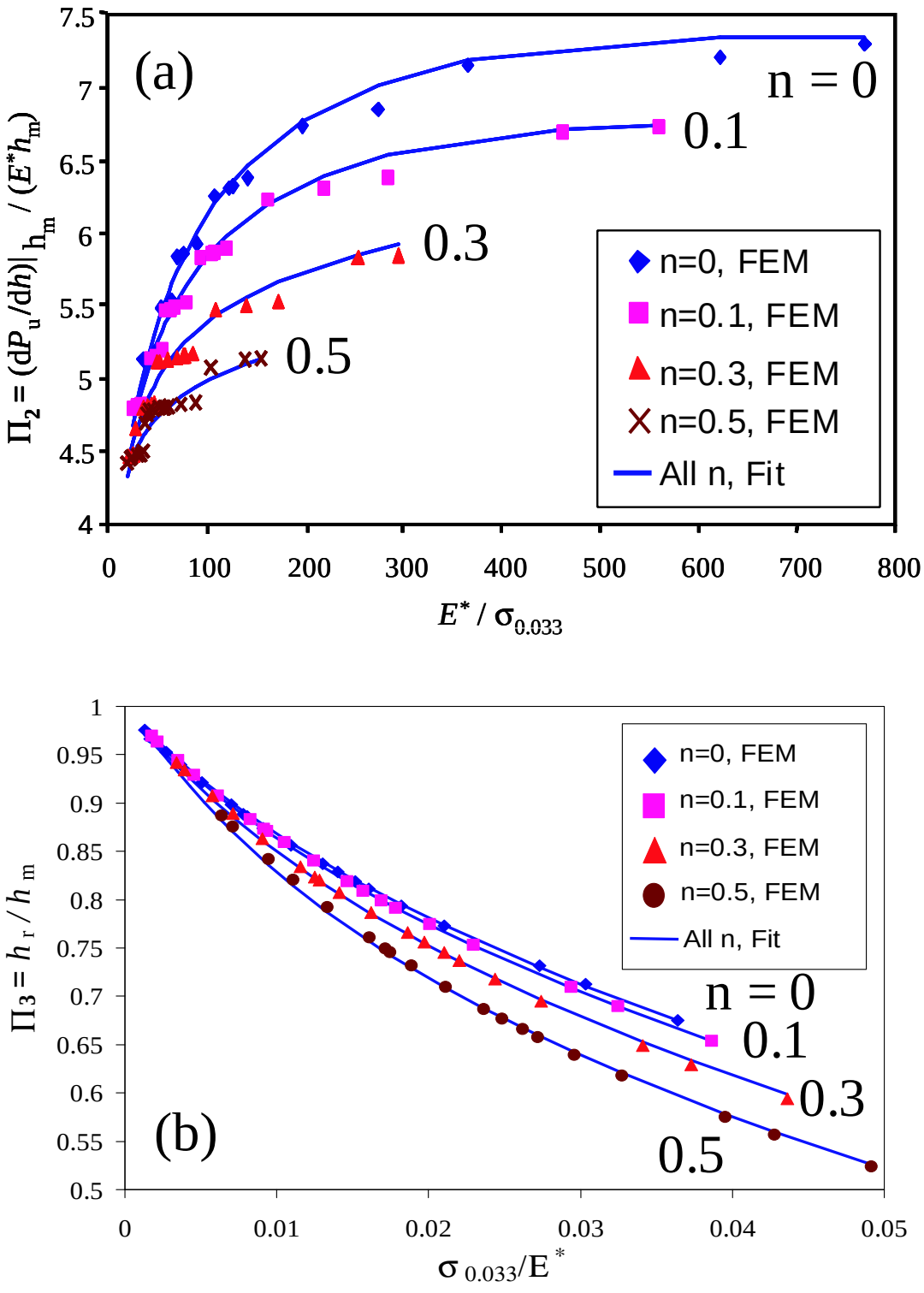

Figure 2-10: Dimensionless functions (a) $\Pi_2\left(\frac{E^*}{\sigma_r}, n\right)$ and (b) $\Pi_3\left(\frac{\sigma_r}{E^*}, n\right)$.

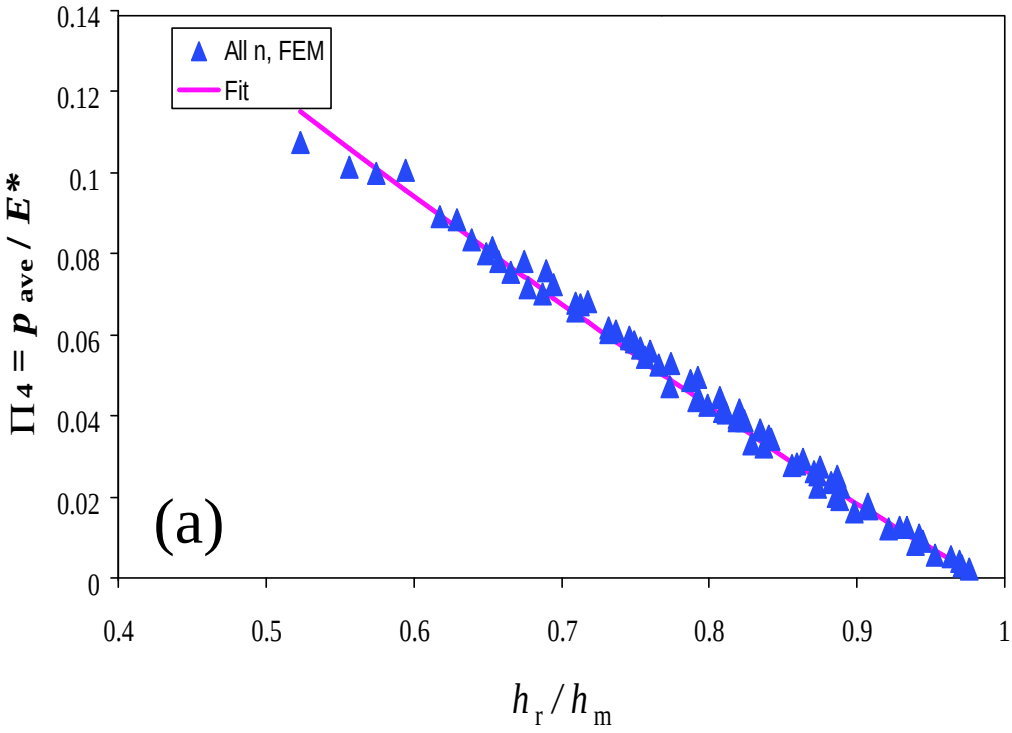

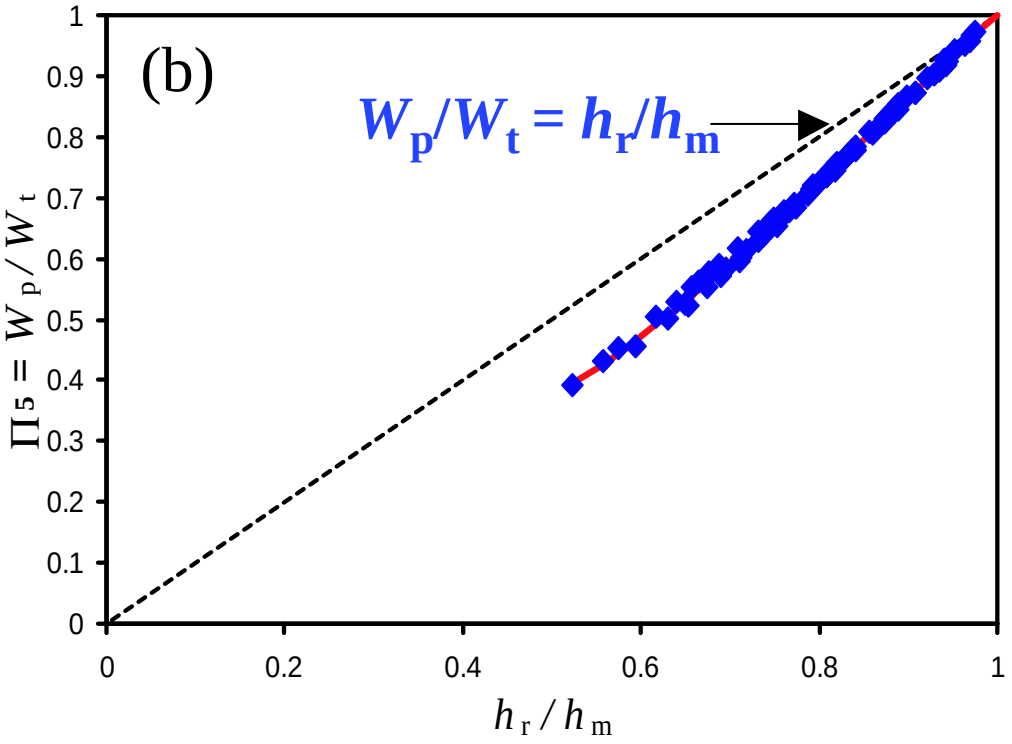

Figure 2-11: Dimensionless functions (a) $\Pi_4\left(\frac{h_r}{h_m}\right)$ and (b) $\Pi_5\left(\frac{h_r}{h_m}\right)$.

for Π_4, i.e. $0.5 < \frac{h_r}{h_m} < 0.98$. From Fig. 2-11(b), it is obvious that $\frac{W_p}{W_t} = \frac{h_r}{h_m}$ is not a good approximation except when $\frac{h_r}{h_m}$ approaches unity.

According to King [53]

$$E^* = \frac{1}{c^*\sqrt{A_m}} \left.\frac{dP}{dh}\right|_{h_m} \tag{2.26}$$

where linear elastic analysis gives $c^* = 1.167$ for the Berkovich indenter, 1.142 for the Vickers indenter and 1.128 for the conical indenter. Large deformation elasto-plastic analysis of the 76 cases showed that $c^* \approx 1.1957$ (within $\pm 0.9\%$ error) for the conical indenter with $\theta = 70.3^o$. This value of c^*, which takes into account the elasto-plastic finite deformation prior to the unloading, is about 6% higher than the small-deformation, linear-elastic solution. It is noted that the initial unloading response is expected to be entirely elastic, and the linear elastic solution is quite accurate compared to the large deformation solution. Assuming the same relative influence of the large deformation elasto-plastic solution on the elastic solution for the Berkovich and Vickers geometries, the adjusted values of c^* were proposed to be 1.2370 and 1.2105, respectively. This completes another important dimensionless function Π_6 ,

$$\Pi_6 = \frac{1}{E^*\sqrt{A_m}} \left.\frac{dP}{dh}\right|_{h_m} = c^* \tag{2.27}$$

For a conical indenter with $\theta = 70.3^o$, noting that $A_m = \pi a_m^2$, Eq. (2.27) can be rewritten as

$$\Pi_{6C} = \frac{1}{E^* a_m} \left.\frac{dP}{dh}\right|_{h_m} = c^*\sqrt{\pi} \approx 2.12 \tag{2.28}$$

Note that Eq. (2.28) is simply a revision of Eq. (2.26) in light of the computationally derived values of c^*. In Oliver and Pharr [27], $c^*\sqrt{\pi} = 2$ (i.e., $c^* = 1.128$, the linear elastic solution) was used. Table 2.3 tabulates the values of c^* used in the current study and in the literature.

It is noted that Π_3 and Π_4 are interdependent, i.e., function Π_4 together with di-

Table 2.3: The values of c^* used in the current study.

c^*	Small deformation linear elastic solution[53]	Large deformation elasto-plastic solution[22]
Conical	1.128	1.1957
Berkovich	1.167	1.2370
Vickers	1.142	1.2105

mensionless functions Π_1, Π_2 and Π_6, can be used to solve for Π_3. Function Π_5 relates $\frac{W_\mathrm{p}}{W_\mathrm{t}}$ to $\frac{h_\mathrm{r}}{h_\mathrm{m}}$. Alternative and/or more concise universal dimensionless functions (i.e., Π_1 to Π_5), which fit the same set of data taken from the 76 cases examined in the present study, may also be explored.

2.3.2 Forward Analysis Algorithms

The forward analysis leads to prediction of the $P - h$ response from known elasto-plastic properties. With the available dimensionless functions Π_1, Π_2, Π_3, Π_4, Π_5 and Π_6, the forward analysis algorithm is readily constructed. One such set of algorithms is shown in Fig. 2-12. Alternatively, $\frac{h_\mathrm{r}}{h_\mathrm{m}}$ can also be obtained using function Π_3 instead of Π_4. As discussed earlier, Π_3 and Π_4 are interdependent functions.

To verify the accuracy of the proposed algorithms, uniaxial compression and indentation experiments were conducted in two materials: 7075-T651 aluminum and 6061-T651 aluminum. Values for E and σ_y were obtained from the resulting experimental true stress-true total strain data. The value for $\sigma_{0.033}$ was then determined from the true stress-true plastic strain data. Finally, a power law equation was fit to the true stress-true plastic strain data (see Fig. 2-4) to estimate a value for n (see Table 2.4). The Poisson ratio ν was not experimentally determined, and was assigned a typical value of 0.33 for aluminum alloys. The parameters E_i and ν_i were assigned values of 1100 GPa and 0.07, respectively; these are typical values for diamond taken from the literature [54]. Microhardness specimens were prepared identically to the microindentation specimens, and were indented on

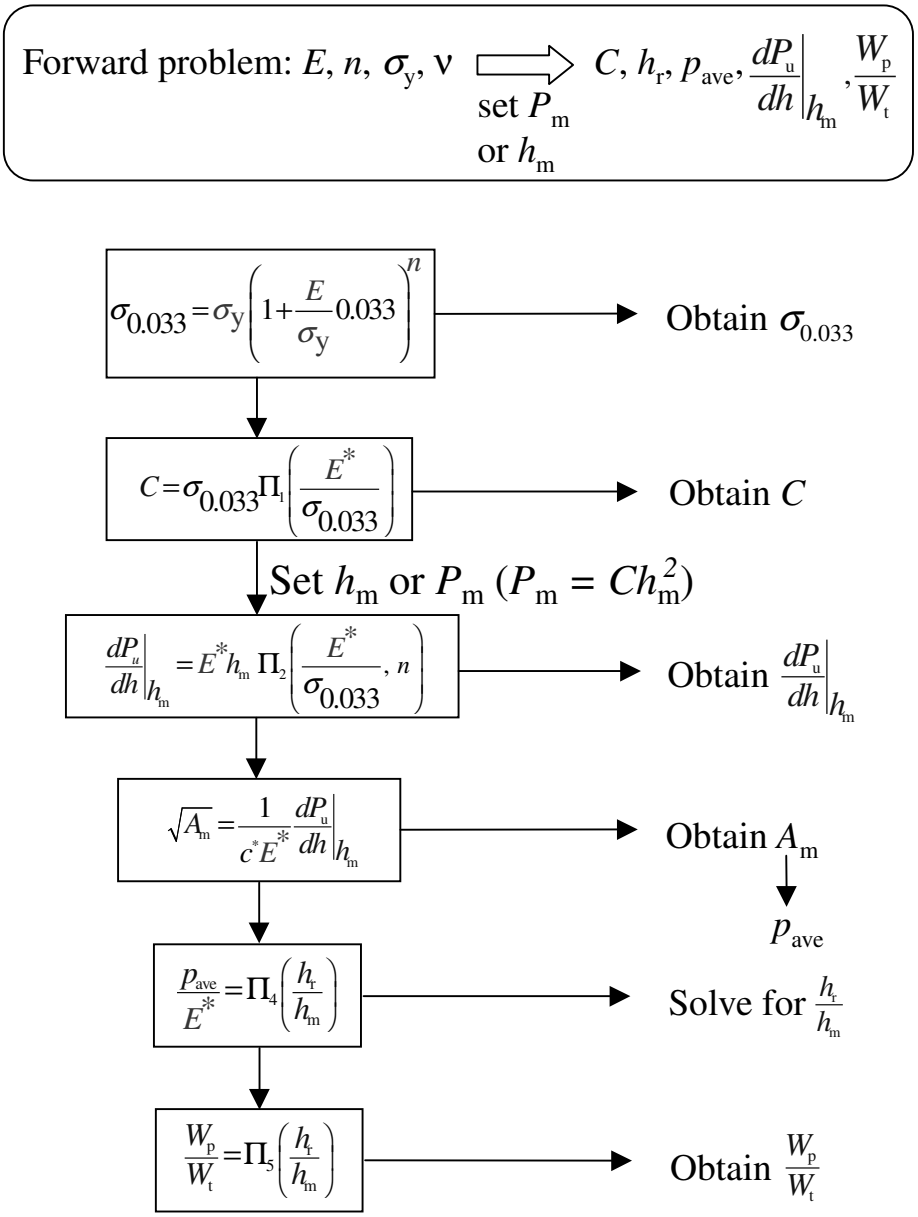

Figure 2-12: Forward Analysis Algorithms

Table 2.4: Mechanical property values used in forward analysis.

Material	E (GPa)	ν	E^* (GPa)[a]	σ_y (MPa)[b]	$\sigma_{0.033}$ (MPa)	n[c]	Vickers hardness $\left[\frac{\text{kgf}}{\text{mm}^2}\right]$[d]	p_{ave} (MPa)[e]
Al6061-T651	66.8	0.33	70.2	284	338	0.08	104.7	1108
Al7075-T651	70.1	0.33	73.4	500	617.5	0.122	174.1	1842

[a] Calculated from Eq. (2.8) using $E_i = 1100$ GPa and $\nu_i = 0.07$ for the diamond indenter.
[b] Estimated at 0% offset strain.
[c] Estimated from power law fit.
[d] Averaged from 10 and 5 hardness tests (P = 0.1 kgf) for Al 6061-T651 and Al 7075-T651 specimens, respectively.
[e] Estimated from the hardness number assuming that changes in impression size during unloading can be ignored.

a commercial microhardness tester to a maximum load of 0.1 kgf over a total test time of 20 s. Vickers hardness was calculated as HV $= 1.8544P/D^2$, where P is load (in kgf) and D is the average length of the indentation diagonals (in mm) as observed under an optical microscope with a 40× objective lens. The algorithm shown in Figure 2-12 was applied to solve for C, $\frac{h_r}{h_m}$, A_m, p_{ave} and $\frac{dP}{dh}\big|_{h_m}$. Table 2.4 lists the mechanical property values used in the forward analysis. Tables 2.5(a) and 2.5(b) list the predictions from the forward analysis, along with the values extracted from the experimental indentation data for 7075-T651 aluminum and 6061-T651 aluminum specimens, respectively. As proposed in [27], the experimental values of $\frac{dP}{dh}\big|_{h_m}$ listed in Table 2.5 were obtained by first fitting a power law function $P = A(h - h_r)^m$ to 67% of the unloading data and then evaluating the derivative at $h = h_m$. From Table 2.5, it is evident that the present forward analysis results are in good agreement with the experimental $P - h$ curves.

2.3.3 Reverse Analysis Algorithms

Table 2.5: Forward analysis results on (a) Al 6061-T651 and (b) Al 7075-T651 (max. load = 3 N).

	C [GPa]	%err C^a	$\frac{\mathrm{d}P}{\mathrm{d}h}\Big\vert_{h_\mathrm{m}}$	%err $\frac{\mathrm{d}P}{\mathrm{d}h}\Big\vert_{h_\mathrm{m}}$	$\frac{W_\mathrm{p}}{W_\mathrm{t}}$	%err $\frac{W_\mathrm{p}}{W_\mathrm{t}}$
(a) Al 6061-T651						
Test 1	27.4	-1.6%	4768	1.6%	0.902	0.8%
Test 2	28.2	1.2%	4800	2.3%	0.905	1.2%
Test 3	27.2	-2.4%	4794	2.2%	0.904	1.1%
Test 4	27.3	-2.2%	4671	-0.4%	0.889	-0.6%
Test 5	27.0	-3.2%	4762	1.5%	0.889	-0.6%
Test 6	27.6	-0.9%	4491	-4.2%	0.891	-0.4%
Ave	27.4		4715		0.896	
$STDEV^b$	0.6		110.9		0.007	
$STDEV/X_\mathrm{prediction}$	2.1%		2.4%		0.8%	
Forward Prediction^c	27.9		4691		0.894	
(b) Al 7075-T651						
Test 1	42.0	-4.2%	3665	2.2%	0.833	1.0%
Test 2	40.9	-6.9%	3658	2.1%	0.838	1.7%
Test 3	42.3	-3.7%	3654	1.9%	0.832	1.0%
Test 4	43.1	-1.7%	3744	4.5%	0.836	1.5%
Test 5	43.5	-0.7%	3789	5.7%	0.839	1.8%
Test 6	44.6	1.6%	3706	3.4%	0.831	0.9%
Ave	42.7		3703		0.835	
$STDEV^b$	1.6		128.1		0.011	
$STDEV/X_\mathrm{prediction}$	3.7%		3.6%		1.3%	
Forward Prediction^c	43.9		3585		0.824	

[a] All errors were computed as $\frac{X_\mathrm{test}-X_\mathrm{prediction}}{X_\mathrm{prediction}}$, where X represents a variable.

[b] $STDEV = \sqrt{\frac{1}{N}\sum_{i=1}^{N}(X_\mathrm{test} - X_\mathrm{prediction})^2}$, where X represents a variable.

[c] Assume $\nu = 0.33$ and Berkovich c^*.

Figure 2-13: Reverse Analysis Algorithms

Table 2.6: Reverse analysis on (a) Al 6061-T651 and (b) Al 7075-T651 (max. load = 3 N; assume $\nu = 0.3$).

	Oliver and Pharr [27]		Doerner and Nix [25]		Current method using Berkovich c^*								
	E^* (GPa)	%err E^* [a]	E^* (GPa)	%err E^*	E^* (GPa)	%err E^*	$\sigma_{0.033}$ (MPa)	%err $\sigma_{0.033}$	n	σ_y (MPa)	%err σ_y	p_{ave} (MPa)	%err p_{ave}
(a) Al 6061-T651													
Test 1	85.8	22.2%	85.3	21.5%	67.6	-3.7%	334.5	-1.0%	0.002	333.1	17.3%	904	-18.4%
Test 2	87.7	25.0%	87.3	24.4%	66.1	-5.8%	349.4	3.4%	0	349.4	23.0%	849	-23.4%
Test 3	86.0	22.5%	85.6	22.0%	66.5	-5.3%	332.8	-1.5%	0	332.8	17.2%	860	-22.4%
Test 4	84.1	19.7%	83.9	19.5%	75.0	6.8%	322.9	-4.5%	0.234	171.0	-39.8%	1150	3.8%
Test 5	85.0	21.1%	85.0	21.0%	77.8	10.8%	315.9	-6.5%	0.298	128.0	-54.9%	1198	8.1%
Test 6	81.4	16.0%	80.9	15.3%	67.9	-3.4%	337.4	-0.2%	0.088	278.5	-1.9%	1025	-7.5%
Ave	85.0		84.7		70.1		332.1		0.104	265.5		998	
$STDEV$ [b]	14.9		14.6		4.5		12.2			87.7		176.5	
$\frac{STDEV}{X_{exp}}$	21.3%		20.8%		6.5%		3.6%			30.9%		15.9%	
(b) Al 7075-T651													
Test 1	84.3	14.8%	83.3	13.5%	73.7	0.5%	579.3	-6.2%	0.130	457.1	-8.6%	1799	-2.3%
Test 2	83.4	13.6%	82.8	12.8%	71.5	-2.6%	564.2	-8.6%	0.085	486.2	-2.8%	1656	-10.1%
Test 3	84.5	15.2%	84.0	14.5%	74.0	0.8%	583.2	-5.6%	0.132	458.2	-8.4%	1807	-1.9%
Test 4	87.5	19.2%	87.2	18.8%	75.4	2.8%	595.6	-3.6%	0.098	500.7	0.1%	1780	-3.4%
Test 5	89.4	21.9%	88.4	20.4%	76.6	4.4%	599.6	-2.9%	0.088	513.4	2.7%	1756	-4.7%
Test 6	88.2	20.2%	87.4	19.0%	76.5	4.2%	620.4	0.5%	0.108	513.4	2.7%	1870	1.5%
Ave	86.2		85.5		74.6		590.4		0.107	488.2		1778	
$STDEV$ [b]	13.0		12.3		2.2		32.4			26.2		91	
$\frac{STDEV}{X_{exp}}$	17.7%		16.8%		3.0%		5.2%			5.3%		4.9%	

[a] All errors were computed as $\frac{X_{\text{revese analysis}} - \overline{X}_{\text{exp}}}{\overline{X}_{\text{exp}}}$, where X represents a variable.

[b] $STDEV = \sqrt{\frac{1}{N}\sum_{i=1}^{N}(X_{\text{reverse analysis}} - \overline{X}_{\text{exp}})^2}$, where X represents a variable.

The reverse analysis implies estimation of the elasto-plastic properties from one complete (i.e., loading and full unloading) $P-h$ curve. In a similar manner, the dimensionless functions Π_1, Π_2, Π_3, Π_4, Π_5 and Π_6 allow us to construct the reverse algorithms. A set of the reverse analysis algorithms is shown in Figure 2-13. Alternatively, due to the interdependence between Π_3 and Π_4, the dimensionless function Π_3 can be used instead of Π_4 to solve the reverse problem, although this alternative set of algorithms involving Π_3 is not as straightforward as that proposed in Figure 2-13. For those experiments for which it is difficult to measure h_{r} accurately, as proposed by Giannakopoulos and Suresh [41], one can measure $\frac{W_{\mathrm{p}}}{W_{\mathrm{t}}}$ instead and use the dimensionless function Π_5 to obtain $\frac{h_{\mathrm{r}}}{h_{\mathrm{m}}}$.

To verify the reverse analysis algorithms, twelve experimental $P-h$ curves (six from 6061-T651 aluminum specimens and six from 7075-T651 aluminum specimens) shown in Table 2.5 were analyzed to extract elasto-plastic properties of the indented specimens; results are shown in Table 2.6. From Table 2.6, it is clear that the proposed reverse algorithms yield accurate estimates of E and $\sigma_{0.033}$, and give reasonable estimates of σ_{y} (especially after taking an average from the six indentation results) which agree well with experimental compression data. It is noted that changing the definition of σ_{y} to 0.1% or 0.2% (instead of 0%) offset strain would not affect the conclusions. The average pressure p_{ave} also compares well with values estimated from experimental microhardness tests. The fractional errors observed in obtaining n are somewhat misleading, due to the fact that $n \ll 1$. Although the errors obtained from individual $P-h$ curves were relatively large in a few cases, the values averaged from a number of indentation tests appeared to be more reliable. Results in Table 2.6 also show that the proposed reverse algorithms give better predictions than Oliver and Pharr [27] and Doerner and Nix [25] methods for extracting E^* values. This improved calculation of elastic properties is likely due to the fact that sink-in/pile-up effects were taken into account with present model, while they have been neglected before.

2.3.4 Pile-up/Sink-in and Contacted Area

Additional dimensionless functions not used in either forward or reverse algorithms are Π_7 and Π_8 illustrated in Figs. 2-14 and 2-15, respectively. In Fig. 2-14, the contact height (h_{c}) is defined as the height of the indentation contact at the maximum depth, as schematically

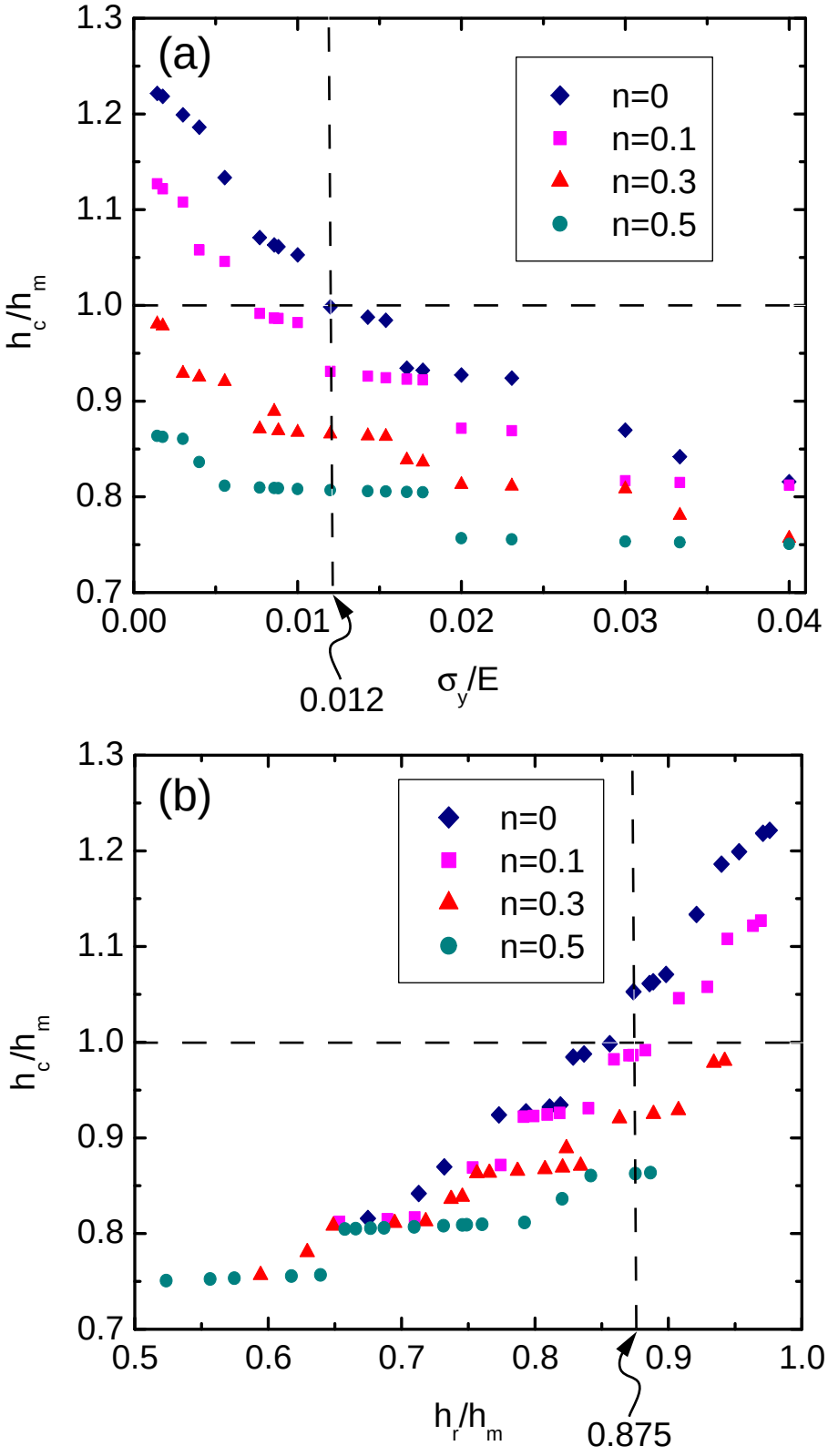

Figure 2-14: Dimensionless functions (a) $\Pi_7\left(\frac{\sigma_y}{E}, n\right)$ and (b) $\Pi_7^0\left(\frac{h_r}{h_m}, n\right)$.

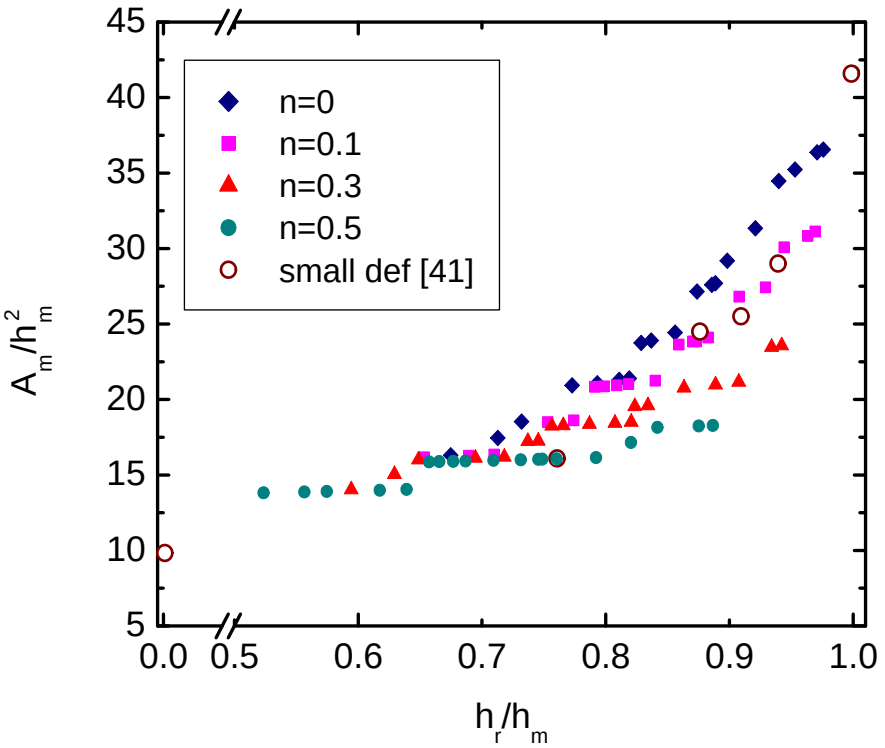

Figure 2-15: Dimensionless function $\Pi_8\left(\frac{h_r}{h_m}, n\right)$.

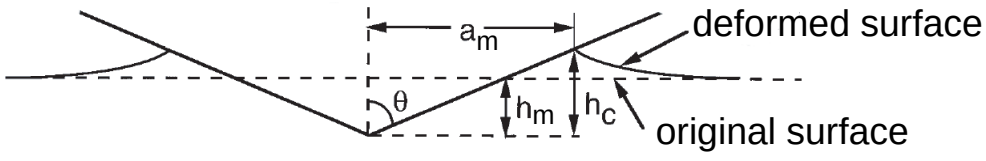

Figure 2-16: Schematic illustration of indentation at maximum load showing contact height h_c for a pile-up case.

shown in Fig. 2-16. It is obvious that the material experiences sink-in when $\frac{h_c}{h_m} < 1$, pile-up when $\frac{h_c}{h_m} > 1$ and neither when $\frac{h_c}{h_m} = 1$. The horizontal dash line in Figs. 2-14(a) and 2-14(b) indicates $\frac{h_c}{h_m} = 1$. Therefore, all the points above this dash line are pile-up cases; whereas, those below the dash line are sink-in cases. Fig. 2-14(a) clearly shows that for materials with large value of $\frac{\sigma_y}{E}$ ($\geqslant 0.012$), sink-in is observed for all values of n. On the other hand, for materials with small value of $\frac{\sigma_y}{E}$ ($\leqslant 0.012$), both pile-up and sink-in can be observed depending on the degree of work hardening n. In the case of highly work-hardened materials ($n \geqslant 0.3$), sink-in is expected even for the materials with small value of $\frac{\sigma_y}{E}$. Similar conclusion is found for the computational works of [33, 55] with the apex angle of 68^o and the experimental works of [24, 56, 57]. The general conclusion is that the pile-up/sink-in behavior depends on both strain hardening exponent (n) and the ratio $\frac{\sigma_y}{E}$.

Fig. 2-14(b) also implies that the pile-up/sink-in behavior does not only depend on the residual depth ratio $\frac{h_r}{h_m}$ but also strain hardening exponent (n). The critical value of $\frac{h_r}{h_m}$ = 0.875 (as suggested by [41] using small deformation theory) is applicable only for small $n \leqslant 0.3$. Fig. 2-14(b) is consistent with Fig. 2-14(a) because the lower $\frac{h_r}{h_m}$, the more elastic the material implying the higher $\frac{\sigma_y}{E}$.

From Fig. 2-16, the contact radius (a_m) is related to the contact depth (h_c) via

$$a_m = h_c \tan(\theta) \tag{2.29}$$

As mentioned earlier, for a conical indenter $A_m = \pi a_m^2$ can be used to convert Fig. 2-14(b) to Fig. 2-15. Likewise, the dimensionless contact area ($\frac{A_m}{h_m^2}$) does not only depend on the residual depth ratio $\frac{h_r}{h_m}$ but also strain hardening exponent (n). Superimposed on Fig. 2-15 are six points calculated from small deformation theory FEM [41], indicating that small deformation theory FEM may not accurately capture the indentation contact area.

2.4 Discussion of Uniqueness, Sensitivity and Representative Strains

2.4.1 Uniqueness in Forward and Reverse Analyses

In order to verify the proposed forward algorithms shown in Fig. 2-12, computational results from the 76 sets of elasto-plastic parameters were taken as input to predict the $P-h$ responses. Each of the forward analyses resulted in a single set of output $\left(C, \frac{h_\mathrm{r}}{h_\mathrm{m}}, \frac{\mathrm{d}P}{\mathrm{d}h}\big|_{h_\mathrm{m}}\right)$ which agreed well with the FEM-predicted $P-h$ response.

Similarly for the reverse problem, the 76 cases of the forward analysis (output) results were used as input to verify the reversibility of the reverse analysis algorithms proposed in Fig. 2-13. In only two cases, $\left(\frac{\sigma_\mathrm{y}}{E}, n\right) = (0.033, 0.5)$ and (0.04, 0.5) with very high hardening ($n = 0.5$), the reverse analysis yielded two solutions of n (E^* and σ_r still gave the correct answers). Reverse analysis on the remaining 74 cases resulted in a single, accurate re-construction of the initial elasto-plastic parameters.

As established in the literature (e.g., [27, 34, 38]), E^* may be uniquely obtained from a single $P-h$ curve via Eq. (2.26). Alternatively, noting that $p_\mathrm{ave} = \frac{P_\mathrm{m}}{A_\mathrm{m}}$, it is readily shown that dimensionless functions Π_4 and Π_6 can be combined to solve for E^* and A_m. From known E^*, the dimensionless function Π_1 can be used to determine the value of $\sigma_{0.033}$ (see Fig. 2-8(b)). Consequently, after both E^* and $\sigma_{0.033}$ are determined, strain hardening exponent n can be determined by dimensionless function Π_2 or Π_3 (see Figs. 2-10(a) and (b)). It was found in the current study that, *when the assumptions of the model are valid*, a single value for E^* and $\sigma_{0.033}$ can be determined for all cases. Furthermore, except for cases where $\frac{\sigma_\mathrm{y}}{E} \geqslant 0.033$ and $n > 0.3$, one single value of n can be determined as well. (although both σ_y and n are highly sensitive to even small variation in $P-h$ response) Examining Fig. 2-10(a) in detail, when $\frac{\sigma_\mathrm{y}}{E} \geqslant 0.033$ $\left(\frac{\sigma_\mathrm{y}}{E^*} \geqslant 0.03\right)$ and $n > 0.3$, the $n = 0.5$ curve crossed the other three curves, which indicates the solution of n may not be unique using dimensionless function Π_2 in that region; a single solution of n may be obtained using dimensionless function Π_3 instead. The above arguments regarding uniqueness can only be valid when the $P-h$ responses can be measured accurately and precisely. Therefore,

Table 2.7: Uniqueness of reverse analysis

Mechanical Property		Solution unique?
E^*		Yes
Hardness (p_{ave})		Yes
σ_{r}		Yes
σ_{y}	when $n \leqslant 0.3$	Yes
	when $0.3 < n \leqslant 0.5$ and $\frac{\sigma_{\text{y}}}{E^*} < 0.03$	Yes
	when $0.3 < n \leqslant 0.5$ and $\frac{\sigma_{\text{y}}}{E^*} \geqslant 0.03$	?

with accurate $P-h$ curves, the uniqueness of the reverse problem can be ensured for low hardening materials (i.e., $n \leqslant 0.3$); the uniqueness can also be preserved if $\frac{\sigma_{\text{y}}}{E^*} < 0.03$ for higher hardening materials (i.e., $0.3 < n \leqslant 0.5$). Considering the fact that each of the dimensionless functions Π_1, Π_2, ..., and Π_6 carries a small amount of uncertainty, definitive conclusion can not be drawn as yet regarding the uniqueness of the reverse analysis when $\frac{\sigma_{\text{y}}}{E^*} \geqslant 0.03$ and $0.3 < n \leqslant 0.5$. Table 2.7 summarizes the above mentioned results.

Cheng and Cheng [40] examined whether uniaxial stress-strain relationships of materials can be uniquely determined by matching the loading and unloading $P-h$ curves, calculated using their FEM analysis and scaling relationships, with those measured experimentally. By showing that there could be multiple stress-strain curves for a given set of loading and unloading curves, the conclusion was that the material stress-strain behavior may not be uniquely determined from the loading and unloading $P-h$ response alone. All seven cases presented in [40] were examined. For the four cases presented in Fig. 3(a) of Ref. [40], the values of $\frac{\sigma_{\text{y}}}{E^*}$ are beyond the range of the current study. That is, the ratio of $\frac{\sigma_{\text{y}}}{E^*}$ given by these four cases ($\sim 10^{-1}$) may not accurately describe any metallic engineering alloys (see, e.g., [58]), but may describe certain ceramics or engineering polymers, which are not well-described by power law plasticity. Therefore, the non-uniqueness of these cases is physically irrelevant to the scope of our analysis. In contrast, the cases reported in Fig. 3(b) of Ref. [40] are within our range of parameters $\left(\frac{\sigma_{\text{y}}}{E^*} \sim 10^{-2} \text{ to } 10^{-3}\right)$. The current forward analysis predicts three $P-h$ responses which are statistically unique in terms of

the calculated curve parameters such as C, $\frac{h_r}{h_m}$, $\frac{dP}{dh}\big|_{h_m}$. This statistical uniqueness does not directly contradict Cheng and Cheng's assertion of non-uniqueness, as they used a different apex angle in their FEM simulations, and as the $P-h$ curves appear visually similar. The maximum variation in curve parameters calculated by our forward analysis of these three cases was an 8% change in $\frac{dP}{dh}\big|_{h_m}$. The present reverse analysis provides a unique solution in that, even if the calculated loading curvatures (C) were mathematically identical for two separate $P-h$ responses, small variations in terms of $\frac{dP}{dh}\big|_{h_m}$ or $\frac{h_r}{h_m}$ are sufficient to calculate a unique value of n and, consequently, a unique value of σ_y for each case. However, these small variations in curve parameters may not be visually apparent when plotting these $P-h$ responses simultaneously. In fact, as experimental scatter may cause such variation in $P-h$ curve parameters, the issue of sensitivity in these analyses is an important consideration.

2.4.2 Sensitivity to Forward Analysis, Reverse Analysis and Apex Angle

For forward analysis, the sensitivity of the predicted $P-h$ response parameters to variations in the input mechanical properties of the indented material was investigated for the 76 cases examined in this study. The results showed that a $\pm 5\%$ change in any one input parameter (i.e., E^*, σ_y or n), would lead to variations of less than $\pm 6\%$ in the predicted results $\left(C, \frac{h_r}{h_m}, \frac{dP}{dh}\big|_{h_m}\right)$.

As discussed in Venkatesh *et al.* [42], the accuracy with which the mechanical properties of the indented material can be estimated through reverse analysis could depend strongly on the accuracy with which the $P-h$ responses are measured. The sensitivity of the estimated mechanical properties to variations in the input parameters obtained from the $P-h$ curves was investigated for the 76 cases examined in this study, as well. For each of these cases, the sensitivity of the estimated elasto-plastic properties to variations in the three $P-h$ curve parameters$-C$, $\frac{dP}{dh}\big|_{h_m}$, and $\frac{W_p}{W_t}-$about their respective reference values (as estimated from the forward analysis) was examined. The results are summarized in Table 2.8. In general, sensitivity to reverse analysis is different for each individual case, thus the maximum variations listed in Table 2.8 are conservative estimates. For a more practical interpretation of the sensitivity to reverse analysis, Fig. 2-17 shows statistical results through the average values and the error bar indicating 99% confidence interval (not

Table 2.8: Sensitivity to reverse analysis

Maximum variations in estimated properties[a]	Changes in input parameters: ±2% in C	±2% in $\frac{\mathrm{d}P}{\mathrm{d}h}\big\vert_{h_\mathrm{m}}$	±0.25% in $\frac{W_\mathrm{p}}{W_\mathrm{t}}$	±4% in C	±4% in $\frac{\mathrm{d}P}{\mathrm{d}h}\big\vert_{h_\mathrm{m}}$	±0.5% in $\frac{W_\mathrm{p}}{W_\mathrm{t}}$
E^*	∓2%	±4%	∓9.5%	∓4%	±8%	∓19%
$\sigma_{0.033}$	+12%/-10%	-8%/+11%	0.9%	+29%/-19%	-15%/+25%	±1.7%
σ_y^b ($n \leqslant 0.1$)	+18%/-24%	-22%/+16%	+31%/-45%	+28%/-43%	-39%/+24%	+39%/-96%
σ_y^b ($n \geqslant 0.1$)	+85%/-29%	-27%/+81%	+70%/-33%	+103%/-53%	-50%/+96%	+71%/-57%
p_ave	∓2%	±4%	-18%/+20%	∓4%	±8%	-34%/+42%

[a] All errors were computed as $\frac{X_\mathrm{varied}-X_\mathrm{reference}}{X_\mathrm{reference}}$, where X represents a variable.
[b] Estimated by setting n=0 when there are multiple solutions or no solution for n, or setting n=0.5 when the solution for n is greater than 0.5 (which is outside the scope of our parameter study)

just the maximum variation as shown in Table 2.8).

It is evident that E^* displayed weak sensitivity with respect to C and $\frac{\mathrm{d}P}{\mathrm{d}h}\big\vert_{h_\mathrm{m}}$, and strong sensitivity to $\frac{W_\mathrm{p}}{W_\mathrm{t}}$; σ_r displayed moderate sensitivity to C, $\frac{\mathrm{d}P}{\mathrm{d}h}\big\vert_{h_\mathrm{m}}$ and $\frac{W_\mathrm{p}}{W_\mathrm{t}}$; for low hardening materials ($n \leqslant 0.1$), σ_y displayed moderate sensitivity to C and $\frac{\mathrm{d}P}{\mathrm{d}h}\big\vert_{h_\mathrm{m}}$, and strong sensitivity to $\frac{W_\mathrm{p}}{W_\mathrm{t}}$; for higher hardening materials ($n > 0.1$), σ_y displayed strong sensitivity to all three parameters; p_ave displayed weak sensitivity to C and $\frac{\mathrm{d}P}{\mathrm{d}h}\big\vert_{h_\mathrm{m}}$, and strong sensitivity to $\frac{W_\mathrm{p}}{W_\mathrm{t}}$. The results of the reverse sensitivity analysis shown in Table 2.8 are consistent with the reverse analyses of experimental $P-h$ curves listed in Table 2.6. The greater scatter in computed σ_y values in Table 2.6 reflects the stronger sensitivity with respect to σ_y. If data scatter is random in nature, it is expected that taking the averaged value from a number of indentation tests may significantly reduce the error, as clearly demonstrated in Table 2.6.

In addition, the sensitivity of the $P-h$ response as computed from FEM calculations to variations in the apex angle θ of the indenter was investigated for the four cases A, B, C and D listed in Table 2.1. The results are summarized in Table 2.9 and Fig. 2-18, where the respective reference values (as calculated from the FEM computed $P-h$ curves) were taken at $\theta = 70.3^o$. From Fig. 2-18 and Table 2.9, the dependence of C, $\frac{\mathrm{d}P}{\mathrm{d}h}\big\vert_{h_\mathrm{m}}$ and $\frac{W_\mathrm{p}}{W_\mathrm{t}}$ to variations in the apex angle appears to be quite significant and approximately linear.

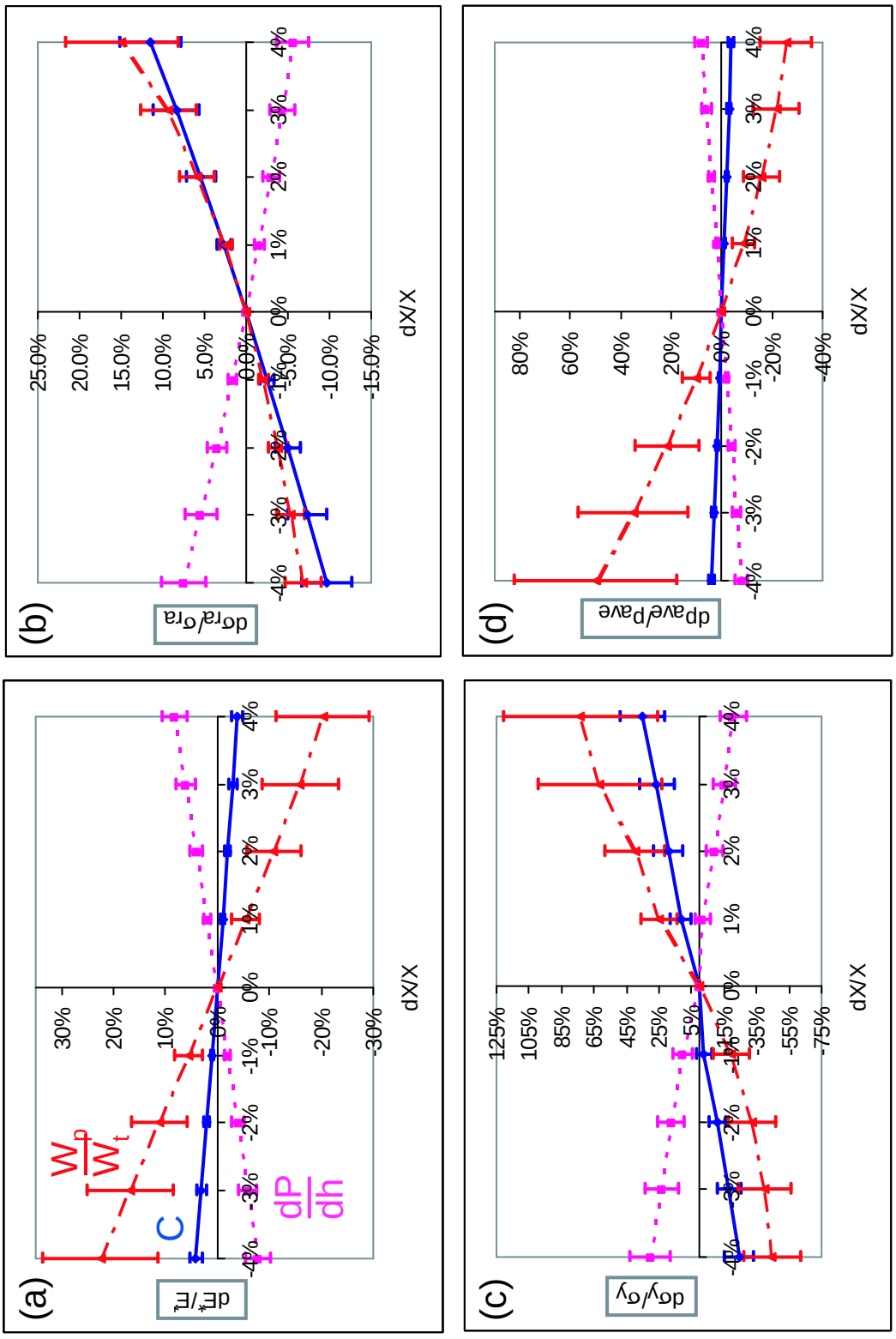

Figure 2-17: Sensitivity charts for reverse analysis showing the average variations in (a) E^*, (b) $\sigma_{0.033}$, (c) σ_{y} and (d) p_{ave} due to $\pm 4\%$ perturbation in C (solid line), $\frac{\mathrm{d}P}{\mathrm{d}h}\big|_{h_{\mathrm{m}}}$ (dotted line) and $\frac{W_{\mathrm{p}}}{W_{\mathrm{t}}}$ (dash-dotted line), with the error bar indicating 99% confidence interval.

Table 2.9: Apex angle sensitivity of A, B, C, and D (four cases)

Maximum variations \ Apex angle	68^o	69^o	70.3^o (reference)	72^o
$\Delta C \ / \ C_{\text{ref}}$	-20.4%	-12.1%	0%	+19.3%
$\Delta\left(\frac{\mathrm{d}P}{\mathrm{d}h}\right) / \left(\frac{\mathrm{d}P}{\mathrm{d}h}\right)_{\text{ref}}$	-11.7%	-7.7%	0%	+9.0%
$\Delta\left(\frac{W_{\text{p}}}{W_{\text{t}}}\right) / \left(\frac{W_{\text{p}}}{W_{\text{t}}}\right)_{\text{ref}}$	+5.7%	+3.0%	0%	-4.8%

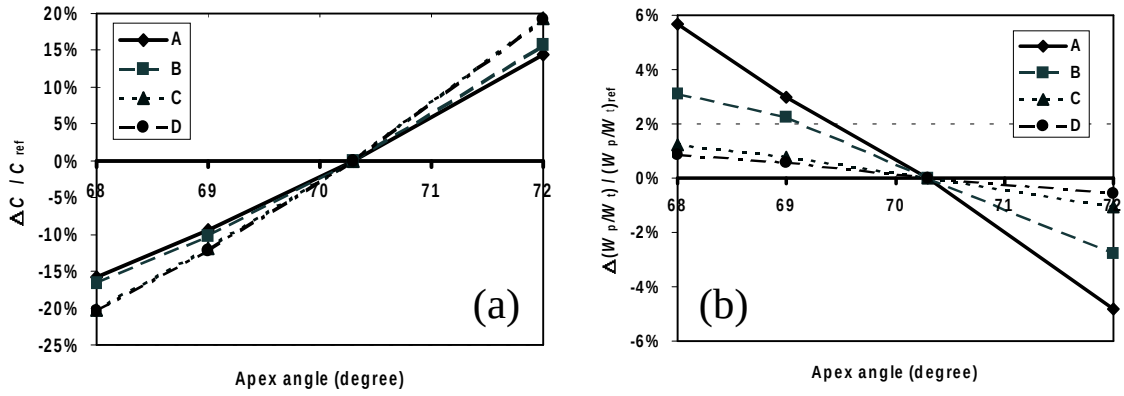

Figure 2-18: Sensitivity of (a) loading curvature C and (b) plastic work ratio $\frac{W_{\text{p}}}{W_{\text{t}}}$ to variations in apex angle for four model materials. A two-degree variation in apex angle resulted in 15-20% variations in loading curvature C and up to 6% variations in plastic work ratio $\frac{W_{\text{p}}}{W_{\text{t}}}$.

Taking $\theta = 68^{\circ}$ as used in [33, 34, 40] as an example, deviation from the reference apex angle by 2.3° results in maximum variations of -20%, -11.7% and +5.7% in terms of C, $\frac{\mathrm{d}P}{\mathrm{d}h}\big|_{h_{\mathrm{m}}}$ and $\frac{W_{\mathrm{p}}}{W_{\mathrm{t}}}$ respectively (see Table 2.9). As evident in Table 2.8, variations of this magnitude are beyond the error tolerance limit of reverse analysis. The universal functions based on a 68° apex angle may significantly differ from those obtained using a 70.3° apex angle, although certain trends with respect to various parameters may be similar. As commercially available diamond indenters normally come with the specification of the apex angle within ±0.5°. The resulting maximum variations in $P - h$ curve parameters as estimated from FEM computations are around ±3%, ±3%, and ±1% in terms of C, $\frac{\mathrm{d}P}{\mathrm{d}h}\big|_{h_{\mathrm{m}}}$ and $\frac{W_{\mathrm{p}}}{W_{\mathrm{t}}}$ respectively, which are within the error tolerance limit of the reverse analysis.

2.4.3 Representative Strains

The concept of representative strain was first introduced by Tabor [23] to relate its corresponding representative stress to the hardness value. Tabor [23] suggested a representative plastic strain of 8-10% based on experimental observations. This original definition does not represent any apparent physical transition in mechanical response. Giannakopoulos *et al.* [3] and Giannakopoulos and Suresh [41] used a "characteristic strain" of 29-30% within the context of Eq. (2.23). Giannakopoulos and Suresh [41] suggested that the region of material experiencing strains beyond 29% under the indenter exhibits plastic "cutting" characteristics and may be modeled using slip line theory. In the current study, a representative plastic strain $\varepsilon_{\mathrm{r}} = 0.033$ was identified as a strain level which allows for the construction of a dimensionless description of the indentation loading response (i.e., Eq. (2.12)), independent of strain hardening exponent n. Here, the underlying connections between these three different definitions and the corresponding representative strain levels are discussed.

To understand these different representative strain values, it is important to note that the dimensionless function Π_1 in Fig. 2-8(b), used to identify $\varepsilon_{\mathrm{r}} = 0.033$ has a different functional form than that used by the earlier researchers, e.g., Eq. (2.23). Therefore, it is possible for these different definitions to result in different solutions. Equation (2.24) is a modification of Eq. (2.23) and, as mentioned in Section 2.2.5, can fit all 76 cases studied reasonably well. For low strain hardening materials, $\sigma_{0.29} \approx \sigma_{\mathrm{r}} (\approx \sigma_{\mathrm{y}})$, and thus Eq. (2.24)

can be rewritten as

$$\begin{aligned} C &\approx N_1\sigma_{0.29}\left(1+\frac{\sigma_{\mathrm{y}}}{\sigma_{0.29}}\right)\left[N_2+\ln\left(\frac{E^*}{\sigma_{\mathrm{r}}}\right)\right] \\ &= \left(\frac{\sigma_{\mathrm{y}}+\sigma_{0.29}}{2}\right)\left\{2N_1\left[N_2+\ln\left(\frac{E^*}{\sigma_{\mathrm{r}}}\right)\right]\right\} \\ &= \left(\frac{\sigma_{\mathrm{y}}+\sigma_{0.29}}{2}\right)\Pi_{1\mathrm{N}}\left(\frac{E^*}{\sigma_{\mathrm{r}}}\right) \end{aligned} \tag{2.30}$$

within a 5.5% error of Eq. (2.24) for all the 76 cases computed in the current study; $\Pi_{1\mathrm{N}}$ is a dimensionless function. One can solve for ε_{r} that gives σ_{r} as an arithmetic average between σ_{y} and $\sigma_{0.29}$:

$$\sigma_{\mathrm{r}} = \frac{\sigma_{\mathrm{y}}+\sigma_{0.29}}{2} \tag{2.31}$$

If it is assumed that $\sigma_{\mathrm{y}} \approx \sigma|_{\varepsilon=0.002}$, then Eq. (2.31) becomes

$$R\varepsilon_{\mathrm{r}}^n \approx \frac{R\cdot 0.002^n + R\cdot 0.29^n}{2} \tag{2.32}$$

and thus

$$\varepsilon_{\mathrm{r}} \approx \left(\frac{0.002^n+0.29^n}{2}\right)^{\frac{1}{n}} \tag{2.33}$$

For low hardening materials with $0 < n < 0.15$, Eq. (2.33) gives $0.024 < \varepsilon_{\mathrm{r}} < 0.038$, which is fairly close to 0.033. This exercise indicates that: (1) $\varepsilon_{\mathrm{r}} = 0.033$ obtained in the current study is fundamentally linked to the "characteristic strain" of 0.29 given in the literature, and the differences in the magnitude of the strain come from their different functional definitions; (2) $\sigma_{0.033}$ taken at the 0.033 representative strain is a "weighted average" of the stresses over the range between ε_{y} and $\varepsilon_{\mathrm{p}} = 0.29$. Additional computations confirmed that stress-strain behavior beyond $\varepsilon_{\mathrm{p}} = 0.29$ has little effect on a material's $P-h$ response.

Earlier studies by Tabor [23] and Johnson [37] gave a representative strain at about $\varepsilon_r = 0.08$. This estimation relied on experimental data which indicated that

$$\frac{H}{\sigma_r} = \frac{p_{ave}}{\sigma_r} \approx 3.0 \tag{2.34}$$

where H is the hardness expressed in units of pressure. Again, it is noted that the functional form defined by Eq. (2.34) is different from those used to define representative strains of 3.3% or 29%, and it is natural that different functions may lead to different results. To better understand this problem, a new dimensionless function can be defined

$$\frac{p_{ave}}{\sigma_r} = \Pi_9 \left(\frac{\sigma_r}{E^*}, n \right) \tag{2.35}$$

Similar to the procedure taken to obtain $\sigma_r = 0.033$ (see Fig. 2-8), errors were minimized using the least squares method to fit results obtained from the 76 cases studied. It was found that when $\sigma_r = 0.082$, a best fit function within a $\pm 5.96\%$ error was achieved with the following n-independent function

$$\Pi_9 = \frac{p_{ave}}{\sigma_{0.082}} \approx -15.4944 \left(\frac{\sigma_{0.082}}{E^*} \right)^2 - 15.1699 \left(\frac{\sigma_{0.082}}{E^*} \right) + 2.7497 \tag{2.36}$$

A representative strain of $\sigma_r = 0.082$ was thus identified. Figure 2-19 shows Eq. (2.36) plotted against the FEM data. Also plotted in Fig. 2-19 are the four cases studied in Section 2.2.5. Equation (2.36) predicts $\Pi_9 = \frac{p_{ave}}{\sigma_{0.082}} \approx 2.75$ for both steel and aluminum listed in Table 2.1. It is noted that, in Tabor's original study [23], when there was no pre-straining, $\frac{p_{ave}}{\sigma_{0.08}}$ was found to be 2.6 and 2.84 (instead of being very close to 3.0) for annealed copper and mild steel, respectively; this is in good agreement with the predictions from Π_9.

Although different functional definitions were used by Tabor and the present study, the same set of modeling assumptions and fitting algorithms were used to derive a characteristic strain of 8.2%. This exercise shows that these two values are fundamentally linked to one another. Thus, the apparent disparity comes not from discrepancies in data, constitutive modeling, or fitting procedures, but rather from the choice of functional definitions that were used to relate certain indentation parameters to certain mechanical properties.

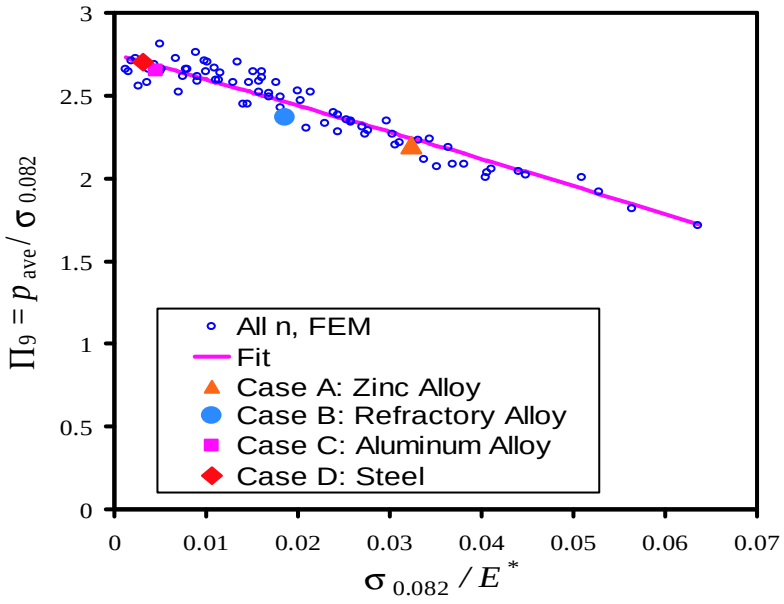

Figure 2-19: Dimensionless function Π_9. A best fit function within a $\pm 5.96\%$ error was achieved with a representative plastic strain $\varepsilon_r = 0.082$ and its corresponding stress $\sigma_{0.082}$

2.5 Conclusions

In this chapter, dimensional analysis and large deformation finite element studies were performed to elucidate the mechanics of instrumented sharp indentation. Systematic experiments were conducted to verify the theoretical results. The key results of this investigation can be summarized as follows.

1. Using dimensional analysis, a set of new universal, dimensionless functions was constructed to characterize instrumented sharp indentation. From these functions and elasto-plastic finite element computations, solutions were formulated to relate indentation data to elasto-plastic properties.

2. Forward and reverse analysis algorithms were established based on the identified dimensionless functions. These algorithms allow for the calculation of the indentation response for a given set of properties, and also for extraction of some elasto-plastic properties from a given set of indentation data, thus obviating the need for large-scale finite element computations after each indentation test.

3. The proposed forward analysis algorithms work well and robustly; a $\pm 5\%$ error in any input parameter results in less than $\pm 6\%$ in the predicted values of C, $\frac{\mathrm{d}P}{\mathrm{d}h}\big|_{h_\mathrm{m}}$ or $\frac{h_\mathrm{r}}{h_\mathrm{m}}$. Theoretical predictions compare well with experimental $P-h$ curves.

4. The proposed reverse analysis algorithms were found to predict E^* and $\sigma_{0.033}$ quite well, and σ_y reasonably well for the few cases studied. Although greater scatter was found in the computation of σ_y, the averaged value approached the experimentally measured yield strength σ_y. The average pressure p_ave also compared well with values estimated from experimental microhardness tests.

5. Assuming large deformation in FEM simulations and an isotropic power law elasto-plastic constitutive description of the material within the specified range of material parameters, except for cases where $\frac{\sigma_\mathrm{y}}{E} \geqslant 0.033$ and $n > 0.3$, the reverse algorithms were able to predict one single set of values for E^*, $\sigma_{0.033}$ and σ_y; furthermore, if the power law assumption holds, the full stress-strain response can be estimated.

6. For sharp indentation of power law hardening pure metals and alloys, a representative strain ε_r was identified at 3.3%. Within the same theoretical framework, it was demonstrated that the apparent disparities between the value of 3.3% identified in the current study and the values of 8% and 29% proposed in the literature stem from the different functional definitions used to obtain these values, rather than from any intrinsic differences in mechanistic interpretations.

7. A comparative study showed that the $P-h$ responses obtained using large deformation theory exhibited loading curvature C considerably greater than those obtained using small deformation theory.

8. Comprehensive sensitivity analyses were carried out for both forward and reverse algorithms. Forward analysis algorithms were found to be accurate and robust. For the sensitivity to reverse analysis, E^*, $\sigma_{0.033}$ and p_ave displayed weak or moderate sensitivity to variations in C, $\frac{\mathrm{d}P}{\mathrm{d}h}\big|_{h_\mathrm{m}}$, and $\frac{W_\mathrm{p}}{W_\mathrm{t}}$; for low hardening materials ($n \leq 0.1$), σ_y displayed moderate sensitivity to C and $\frac{\mathrm{d}P}{\mathrm{d}h}\big|_{h_\mathrm{m}}$, and strong sensitivity to $\frac{W_\mathrm{p}}{W_\mathrm{t}}$; for higher hardening materials ($n > 0.1$), σ_y displayed strong sensitivity to all three parameters. Sensitivity of the $P-h$ responses to apex angle deviations were found to be significant with even an $1-2^\mathrm{o}$ deviation; nevertheless, the $P-h$ response variations

with respect to apex angle deviations less than $\pm 0.5^{\circ}$ were within the tolerance limit of the reverse analysis.

9. It is noted that plastic properties of materials extracted from instrumented indentation are very sensitive to even small variation in the $P - h$ responses. Nevertheless, the present computational study provides a mean to determine these plastic properties, which may not be easily obtainable by other means in small volume structures, and further provides an indication of the level of the sensitivity to experimental indentation data.

Chapter 3

Depth-Sensing Instrumented Indentation with Dual Sharp Indenters

In this chapter*, a methodology for interpreting instrumented sharp indentation with dual sharp indenters with different tip apex angles is presented by recourse to computational modeling within the context of finite element analysis. The forward and reverse algorithms (as defined in Sections 2.3.2 and 2.3.3, respectively) were constructed on the basis of theoretical and computational foundations established in the previous chapter. This chapter also focuses on the uniqueness of the reverse algorithm and its sensitivity to variations in the measured indentation data in comparison with the single indentation analysis on Vickers/Berkovich tip, discussed in the previous chapter. Finite element computations were carried out for the same 76 combinations of elasto-plastic properties chosen in the previous chapter (see Table 2.2) for each tip geometry (i.e., 50°, 60° and 80° cones). Young's modulus, E, was varied from 10 to 210 GPa; yield strength, σ_y, from 30 to 3000 MPa; and strain hardening exponent, n, from 0 to 0.5; while the Poisson's ratio, ν, was fixed at 0.3. Using dimensional analysis, additional closed-form dimensionless functions were constructed to relate indentation response to elasto-plastic properties for each indenter tip geometry. The

*This article is published in *Acta. Mater.*, Vol. 51 (2003), p. 3713, with co-authors: M. Dao and S. Suresh. [59]

representative plastic strain ε_r, as defined in Section 2.3.1, was constructed as a function of tip geometry in the range of 50° and 80°. Incorporating the results from 60° tip to the single-indenter algorithms, the improved forward and reverse algorithms for dual indentation can be established. This dual-indenter reverse algorithm provides a unique solution of the reduced Young's modulus E^*, the hardness p_{ave} and two representative stresses (measured at two corresponding representative strains), which establish the basis for constructing power-law plastic material response. Comprehensive sensitivity analyses showed much improvement of the dual-indenter algorithms over the single-indenter results. Experimental verifications of these dual-indenter algorithms were carried out using a 60° half-angle cone tip (or a 60° cone equivalent 3-sided pyramid tip) and a standard Berkovich indenter tip for two materials: 6061-T651 and 7075-T651 aluminum alloys. Possible extensions of the present results to studies involving multiple indenters are also suggested.

3.1 Introduction

The previous chapter on instrumented indentation involving a single sharp indenter established a set of dimensionless functions, which took into account the pile-up/sink-in effects and finite strain beneath the indenter. These functions were used to predict the indentation response from a given set of elasto-plastic properties (forward algorithms), and to extract the elasto-plastic properties from a given set of indentation data (reverse algorithms). A representative strain of $\varepsilon_r = 3.3\%$ for a Berkovich or Vickers indenter (equivalent to a 70.3° cone) was identified with which the indentation loading curvature could be normalized independently of the material hardening exponent for a very wide range of elasto-plastic properties (see Section 2.3.1). For most common metallic systems, a single set of elasto-plastic properties was extracted from a single $P - h$ curve. The accuracy of the analysis, however, was found to be sensitive to the small experimental errors (see Section 2.4.2). Cheng and Cheng [40] and Venkatesh *et al.* [42] discussed the uniqueness issue and the former presented a number of computationally non-unique cases.

It is clear that two important fundamental issues remain which require further investigation:

1. Uniqueness of the reverse analysis for the range of material properties examined; and
2. The accuracy and sensitivity of the reverse analysis.

In this chapter, these issues will be addressed within the context of dual sharp indentation, continuum analysis and experimental observations.

3.2 Framework for Analysis

3.2.1 Problem Formulation and Nomenclature

A comprehensive framework using dimensional analysis to extract closed form universal functions was developed in the previous chapter. A representative plastic strain ε_{r} was identified as a strain level which allows for the construction of a dimensionless description of indentation loading response, independent of strain hardening exponent n; $\varepsilon_{\mathrm{r}} = 3.3\%$ for Berkovich, Vickers or 70.3° apex-angle cone tip. It was also found that for most cases, three independent quantities$-C$, $\frac{\mathrm{d}P}{\mathrm{d}h}\big|_{h_{\mathrm{m}}}$, and $\frac{h_{\mathrm{r}}}{h_{\mathrm{m}}}-$obtained from a single $P-h$ curve are sufficient to uniquely determine the indented material's elasto-plastic properties under certain ranges of validity (see Table 2.7). Although the estimation of σ_{y} and n in certain ranges could be prone to considerable sensitivity from a variation in these three $P-h$ characteristics (see Table 2.8), a reverse analysis algorithm proposed in Section 2.3.3 predicts stress at representative strain, $\sigma_{0.033}$, robustly.

It is expected that, with different indenter geometries (i.e. different apex angles), the representative strain would be different (e.g. $\varepsilon_{\mathrm{r}} = \varepsilon_{\mathrm{r}}(\theta)$). In fact, a $\pm 2^{\mathrm{o}}$ variation in apex angle can result in a $\pm 20\%$ change in loading curvature C (see Fig. 2-18). This observation suggests a possibility of determining σ_{y} and n more precisely using dual indenter geometries (two representative stresses). An additional representative stress σ_{r} can be identified from a loading curvature of a $P-h$ curve using a second indenter of which its tip geometry is different from Berkovich/Vickers. The question remains whether two $P-h$ curves from two different indenter tips can yield unique solution for a broader range of material's elasto-plastic properties with improved accuracy than previously demonstrated with a single indentation.

3.2.2 Dimensional Analysis and Universal Functions

For a sharp indenter of apex angle θ, the load required to penetrate into a power law elasto-plastic solid (E, ν, $\sigma_{\rm y}$ and n) can be written as

$$P = P(h, E^*, \sigma_{\rm y}, n, \theta), \tag{3.1}$$

where E^* is reduced Young's modulus (as defined in Eq. (2.8)), commonly introduced [49] to include elasticity effect ($E_{\rm i}, \nu_{\rm i}$) of an elastic indenter. Define $\sigma_{\rm r}$ as the stress at the representative strain $\varepsilon_{\rm r}$ in Eq. (2.5); Eq. (3.1) can be rewritten as

$$P = P(h, E^*, \sigma_{\rm r}, n, \theta), \tag{3.2}$$

Using dimensional analysis (see Section 2.2.2, Eq. (3.2) becomes

$$P = \sigma_{\rm r} h^2 \Pi_{1\theta} \left(\frac{E^*}{\sigma_r}, n, \theta \right) \tag{3.3}$$

and from Kick's law, as defined in Eq. 2.1

$$C = \frac{P}{h^2} = \sigma_{\rm r} \Pi_{1\theta} \left(\frac{E^*}{\sigma_{\rm r}}, n, \theta \right) \tag{3.4}$$

where $\Pi_{1\theta}$ is a dimensionless function.

A complete set of universal dimensionless functions for a single indenter is listed in Appendix A.1 (Eqs. (A.1)-(A.6)) for an apex angle of 70.3$^{\rm o}$ (Berkovich and Vickers equivalent). In the this chapter, $\Pi_{1\theta}$ functions at different apex angles (e.g. 50$^{\rm o}$, 60$^{\rm o}$ or 80$^{\rm o}$) will be constructed. The original algorithms in the previous chapter can be modified to accurately predict the $P-h$ response from known elasto-plastic properties (forward algorithms) and to systematically and uniquely extract the indented material's elasto-plastic properties from two sets of $P-h$ data of two different indenter geometries (reverse algorithms).

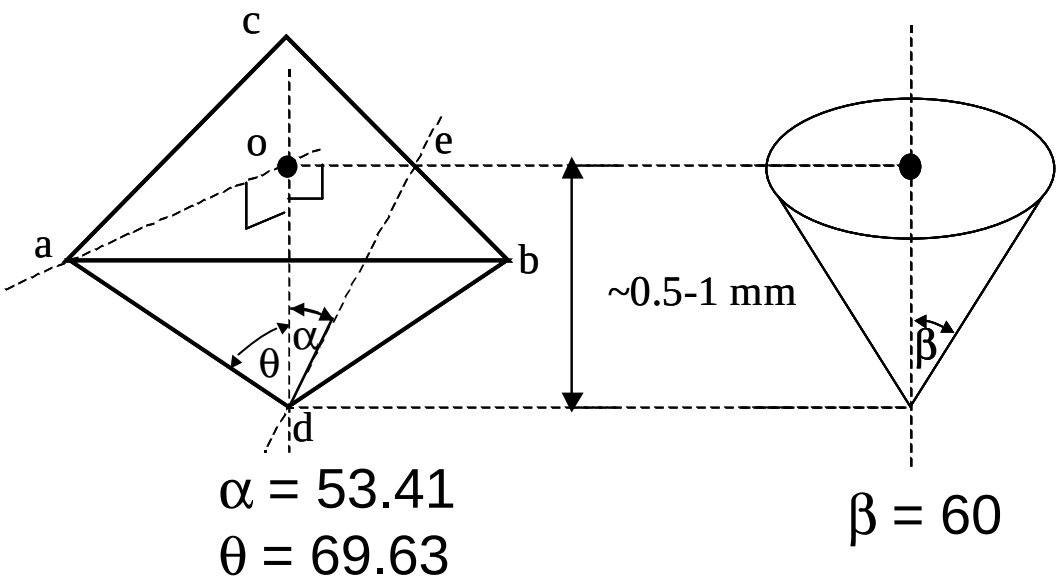

Figure 3-1: Schematic drawing of the customized 60° cone and 60° cone equivalent 3-sided pyramid with the appropriate angles such that the projected area at a given depth is the same.

3.2.3 Computational Model

It is generally known that axisymmetric two-dimensional finite element model can be used to capture the result of full three-dimensional model as long as the projected area/depth of the two models are equivalent (see Section 2.2.3). Computations were performed using the general purpose finite element package ABAQUS [52]. For both Berkovich and Vickers indenters, the corresponding apex angle θ (see Fig. 2-3) of the equivalent cone was calculated to be 70.3°. The detail of mesh design was modified from Fig. 2-3 such that at the maximum load, the minimum number of contact elements in the contact zone was no less than 12 in each FEM computation. The mesh was well-tested for convergence and was determined to be insensitive to far-field boundary conditions. In all finite element computations, the indenter was modeled as a rigid body; the contact was modeled as frictionless; and large deformation FEM computations were performed

3.2.4 Comparison of Experimental and Computational Results

The same two aluminum alloys (6061-T651 and 7075-T651) were prepared, as described in Section 2.2.4, for indentation using a Berkovich tip and a second indenter tip with different geometry. The specimens were indented on a commercial nanoindenter (MicroMaterials, Wrexham, UK) with the Berkovich, 60° cone and 60° cone equivalent 3-sided pyramid at a loading/unloading rate of approximately 4.4 N/min. Figure 3-1 shows the schematic drawing of the 60° cone and 60° cone equivalent 3-sided pyramid with the appropriate angles. For the Berkovich tip, the maximum loads for both aluminum alloys were 3 N with a repetition of 6 tests. For the other two indenter tips, the Al6061-T651 specimens were indented to 1.8 and 2.7 N with a repetition of 3 and 10 tests, respectively; whereas the Al7075-T651 specimens were indented to 3 N with a repetition of 6 tests. From all the tests, the data were repeatable. For comparison with the single indentation results, the Berkovich indentation data of Al6061-T6511 specimens examined in the current chapter were taken directly from Table 2.5.

Figure 3-2(a) shows the typical indentation response of the 6061-T651 aluminum specimens under Berkovich and 60° cone indenter tips, superimposed with the corresponding finite element computations. Figure 3-2(b) shows the same for the 7075-T651 aluminum. Using experimental uniaxial compression (see Fig 2-4) as an input for the simulation, the resulting $P - h$ curves agree well with the experimental curves, as demonstrated in Figs. 3-2(a) and 3-2(b).

3.3 Computational Results

A comprehensive parametric study of 76 cases was conducted (see Table 2.2 for a complete list of parameters) representing the range of parameters of mechanical behavior found in common engineering metals. Values of Young's modulus E ranged from 10 to 210 GPa, yield strength σ_y from 30 to 3000 MPa, strain hardening exponent n from 0 to 0.5, and Poisson's ratio ν was fixed at 0.3. The axisymmetric finite element model was used to obtain computational results, unless otherwise specified.

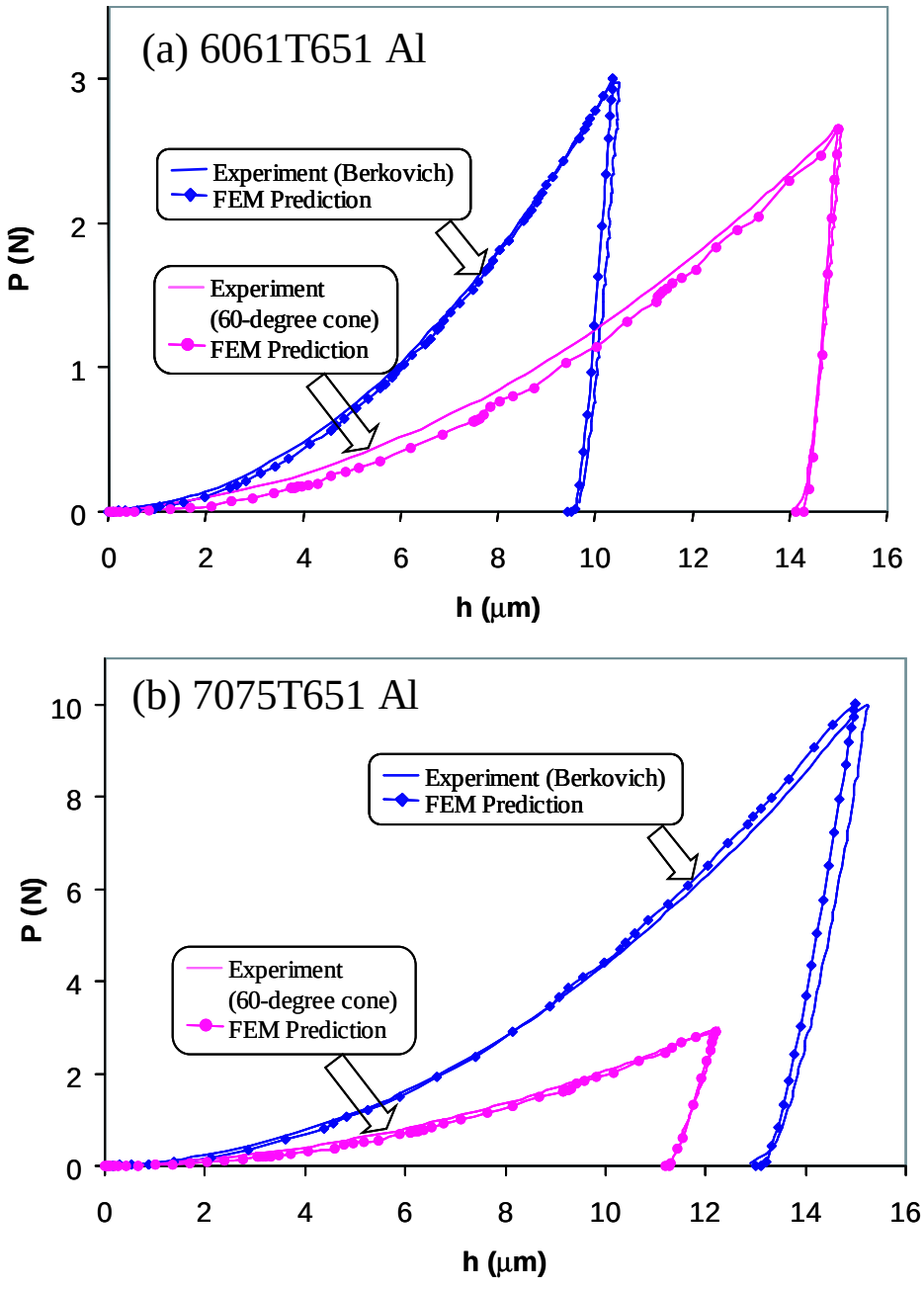

Figure 3-2: Experimental (Berkovich and 60° cone tips) versus computational indentation responses of both (a) 6061-T651 and (b) 7075-T651 aluminum specimens.

The dimensionless functions $\Pi_{1\theta}$ for different apex angles (e.g. 50°, 60° or 80°) were constructed in addition to the $\Pi_{1\theta}$ function at 70.3° angle (Berkovich and Vickers equivalent) presented earlier in Section 2.3.1. It is noted that the apex angle of 60° is commonly used in commercial indenters for scanning the surface profile or performing indentation tests. The second indenter tip geometry is chosen to be 60° cone.

3.3.1 Representative Strain and Dimensionless Function Π_1 as a Function of Indenter Geometry

The first dimensionless function of interest is $\Pi_{1\theta}$ in Eq. (3.4). Using subscript "a" to denote $\theta = 70.3^{\circ}$ in eq. (3.4), it follows that

$$\Pi_{1\mathrm{a}}\left(\frac{E^*}{\sigma_{\mathrm{r,a}}}, n, \theta = 70.3^{\circ}\right) = \frac{C_{\mathrm{a}}}{\sigma_{\mathrm{r,a}}} \tag{3.5}$$

It was found in Section 2.3.1 that for $\theta = 70.3^{\circ}$ a representative strain of 0.033 could be identified, such that a polynomial function $\Pi_{1\mathrm{a}}\left(\frac{E^*}{\sigma_{0.033}}\right) = \frac{C_{\mathrm{a}}}{\sigma_{0.033}}$ fits all 76 data points within a $\pm 2.85\%$ error†. It is worth noting that the corresponding dimensionless function $\Pi_{1\mathrm{a}}$ normalized with respect to $\sigma_{0.033}$ was found to be independent of the strain hardening exponent n.

Following the same procedure, one can identify the $\Pi_{1\theta}$ functions with different apex angles (i.e. different tip geometries). Three additional angles were studied here. For $\theta = 60^{\circ}$, a representative strain of 0.057 could be identified, where a closed-form function $\Pi_{1\mathrm{b}}\left(\frac{E^*}{\sigma_{0.057}}\right) = \frac{C_{\mathrm{b}}}{\sigma_{0.057}}$† fits all 76 data points within a $\pm 2.51\%$ error; here the subscript"b" is used to denote the case for $\theta = 60^{\circ}$. For $\theta = 80^{\circ}$, a representative strain of 0.017 could be identified, where a closed form function $\Pi_{1\mathrm{c}}\left(\frac{E^*}{\sigma_{0.017}}\right) = \frac{C_{\mathrm{c}}}{\sigma_{0.017}}$† fits all 76 data points within a $\pm 2.71\%$ error; here the subscript "c" is used to denote the case for $\theta = 80^{\circ}$. For $\theta = 50^{\circ}$, a representative strain of 0.082 could be identified, where a closed-form function $\Pi_{1\mathrm{d}}\left(\frac{E^*}{\sigma_{0.017}}\right) = \frac{C_{\mathrm{d}}}{\sigma_{0.017}}$† fits all 76 data points within a $\pm 2.49\%$ error; here the subscript "d" is used to denote the case for $\theta = 50^{\circ}$. The representative strain can be correlated with the half tip angle via a simple linear function (see Fig. 3-3(a))

†See Appendix A.2 for a complete listing of functions.

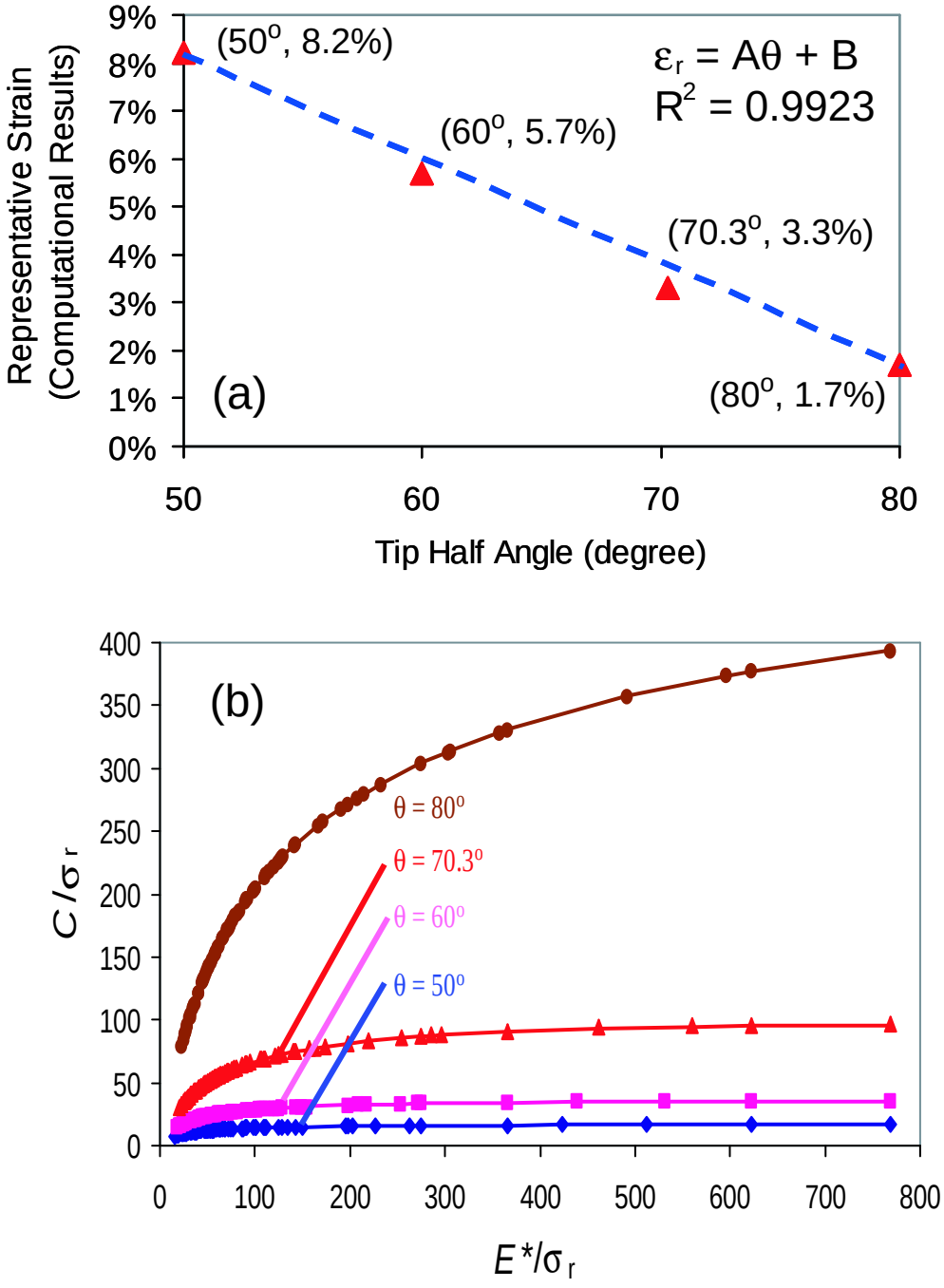

Figure 3-3: (a) A relationship between representative strain and indenter apex angle. (b) A generalized dimensionless function $\Pi_{1\theta}$ for $\theta = 50^{o}$, 60^{o}, 70.3^{o} and 80^{o}.

$$\varepsilon_{\mathrm{r}}(\theta) = -2.185 \times 10^{-3}\theta + 0.1894 \qquad \text{for } \theta \text{ in degree} \tag{3.6}$$

or a more accurate quadratic function, within ±1.63% error,

$$\varepsilon_{\mathrm{r}}(\theta) = 2.397 \times 10^{-5}\theta^2 - 5.311 \times 10^{-3}\theta + 0.2884 \qquad \text{for } \theta \text{ in degree} \tag{3.7}$$

To extend the capability of the present dual indentation algorithm, the choice for the second indenter geometry can be chosen between 50° and 80°. By correlating the coefficients in eqs. (A.1), (A.7), (A.8) and (A.9) with apex angle θ, $\Pi_{1\theta}\left(\frac{E^*}{\sigma_{\varepsilon_{\mathrm{r}}}}, \theta\right) = \frac{C_\theta}{\sigma_{\varepsilon_{\mathrm{r}}}}$ fits all $4 \times 76 = 304$ data points within a ±3% error, as shown in Fig. 3-3(b).

3.3.2 Forward Analysis Algorithms

In the following sections, the dual indenter geometries of the 70.3° and 60° pair are examined. The forward analysis leads to prediction of the $P - h$ response from known elasto-plastic properties. Following the procedure outlined in Section 2.3.2, an updated forward analysis algorithm for generalized dual indentation is shown in Fig. 3-4. The complete prediction of $P - h$ response can be readily constructed for $\theta = 70.3°$ using dimensionless functions $\Pi_{1\mathrm{a}}$ to $\Pi_{6\mathrm{a}}$, while the prediction of loading curvature can be obtained for any $\theta \in [50°, 80°]$ using $\Pi_{1\theta}$.

To verify the accuracy of the proposed algorithms, uniaxial compression and Berkovich indentation experiments were conducted in two well-characterized materials: 6061-T6511 aluminum and 7075-T651 aluminum (see Fig. 2-4). Additional indentation experiments using a different tip geometry (either a 60° cone or an equivalent 3-sided pyramid) were performed on both 6061-T651 and 7075-T651 aluminum samples. The mechanical property values used in the forward analysis were obtained directly from Table 2.4, where (E, ν, σ_{y}, n) are (66.8 GPa, 0.33, 284 MPa, 0.08) and (70.1 GPa, 0.33, 500 MPa, 0.0122) for Al6061-T651 and Al7075-T651, respectively. Table 3.1(a)[‡] – (c) list the predictions from

[‡]Table 3.1(a) reproduced from Table 2.5 here for easier comparison.

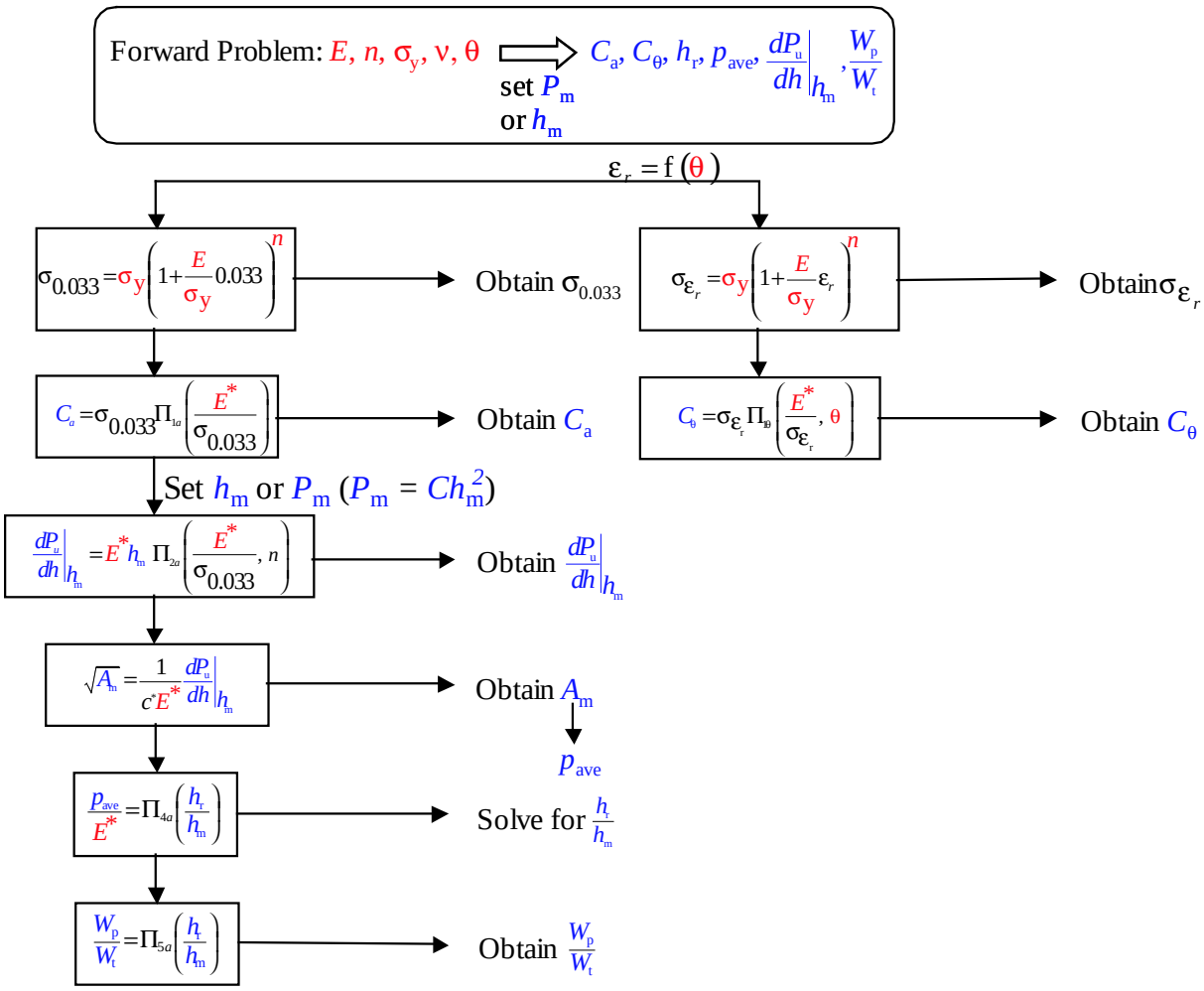

Figure 3-4: Dual Indentation Forward Analysis Algorithms.

the forward analysis (using Π_{1a} to Π_{6a} and Π_{1b}) for 6061-T651 aluminum specimens, along with the values extracted from the Berkovich indentation, the 60° cone indentation, and the 60° cone equivalent 3-sided pyramid indentation experiments, respectively. Table 3.2(a) − (b) lists the predictions from the forward analysis (using Π_{1a} to Π_{6a} and Π_{1b}) for 7075-T651 aluminum specimens, along with the values extracted from the Berkovich indentation and the 60° cone equivalent 3-sided pyramid indentation experiments, respectively. From Tables 3.1 and 3.2, it is evident that the present forward analysis results are in good agreement with the experimental $P - h$ curves.

3.3.3 Reverse Analysis Algorithms

Since a single $P-h$ curve is sufficient for estimation of the elasto-plastic properties, the use of two complete $P-h$ curves would give redundant information. Therefore, there are many possible ways to construct the reverse analysis algorithm; however, the most reliable path is presented here. The proposed reverse algorithm utilizes a complete $P-h$ curve obtained under Berkovich or Vickers indenter and a loading portion of a second $P-h$ curve under a conical indenter of apex angle $\theta \in [50^o, 80^o]$ (or its equivalent 3-sided pyramid). In the present study, $\theta = 60^o$ is chosen. The dimensionless functions Π_{1a} to Π_{6a} and $\Pi_{1\theta}$ allow us to construct an improved reverse algorithm. A set of the dual indentation reverse analysis algorithms is shown in Fig. 3-5.

To verify the dual indentation reverse algorithms, six Berkovich indentation curves shown in Table 3.1(a) and three 60° cone indentation curves shown in Table 3.1(b) from 6061-T651 aluminum specimens were first analyzed (using Π_{1a} to Π_{6a} and $\Pi_{1\theta}$). Table 3.3 shows the dual indentation results, along with part of the single indentation results from Table 2.6. In the reverse analyses, each case comprises one set of Berkovich indentation parameters shown in Table 3.1(a) and an average loading curvature C_b shown in Table 3.1(b) for the 60° cone indentation.

Additional verification for the dual indentation algorithms was performed on 7075-T651 aluminum specimens. Six Berkovich indentation $P-h$ curves shown in Table 3.2(a) and six 60° cone equivalent 3-sided pyramid indentation curves shown in Table 3.2(b) were analyzed (using Π_{1a} to Π_{6a} and $\Pi_{1\theta}$). Table 3.3(b) shows the dual indentation results, along

Table 3.1: Forward analysis on Al 6061-T651 indentation experiments using (a) Berkovich (max. load = 3 N) (b) 60^o cone (max. load = 1.8 N) and (c) 60^o cone equivalent 3-sided pyramid (max. load = 1.8 N).

Al 6061-T651	C [GPa]	%err C^a	$\frac{\mathrm{d}P}{\mathrm{d}h}\Big\vert_{h_\mathrm{m}}$	%err $\frac{\mathrm{d}P}{\mathrm{d}h}\Big\vert_{h_\mathrm{m}}$	$\frac{W_\mathrm{p}}{W_\mathrm{t}}$	%err $\frac{W_\mathrm{p}}{W_\mathrm{t}}$
			(a) Berkovich with P_m=3 N			
Test A1	27.4	-1.6%	4768	1.6%	0.902	0.8%
Test A2	28.2	1.2%	4800	2.3%	0.905	1.2%
Test A3	27.2	-2.4%	4794	2.2%	0.904	1.1%
Test A4	27.3	-2.2%	4671	-0.4%	0.889	-0.6%
Test A5	27.0	-3.2%	4762	1.5%	0.889	-0.6%
Test A6	27.6	-0.9%	4491	-4.2%	0.891	-0.4%
Ave	27.4		4715		0.896	
$STDEV^b$	0.6		110.9		0.007	
$STDEV/X_\mathrm{prediction}$	2.1%		2.4%		0.8%	
Forward Prediction^c	27.9		4691		0.894	
			(b) 60^o cone with P_m=1.8 N			
Test B1c	11.27	0.0%				
Test B2c	11.23	-0.4%				
Test B3c	11.32	0.5%				
Ave	11.27					
$STDEV^b$	0.04					
$STDEV/X_\mathrm{prediction}$	0.3%					
Forward Prediction^c	11.27					
			(c) 60^o cone equivalent 3-sided pyramid with P_m=1.8 N			
Test B1p	12.03	0.0%				
Test B2p	11.39	-0.4%				
Test B3p	11.97	0.5%				
Ave	11.80					
$STDEV^b$	0.60					
$STDEV/X_\mathrm{prediction}$	5.4%					
Forward Prediction^c	11.27					

[a] All errors were computed as $\frac{X_\mathrm{test}-X_\mathrm{prediction}}{X_\mathrm{prediction}}$, where X represents a variable.

[b] $STDEV = \sqrt{\frac{1}{N}\sum_{i=1}^{N}(X_\mathrm{test} - X_\mathrm{prediction})^2}$, where X represents a variable.

[c] Assume $\nu = 0.33$ and Berkovich c^*.

Table 3.2: Forward analysis on Al 7075-T651 indentation experiments using (a) Berkovich (max. load = 3 N) and (b) 60° cone equivalent 3-sided pyramid (max. load = 3 N).

Al 7075-T651	C [GPa]	%err C^a	$\frac{\mathrm{d}P}{\mathrm{d}h}\Big\vert_{h_\mathrm{m}}$	%err $\frac{\mathrm{d}P}{\mathrm{d}h}\Big\vert_{h_\mathrm{m}}$	$\frac{W_\mathrm{p}}{W_\mathrm{t}}$	%err $\frac{W_\mathrm{p}}{W_\mathrm{t}}$
(a) Berkovich with P_m=3 N						
Test A1	40.7	-7.1%	3636	1.4%	0.839	1.8%
Test A2	42.6	-2.8%	3637	1.4%	0.831	1.2%
Test A3	41.5	-5.5%	3498	-2.5%	0.829	1.1%
Test A4	40.7	-7.2%	3636	1.4%	0.835	-0.6%
Test A5	40.8	-7.0%	3566	-0.5%	0.834	-0.6%
Test A6	41.2	-6.0%	3600	0.4%	0.831	-0.4%
Ave	41.2		3595		0.833	
$STDEV^b$	1.6		51.7		0.00956	
$STDEV/X_\mathrm{prediction}$	3.7%		1.4%		1.2%	
Forward Prediction^c	43.9		3585		0.824	
(c) 60° cone equivalent 3-sided pyramid with P_m=3 N						
Test B1p	17.41	-7.9%				
Test B2p	17.52	7.4%				
Test B3p	16.95	-10.4%				
Test B4p	17.75	-6.2%				
Test B5p	18.08	-4.4%				
Test B6p	17.90	-5.4%				
Ave	17.60					
$STDEV^b$	1.37					
$STDEV/X_\mathrm{prediction}$	7.2%					
Forward Prediction^c	18.92					

[a] All errors were computed as $\frac{X_\mathrm{test}-X_\mathrm{prediction}}{X_\mathrm{prediction}}$, where X represents a variable.

[b] $STDEV = \sqrt{\frac{1}{N}\sum_{i=1}^{N}(X_\mathrm{test} - X_\mathrm{prediction})^2}$, where X represents a variable.

[c] Assume $\nu = 0.33$ and Berkovich c^*.

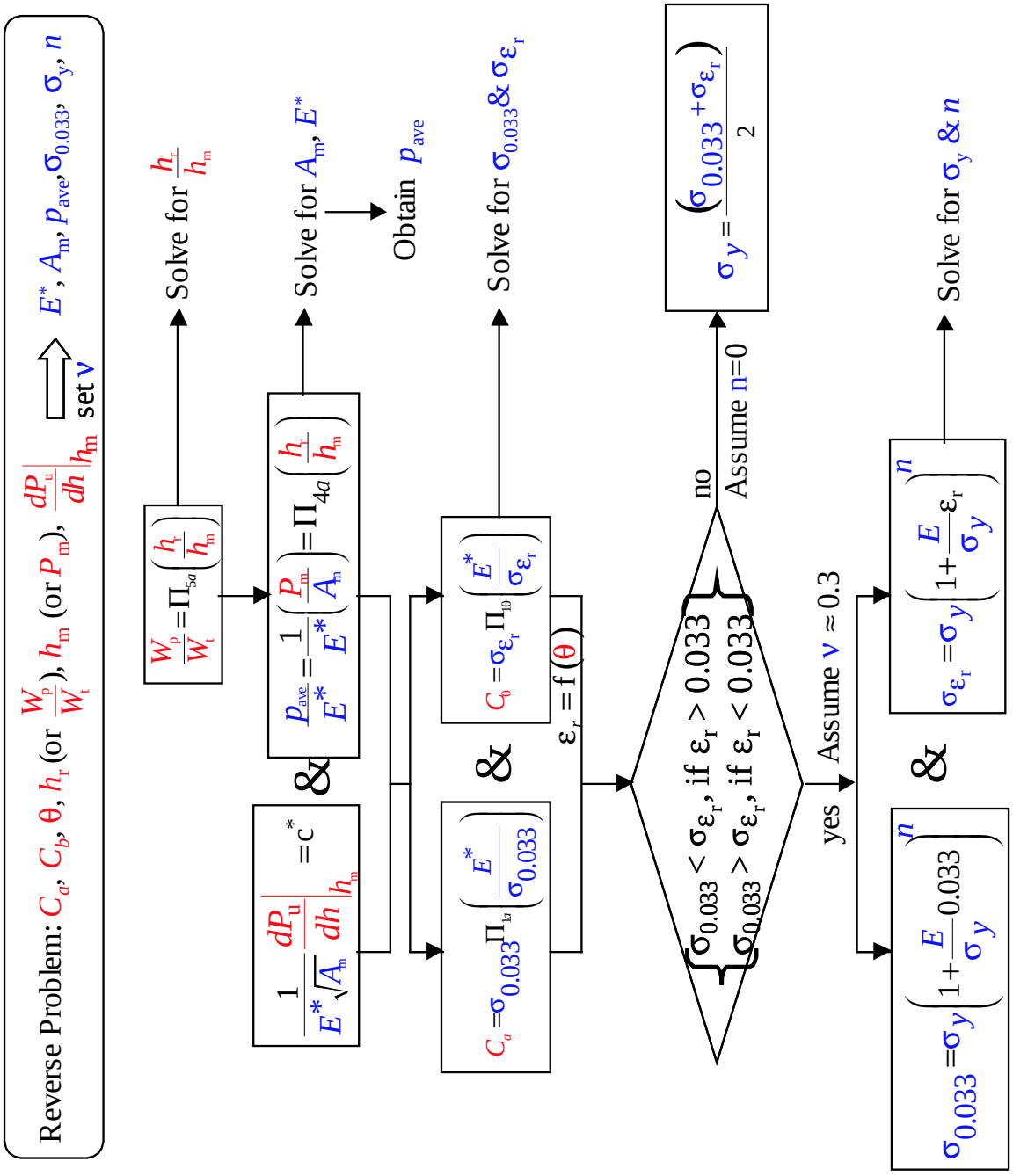

Figure 3-5: Dual Indentation Reverse Analysis Algorithms.

with the single indentation results. In the reverse analyses, each case comprises one set of Berkovich indentation parameters shown in Table 3.2(a) and an average loading curvature C_{b} shown in Table 3.2(b) for the 60° cone equivalent 3-sided pyramid indentation.

According to the flow chart shown in Fig. 3-5, the predictions of E^* and $\sigma_{0.033}$ by the dual indentation algorithm should yield the similar accuracy to those by the single indentation algorithm.

From Table 3.3(a) and (b), it is clear that the proposed reverse algorithms yield accurate estimates of $\sigma_{0.033}$, $\sigma_{0.057}$ and E^*, and give reasonable estimates of σ_y (especially after taking an average from the six indentation results), which agree well with experimental uniaxial compression data. It is noted that changing the definition of σ_y to 0.1% or 0.2% (instead of 0%) offset strain would not affect the main conclusions. According to the flow chart shown in Fig. 3-5, the improvement of the dual indentation algorithm over the single indentation algorithm reflects upon yield strength (and consequently strain hardening exponent) estimation, as clearly illustrated by comparing the first and last column pairs in Table 3.3(a) and (b). This improved calculation of plastic properties is likely due to the fact that the second indenter geometry results in more accurate estimations of the second representative stress $\sigma_{0.057}$ at 5.7% plastic strain in addition to the representative stress $\sigma_{0.033}$ at 3.3% plastic strain.

Table 3.3: Dual Indentation Reverse analysis on (a) Al 6061-T651 and (b) Al 7075-T651 (assume $\nu = 0.3$).

	Single		Dual (using B_{ave})							
	σ_y (MPa)	%err σ_y^a	E^* (GPa)	%err E^*	$\sigma_{0.033}$ (MPa)	%err $\sigma_{0.033}$	$\sigma_{0.057}$ (MPa)	%err $\sigma_{0.057}$	σ_y (MPa)	%err σ_y
(a) Al 6061-T651										
Test A1	333.1	17.3%	67.6	-3.7%	334.5	-1.0%	353.9	0.7%	261.7	-7.9%
Test A2	349.4	3.4%	66.1	-5.8%	349.4	3.4%	355.3	1.1%	322.7	13.6%
Test A3	332.8	17.2%	66.5	-5.3%	332.8	-1.5%	355.0	1.0%	246.5	-13.2%
Test A4	171.0	-39.8%	75.0	6.8%	322.9	-4.5%	348.0	-1.0%	225.2	-20.7%
Test A5	128.0	-54.9%	77.8	10.8%	315.9	-6.5%	346.0	-1.6%	204.4	-28.0%
Test A6	278.5	-1.9%	67.9	-3.4%	337.4	-0.2%	353.7	0.6%	272.9	-3.9%
Ave	265.5		70.1		332.1		352.0		255.6	
Uniaxial Exp	284		70.2		338		351.6		284	
$STDEV^b$	87.7		4.5		12.2		3.6		47.1	
$\frac{STDEV}{X_{exp}}$	30.9%		6.5%		3.6%	1.0%		16.6%		
(a) Al 7075-T651										
Test A1	320.2	-36.0%	79.5	0.5%	537.6	-12.9%	585.2	-10.5%	380.4	-12.3%
Test A2	314.6	-37.1%	81.5	-2.6%	566.9	-8.2%	581.9	-11.0%	511.1	-26.7%
Test A3	332.1	-33.6%	77.2	0.8%	557.6	-9.7%	589.4	-9.8%	447.8	-9.1%
Test A4	289.7	-42.1%	79.7	2.8%	536.8	-13.1%	584.9	-10.5%	376.7	2.4%
Test A5	316.0	-36.8%	78.0	4.4%	542.5	-12.1%	587.8	-10.1%	390.1	8.0%
Test A6	279.7	-44.1%	80.0	4.2%	545.4	-11.7%	584.5	-10.6%	410.3	23.8%
Ave	308.7		79.3		547.8		585.6		419.4	
Uniaxial Exp	500		73.4		617.5		653.6		500	
$STDEV^b$	192.14		6.1		70.6		68.0		93.5	
$\frac{STDEV}{X_{exp}}$	38.4%		8.3%		11.4%	10.4%		18.7%		

[a] All errors were computed as $\frac{X_{\text{revese analysis}} - \overline{X}_{\text{exp}}}{\overline{X}_{\text{exp}}}$, where X represents a variable.

[b] $STDEV = \sqrt{\frac{1}{N}\sum_{i=1}^{N}(X_{\text{reverse analysis}} - \overline{X}_{\text{exp}})^2}$, where X represents a variable.

3.4 Uniqueness of the Dual-Indentation Forward and Reverse Analysis

3.4.1 Uniqueness of the Forward Analysis

In order to verify the proposed forward algorithms, computational results from the 76 sets of elasto-plastic parameters were taken as input to predict the entire $P-h$ responses of $\theta = 70.3^{\text{o}}$ and the loading curvature for $\theta = 60^{\text{o}}$. Each of the forward analyses resulted in a single set of output $\left(C_{\text{a}}, \frac{h_{\text{r}}}{h_{\text{m}}}, \frac{\text{d}P}{\text{d}h}\big|_{h_{\text{m}}} \text{ and } C_{\text{b}}\right)$, which agrees well with the FEM-predicted $P-h$ response.

3.4.2 Uniqueness of the Reverse Analysis

In order to verify the proposed reverse analysis algorithms, the 76 cases of the forward analysis (output) results were used as input to verify the uniqueness of the reverse analysis algorithms. All 76 cases resulted in a single, accurate re-construction of the initial elasto-plastic parameters. For the single-indentation reverse algorithm in Section 2.4.1, two cases out of the same group of 76 cases resulted in no solution. The improvement over our previously proposed reverse algorithm [1] came from the fact that the dimensionless function $\Pi_{2\text{a}}$ or $\Pi_{3\text{a}}$, which is not monotonic in n when $\frac{E^*}{\sigma_{0.033}} < 50$ for $\Pi_{2\text{a}}$ or $\frac{\sigma_{0.033}}{E^*} < 0.005$ for $\Pi_{3\text{a}}$, is no longer used in the present reverse algorithm. Within the range of our current study, the dual indentation algorithm resolves the uniqueness problem.

Cheng and Cheng [40] discussed the non-uniqueness issues by showing that multiple stress-strain curves could result in a visually similar loading and unloading curve. However, such cases were based on the FEM results of 68° apex angle. Following an approach similar to that in Cheng and Cheng [40] for our FEM results of 70.3° apex angle, Fig. 3-6 shows a set of three visually similar FEM indentation responses of steel with different yield strength and strain hardening exponent. It is worth noting two points here. First, when these three visually similar FEM indentation responses (small but with finite differences in the $P-h$ characteristics) were input into the single indenter reverse algorithm (see Fig. 2-12), three unique sets of mechanical properties can be obtained, although the accuracy is

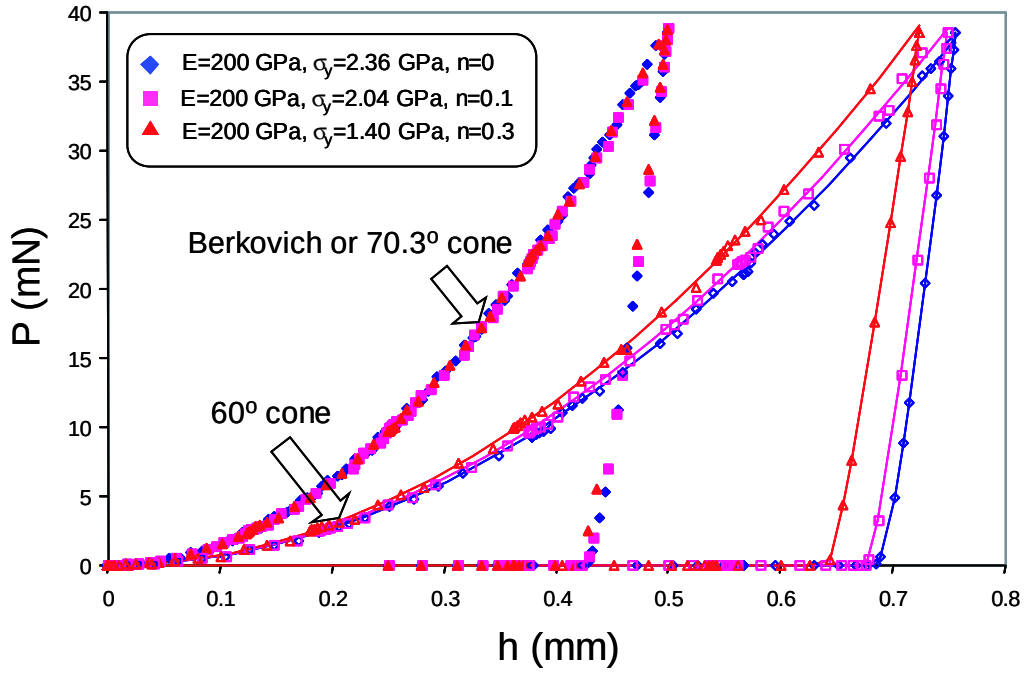

Figure 3-6: An example of the uniqueness problem solved by the second indenter.

sensitive to small experimental scatters. Second, using a second indenter for analysis helps in reducing the non-uniqueness problem and improving the accuracy, as clearly shown by the different loading curvatures of the second indentation response from 60º cone tip. The dual indentation reverse algorithm shown in Fig. 3-5 is thus capable of accurately performing the reverse analysis on these three curves.

3.5 Sensitivity of the Dual Indentation Analysis

3.5.1 Sensitivity of the Forward Analysis

Similar to the sensitivity analysis performed in Section 2.4.2, a ±5% change in any one input parameter (i.e., E^*, σ_y or n) would lead to variations of less than ±7.6% in the predicted results $\left(C_a, \frac{h_r}{h_m}, \frac{dP}{dh}|_{h_m} \text{ and } C_b\right)$. The rather small variability confirms the robustness of the forward algorithm.

Table 3.4: Normalized Standard Deviations in Properties Estimation using Dual Indentation Reverse Algorithm

Δ_{output} in \ Δ_{input} in		$\pm 2\%$ C_{a}	$\pm 2\%$ $\frac{\mathrm{d}P}{\mathrm{d}h}\big\vert_{h_{\text{m}}}$	$\pm 1\%$ $\frac{W_{\text{p}}}{W_{\text{t}}}$
Normalized STDEV in estimated properties[a]	E^*	1	1	1
	$\sigma_{0.033}$	1	1	1
	σ_{y} $(n \leq 0.1)$	1	0.45	0.20
	σ_{y} $(n > 0.1)$	0.83	0.34	0.18
	p_{ave}	1	1	0.53

[a] The normalized STDEV is calculated from $\frac{STDEV_{\text{dual}}}{STDEV_{\text{single}}}$, where STDEV $= \sqrt{\frac{1}{N}\sum_{i=1}^{N}(X_{\text{varied}} - X_{\text{reference}})^2}$ and X_{varied} represents a percentage deviation from $X_{\text{reference}}$.

3.5.2 Sensitivity of the Reverse Analysis

The sensitivity of the estimated mechanical properties to variations in the input parameters obtained from dual $P-h$ curves was investigated for the 76 cases examined in this study. For each of these cases, the sensitivity of the estimated elasto-plastic properties to variations in the four $P-h$ curve parameters$-C_{\text{a}}$, $\frac{\mathrm{d}P}{\mathrm{d}h}\big\vert_{h_{\text{m}}}$, $\frac{W_{\text{p}}}{W_{\text{t}}}$ and $C_{\text{b}}-$about their respective reference values (as estimated from the forward analysis) was analyzed. The variations of $\pm 1\%$, $\pm 2\%$, $\pm 3\%$ and $\pm 4\%$ in C_{a}, $\frac{\mathrm{d}P}{\mathrm{d}h}\big\vert_{h_{\text{m}}}$, $\frac{W_{\text{p}}}{W_{\text{t}}}$ and C_{b} about their forward prediction values were fed into the reverse algorithm. The outputs from reverse algorithm were statistically analyzed in the similar fashion as described in Section 2.4.2. As shown in Figs. 2-13 and 3-5, the improvement of the dual reverse algorithms reflects in the estimation of yield's strength. Hence, similar to Fig. 2-17, Fig. 3-7(a) and 3-7(b) show the sensitivity chart for $\sigma_{0.057}$ and σ_{y}, respectively. Superimposed on Fig. 3-7(b) is the result from single indentation reverse analysis (see Fig. 2-17) for comparison. From Fig. 3-7(b), the average variations and the 99% confidence interval error bar in $\frac{\mathrm{d}P}{\mathrm{d}h}\big\vert_{h_{\text{m}}}$ and $\frac{W_{\text{p}}}{W_{\text{t}}}$ are significantly reduced.

Furthermore, the outputs from reverse algorithm were statistically compared with the original values of elasto-plastic properties. The standard deviations (STDEV) were calculated for each $\pm x\%$ variation, thus sampled over $2 \times 76 = 152$ data points, and com-

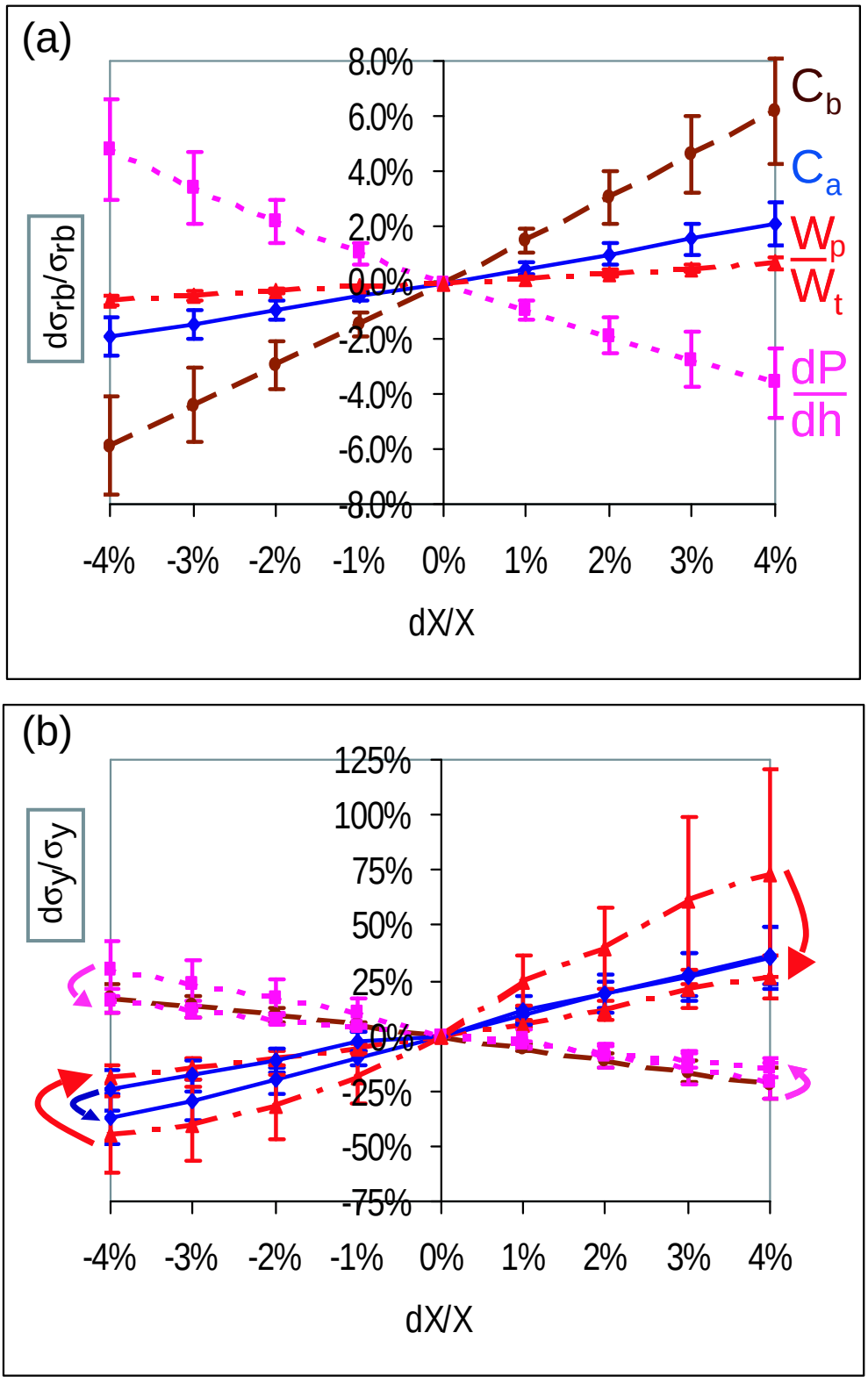

Figure 3-7: Sensitivity charts for reverse analysis showing the average variations in (a) $\sigma_{0.057}$ and (b) σ_{y} due to $\pm 4\%$ perturbation in C_{a} (solid line), $\frac{\mathrm{d}P}{\mathrm{d}h}\big|_{h_{\mathrm{m}}}$ (dotted line), $\frac{W_{\mathrm{P}}}{W_{\mathrm{t}}}$ (dash-dotted line) and C_{b} (long-dash line), with the error bar indicating 99% confidence interval.

pared with that of single indentation. Table 3.4 lists the specific values of STDEV of the dual indentation normalized with that of the single indentation at $\pm 2\%$ C_{a}, $\pm 2\%$ $\frac{\mathrm{d}P}{\mathrm{d}h}\big|_{h_{\mathrm{m}}}$ and $\pm 1\% \frac{W_{\mathrm{p}}}{W_{\mathrm{t}}}$, typically found in the experimental scattering. Other variations in the $P-h$ curve parameters follow the similar trend shown in Table 3.4. Significant improvement of yield strength (for a two-parameter power law plastic constitutive law) was achieved due to the second plasticity parameter, $\sigma_{0.057}$, which can be predicted as robustly as $\sigma_{0.033}$. For instance, within $\pm 1\%$ experimental error in $\frac{W_{\mathrm{p}}}{W_{\mathrm{t}}}$, the average error in the estimated yield strength was reduced by 80% using the dual indentation algorithm.

3.6 Extension to Multiple-Indentation Analysis

To further improve the accuracy and reduce the sensitivity of the reverse algorithm, multiple indenter geometries may be used. This multiple indentation analysis requires a complete indentation curve of Vickers/Berkovich indenter and a loading indentation curve of other tip geometries, $\theta \in [50^{\mathrm{o}}, 80^{\mathrm{o}}]$. A set of the multiple indentation reverse algorithms is shown in Fig. 3-8. It is similar to that of dual indentation except at the last step where yield strength and strain hardening exponent are to be determined. For each indenter geometry (θ), a pair of representative strain and stress can be determined using generalized dimensionless function $\Pi_{1\theta}$ and $\varepsilon_{\mathrm{r}\theta}$ in Eqs. (A.10), (3.6) and (3.7) respectively. By statistically fitting (least square error) these stress/strain values with the power hardening equation (Eq. 2.5), σ_{y} and n can be determined. On the other hand, the dual indentation algorithms shown in Fig. 3-4 can be easily extended to different tip geometries $\theta \in [50^{\mathrm{o}}, 80^{\mathrm{o}}]$. Given a set of elasto-plastic properties, one can predict a complete indentation response for Vickers/Berkovich indenter and a loading indentation response for arbitrary indenter tip geometries.

3.7 Conclusions

In this chapter [60], dimensional analyses and large deformation finite element studies were performed to address the uniqueness problem in the extraction of material properties from

Figure 3-8: Multiple Indentation Reverse Analysis Algorithms.

instrumented sharp indentation and to improve the accuracy and sensitivity of the algorithms used to extract such properties. The key results of this investigation can be summarized as follows.

1. Using dimensional analysis, additional universal, dimensionless functions were constructed to correlate elasto-plastic properties of materials with indentation response for 50°, 60° and 80° cones (or their equivalent 3-sided pyramids). Choosing a pair of Berkovich (or Vickers) and 60° cone (or its equivalent 3-sided pyramid), forward and reverse analysis algorithms were established based on the identified dimensionless functions. These algorithms allow for the calculation of indentation response for a given set of properties, and also for extraction of some plastic properties from a dual set of indentation data, thus obviating the need for large-scale finite element computations after each indentation test.

2. Assuming large deformation FEM simulations and an isotropic power law elasto-plastic constitutive description within the specified range of material parameters, the present reverse algorithms using dual indenters (Berkovich/Vickers and cone of 60° apex angle) were able to predict a single set of values for E^*, $\sigma_{\rm y}$ and n. Furthermore, the full stress-strain response can be estimated from the power law assumption.

3. The accuracy of the dual indentation forward/reverse algorithms were verified in two aluminum alloys (6061-T651 and 7075-T651) with an improvement over the single indentation forward/forward algorithms.

4. The proposed dual indentation forward algorithms work well and robustly with similar sensitivity to the single indentation forward algorithms; a $\pm 5\%$ error in any input parameter results in less than $\pm 7.6\%$ in the predicted values of $C_{\rm a}$, $\frac{h_{\rm r}}{h_{\rm m}}$, $\frac{{\rm d}P}{{\rm d}h}\big|_{h_{\rm m}}$ or $C_{\rm b}$.

5. The proposed dual indentation reverse algorithms were found to predict E^*, $\sigma_{0.033}$ and $\sigma_{0.057}$ quite well, and $\sigma_{\rm y}$ reasonably well for the cases studied. Comprehensive sensitivity analyses show that $\sigma_{\rm y}$ displayed much reduced sensitivity to all $P-h$ parameters due to the second plasticity parameter that can be robustly estimated; whereas, E^*, $\sigma_{0.033}$, $\sigma_{0.057}$ and $p_{\rm ave}$ displayed similar sensitivity to the single indentation algorithms.

6. The extension of forward/reverse algorithms to using multiple indenter geometries,

$50^{o} \leqslant \theta \leqslant 80^{o}$, was proposed with generalized functions of representative strain and indentation loading curvature.

Final remark: An independent computational study using multiple indenters was recently published in Acta Mater [61]. Their findings extended the results from chapter 2 and were consistent with the results presented in this chapter. Nonetheless, this chapter addresses new results which include experimental verification and the uniqueness of the reverse analysis.

Chapter 4

Experimental Assessment of the Representative Stress Estimates from the Instrumented Sharp Indentation

In this chapter, experimental assessment of the representative stresses $\sigma_{0.033}$ and $\sigma_{0.057}$ estimated from single [22, 39] and dual [59] indenters algorithms are critically examined, by analyzing the $P-h$ responses of two metallic materials subjected to different levels of tensile plastic strains prior to indentation. A highly cold-work pure copper that exhibits elastic-perfectly plastic response and an annealed aluminum 6061-T651 alloy that shows considerable work hardening are chosen for their contrasting plastic behavior. Results show that the single indenter methodology proposed by Dao *et al.* [22, 39] accurately predicts a series of $\sigma_{0.033}$, which are offset by the prior plastic strains. In turn, it is shown that the full stress-strain curves can be constructed by connecting the $\sigma_{0.033}$ data. Further, by indenting the same set of strained specimens using a three-sided pyramid tip that is equivalent to a 60^{o} cone indenter, and analyzing the results with the dual indenter methodology proposed by Chollacoop *et al.* [59], a series of $\sigma_{0.057}$ is similarly obtained.

4.1 Introduction

Depth-sensing instrumented indentation has become a popular technique in the recent past for mechanical property evaluation of materials. Development of instruments that can measure load, P, and depth of penetration, h, with high accuracy (to μN and nm, respectively) and a better understanding of contact mechanics problems through computational modeling are the two main factors responsible for this. In a typical instrumented indentation test, the $P-h$ data are continuously recorded for a complete cycle of loading and unloading and is analyzed [23–25, 27, 30, 32–36]. A key factor that goes into this analysis is the contact area between the indenter and the specimen. At micro- and nano-length scales, the material underneath the indenter piles-up or sinks-in against the faces of the indenter, depending on yield stress to elastic modulus ratio and work hardening behavior of the indented material (see Fig.2-14) Hence, it is difficult to measure the true contact area accurately either by simple geometric arguments or through microscopic observations (the latter especially in nanoindentation). Considerable research has been done to overcome this difficulty and standardized methodologies that circumvent this problem are now available [27, 38, 41, 42, 62] It is now possible to evaluate properties such as the elastic modulus, E, and hardness, H, of a given material routinely and reliably. Despite these advances, robust and relatively straightforward methodologies for extraction of plastic properties such as yield stress, σ_{y}, and the work hardening exponent, n, of metallic materials from the $P-h$ curves are not yet available. It would be highly desirable to be able to extract these properties from indentation data, especially σ_{y}, because they are highly sensitive to the microstructures, history, and dimensions of the specimens, and also technological reasons (e.g., the yield behavior of Cu or Al interconnect lines in integrated circuits is essential for modeling their reliability). Additionally, a method that does not require the measurement of contact imprint is desirable from an industrial stand-point-of-view.

A key aspect in achieving this goal is to understand the strain distribution underneath the sharp indenter, which is assessed through the identification of a characteristic (or representative) strain, ε_{r}. Several different values for ε_{r} were attributed in literature (discussed in Section 4.2). Recently, a characteristic stress at $\varepsilon_{\mathrm{r}} = 3.3\%$ was identified by Dao *et al.* [22, 39], who have conducted large-strain finite element analysis of Vick-

ers/Berkovich indentation on a power-law hardening elastic-plastic solids. On this basis, a methodology to assess properties of materials within the context of single [22, 39] and dual [59] indentations were proposed. Note that Section 2.4.3 clearly demonstrates the link between different values of ε_r, and concludes that the apparent disparity stems from a choice of functional definitions used to relate indentation parameters to mechanical properties, but *not* the discrepancies in data or underlying theoretical assumption.

The objective of this chapter is to provide critical experimental assessment of the concept of the characteristic stress. For this purpose, indentation experiments were conducted on two metallic materials with distinct mechanical response: a highly cold-worked Cu that exhibits elastic-perfectly plastic behavior and a well annealed Al alloy that strain hardens considerably. The methodologies proposed by Dao *et al.* [22, 39] and Chollacoop *et al.* [59] were employed to ascertain the possibility of constructing the stress-strain curves from indentation data. This chapter is organized in the following manner. First, relevant literature pertaining to the concept of characteristic strain underneath a sharp indenter is briefly reviewed in Section 4.2. A reader should refer to Chapters 2 and 3 for details of the single and dual indenters methodologies. Materials and experimental details are presented in Section 4.3, and the analysis of the results is presented in Section 4.4. This chapter concludes with a brief summary and identification of possible avenues for utilization of the characteristic stress concept.

4.2 Theoretical Background

For ductile metals that are heavily cold-worked, Tabor [23] has shown that the mean pressure or the hardness can be related to the representative yield stress of the material in uniaxial compression, ε_r, by a simple expression

$$H = C\varepsilon_r \tag{4.1}$$

where ε_r is some 'representative' measure of the flow stress of the deformed metal at the tip of the indenter. Tabor's experiments have shown that the factor of proportionality,

known as the constraint factor, C, is in the range of 2.6 to 3.0. Tabor suggested that for annealed metals under spherical indentation, $\sigma_r = \phi[\varepsilon_o + \alpha(a/R)]$, where ε_o is the initial strain in the test sample, $\alpha(a/R)$ is the strain introduced by the indentation process in the 'representative region', and α is a numerical factor. For conical or pyramidal indentations, where the hardness does not depend on the size of the indentation due to the principle of geometrical self-similarity, it is not possible to set the scale of an indentation without some external reference. On the basis of his experimental observations, Tabor proposed that the representative strain introduced within the plastically deformed region ε_r is $\sim 8\%$ for the case of a Vickers indentation.

Chaudhri [48], by conducting a detailed experimental study of subsurface strain distribution around a Vickers indent in Cu, reported that the maximum strain hardening occurs in a subsurface region adjacent to the tip of indentation. His estimated value of this maximum strain was in the range of 25%-36%, considerably higher than that proposed by Tabor. This strain value correlates well with small-strain finite element analysis conducted by Giannakopolous *et al.* [3] on work-hardening solid. Chaudhri also pointed out that the maximum strain under the indentation might depend on the strain hardening characteristics of the material. While a high value of $\sim 30\%$ appears reasonable for the maximum strain, validity of its use as representative strain remains questionable.

Recent works by Dao *et al.* [22, 39], who have extended the concept developed in [3, 4, 41] by employing a large-strain finite element analysis in the context of single [22, 39] and dual [59] indentations, demonstrate that the representative strains are $\sim 3.3\%$ and 5.7%, respectively. On the basis of this work, explicit closed-form dimensionless functions are constructed, which are in turn utilized to develop forward and reverse analysis algorithms. While the forward algorithm predicts the indentation response (i.e the $P - h$ curve) with the materials' elasto-plastic properties as input parameters, the reverse algorithm predicts materials' elasto-plastic properties from the indentation response.

From Section 2.4.2, error sensitivity analysis shows that in the single indenter reverse algorithms, the reduced Young's modulus, E^*, and a representative stress at 3.3% plastic strain, $\sigma_{0.033}$, were accurately predicted with some sensitivity to experimental scattering typical seen in instrumented indentation. Provided that the assumption of power law

hardening adequately described the full uniaxial stress-strain response, the yield strength (σ_y) and strain hardening exponent (n) could be predicted but suffered a strong sensitivity to small variation in the indentation response. In the dual indenters reverse algorithms as discussed in Section 3.5.2, the representative stress at 5.7% plastic strain, $\sigma_{0.057}$, was also accurately predicted, and the estimates for yield strength were shown to be less sensitive to variation in the indentation response.

However, a critical assessment of the aforementioned methodologies has not been performed hitherto, which is the objective of this chapter. For this purpose, two different materials, one that work hardens whereas the other exhibits elastic-perfectly plastic behavior, are selected. These materials were subjected to different levels of plastic strains prior to indentation. The idea behind this is that the reverse algorithms should predict stresses that correspond to 3.3% plus the prior plastic strains, enabling the construction of the entire stress-strain curves which can then be compared to the uniaxial stress-strain curves to assess the accuracy of the predictions.

4.3 Experiments

Two materials were utilized for experimental investigation: a highly cold-worked pure copper and aluminum 6061-T651 alloy, both in the form of 4.76 mm (3/16 in) thick sheet. Four dog-bone specimens, with 50.8 mm (2 in) gage length, 9.53 mm (3/8 in) gage width and 38.1 mm (1.5 in) grip length, were machined from each sheet. The aluminum specimens were fully annealed in atmosphere at 415 ^{o}C for 2.5 hours (O temper) to obtain the highest hardening. Typical uniaxial tensile tests were conducted on a screw-driven universal testing machine at a cross-head speed of 1.27 mm/min (0.05 in/min) The elongation was obtained from an extensometer. Each copper specimen was strained to approximately 1.6%, 4%, 7.3% and 10% engineering strain before unloading and thus labeled Cu1, Cu2, Cu3 and Cu4, respectively. On the other hand, each aluminum specimen was strained to approximately 0.8%, 3%, 5% and 7% engineering strain before unloading and thus labeled Al1, Al2, Al3 and Al4, respectively. These strain values used in both materials were chosen so that each specimen was plastically deformed before unloading in the incremental manner.

Table 4.1: Averaged mechanical property determined from experimental tensile test.

Material	E (GPa)	ν^a	E^* (GPa)^b	σ_y (MPa)^c	n^d	$\sigma_{0.033}$ (MPa)	$\sigma_{0.057}$ (MPa)
Cu	112.76	0.3	111.42	238	0.029	258	262
Al	65.95	0.33	69.37	25	0.295	94	113

[a] From literature value [54]
[b] Calculated from Eq. (2.8) using $E_i = 1100$ GPa and $\nu_i = 0.07$ for the diamond indenter.
[c] Estimated at 0% offset strain.
[d] Estimated from power law fit.

Indentation specimens were machined (approximately 10 mm long) from the gage section of each strained specimen (Cu1, Cu2, Cu3, Cu4, Al1, Al2, Al3 and Al4) and from the grip section of Cu1 and Al1 (labeled Cu1gs and Al1gs, respectively). The Cu1gs and Al1gs specimens were polished deeper than other specimens to completely remove any marking from the gripping. All specimens were polished to 1 μm diamond paste. The polished samples were then indented on a commercial nanoindenter (MicroMaterials, Wrexham, UK) with a Berkovich and a 60^o cone equivalent three-sided pyramid diamond tips at a loading and unloading of 0.1 N/s. To ensure that each indent was independent of its neighbors, the spacing between the consecutive indents was at least ten times the approximate indentation radius. Limited by the indenter specimen size and the maximum depth allowed in the nanoindenter, the copper and aluminum specimens were indented with the maximum load of 12 and 4 N, respectively under the Berkovich tip, with 1 mm spacing between each indent. On the other hand, the copper and aluminum specimens were indented with the maximum load of 4 and 2 N., respectively under the 60^o cone equivalent three-sided pyramid tip, with 1 mm spacing between each indent. Please note that the maximum load was estimated from the forward algorithms [22, 39, 59]. For all indentation specimens, at least six tests were conducted to ensure the repeatability.

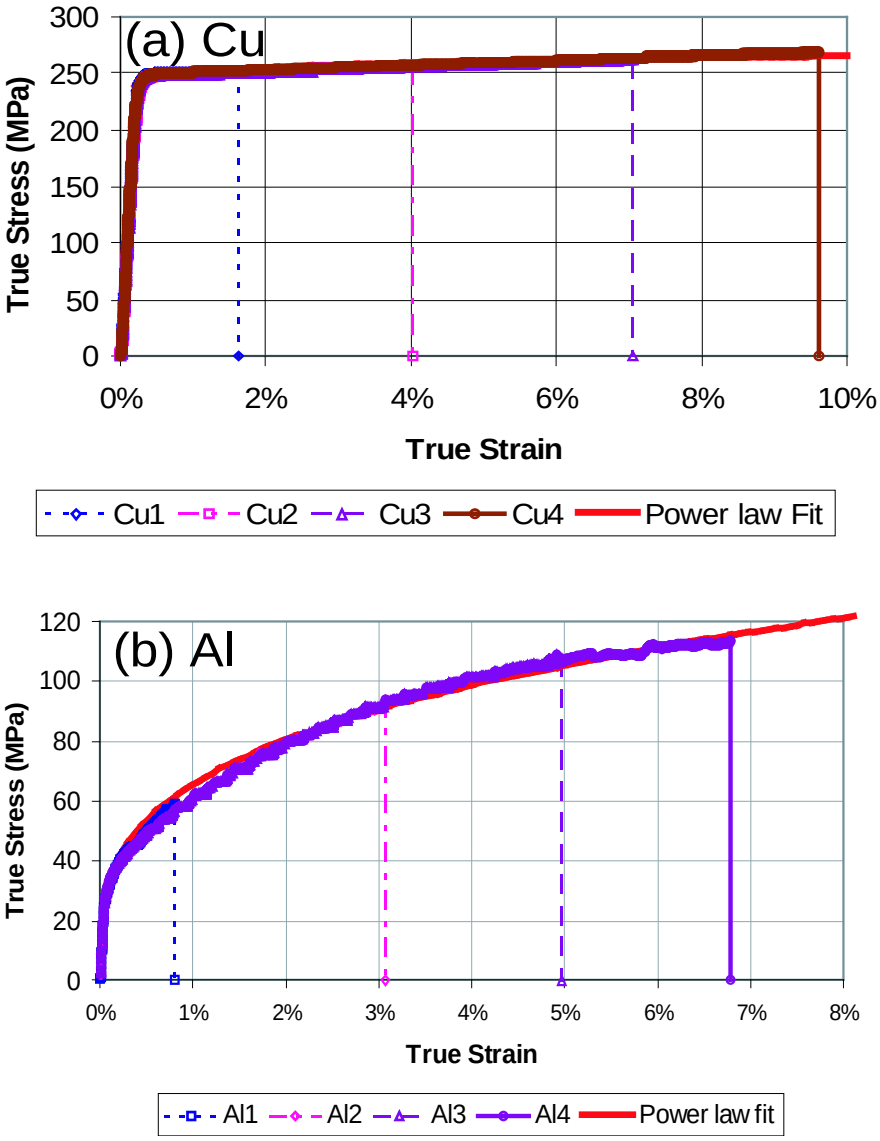

Figure 4-1: Experimental uniaxial tension true stress-true strain responses of (a) copper and (b) aluminum samples with the best power law fit and the pre-strain value projected down on strain axis.

Table 4.2: Maximum true stress and true strain from the tensile test of each strained specimen prior to indentation.

Sample	Cu1	Cu2	Cu3	Cu4	Al1	Al2	Al3	Al4
σ (MPa)	252.15	256.56	261.97	268.33	59.09	94.08	109.30	120.85
$\varepsilon_{\text{pre strain}}$	1.63%	4.01%	7.05%	9.61%	0.81%	3.07%	4.97%	6.79%
$\sigma_{0.033}$ (MPa)	261	264	266	268	101	118	129	138
$\sigma_{0.057}$ (MPa)	263	266	268	269	118	131	140	148

4.4 Results and Discussions

Load-displacement data for both materials were converted to true stress-true strain data, as shown in Fig. 4-1. It was clear that all specimens of each material were repeatable and each specimen was pulled to plastic deformation region. For each material, the Young's modulus was measured from the initial elastic region, and the power law hardening Eq. (2.5) was fitted to the plastic region, as shown in Table 4.1. For comparison with the results from reverse algorithms, the reduced Young's modulus was calculated using Eq. (2.8), and and $\sigma_{0.033}$ and $\sigma_{0.057}$ were estimated from Fig. 4-1. In addition, Table 4.2 lists the values of true stress and true strain each specimen was pulled to. Note that this strain was used to offset the predicted representative stress when compared to the unstrained sample, whereas the corresponding stress was taken as the new yield strength due to work hardening.

For each material and indenter tip, the six indentation curves were statistically analyzed by calculating the average and standard deviation in the incremental range of 0.5 μm and 0.2 μm for loading and unloading sections, respectively. Fig. 4-2(a) and Fig. 4-2(b) show the average curve with the error bar indicating 99% confidence interval from six tests under both indenter tips for the copper and aluminum specimens, respectively. Both sets of data were repeatable as measured by a small error bar of 99% confidence interval. From [22, 39, 59], the loading curvature of the indentation response was rigorously shown to be depending on the reduced Young's modulus and the representative stress only. Thus, the low strain hardening observed in copper specimens predicted the similar values

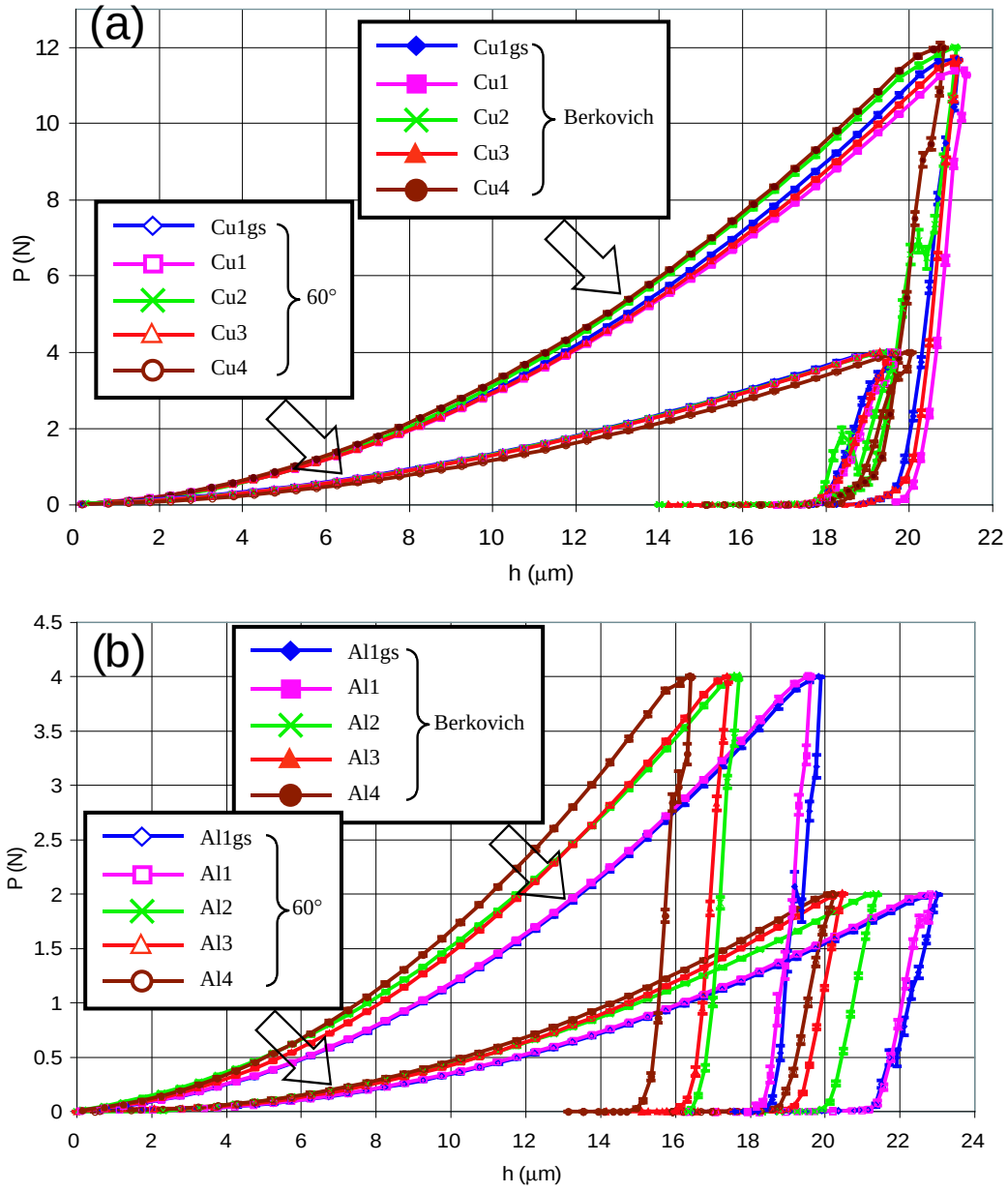

Figure 4-2: Experimental indentation responses (each illustrated by the average with the error bar of 99% confidence interval from 6 tests) under both Berkovich and 60^o cone equivalent three-sided pyramid tips for (a) copper and (b) aluminum specimens.

of representative stress and thus similar indentation curves, as shown in Fig. 4-2(a). On the other hand, the high strain hardening observed in aluminum specimens predicted the increasing values of representative stress and thus stiffer indentation curves with increasing pre-strain values, as shown in Fig. 4-2(b).

The individual indentation responses under both tips for copper and aluminum samples, as representatively shown in Fig. 4-2 were subjected to the single and dual indenter reverse algorithms detailed in [22, 39, 59]. The predictions for reduced Young's modulus, $\sigma_{0.033}$ and $\sigma_{0.057}$ were shown in Figs. 4-3(a), (b) and (c), respectively. It was clear that the predictions from the reverse algorithms well matched the experimental values from the tensile tests. Note that a lesser scattering in $\sigma_{0.057}$ when compared to $\sigma_{0.033}$ may have to do with tip blunting effect because the Berkovich tip has been extensively used whereas the 60^o cone equivalent three-sided pyramid tip is customized and much less used prior to the experiments conducted here.

By superimposing a series of predicted $\sigma_{0.033}$ and $\sigma_{0.057}$ from each specimen onto the average experimental tension stress-strain curves with the power-law fit, Figs. 4-4(a) and 4-4(b) clearly show that the uniaxial tension results were well bounded by the predictions from the reverse algorithms.

4.5 Conclusions

Experiments were conducted to critically assess the representative stress concept, proposed by Dao *et al.* [22, 39] and Chollacoop *et al.* for single and dual indenters algorithm, respectively. Two materials of contrasting plastic behavior (very low strain-hardening pure copper and very high strain-hardening annealed aluminum alloy) were plastically strained prior to indentations under both Berkovich and 60^o cone equivalent three-sided pyramid tips. A series of $\sigma_{0.033}$ were predicted from single indenter reverse algorithms, showing clearly the good agreement with uniaxial tensile stress-strain curve. Better agreement was achieved for a series of $\sigma_{0.057}$ for dual indenters algorithms possibly due to a more perfect tip. This representative stress concept allows the possibility to construct the entire stress-strain curves, with better accuracy and less sensitivity, from multiple indentations of one

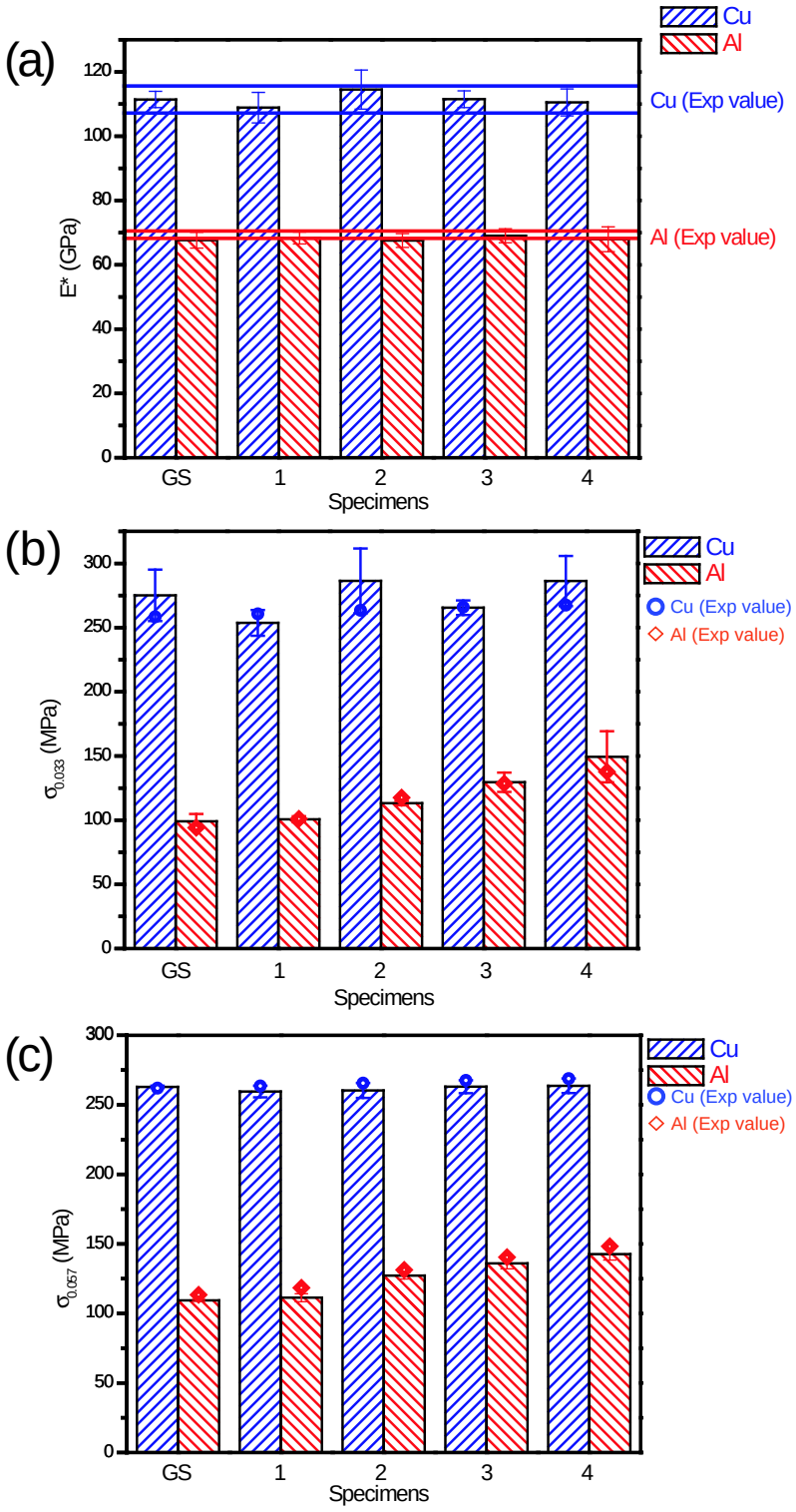

Figure 4-3: The prediction of (a) reduced Young's modulus (the experimental values from uniaxial tensile test span over ± 1 standard deviation), (b) $\sigma_{0.033}$ and (c) $\sigma_{0.057}$ of copper and aluminum specimens from the single and dual indenters reverse algorithms [22, 39, 59] (each illustrated by the average with the error bar indicating the standard deviation, along with the experimental values from uniaxial tensile test).

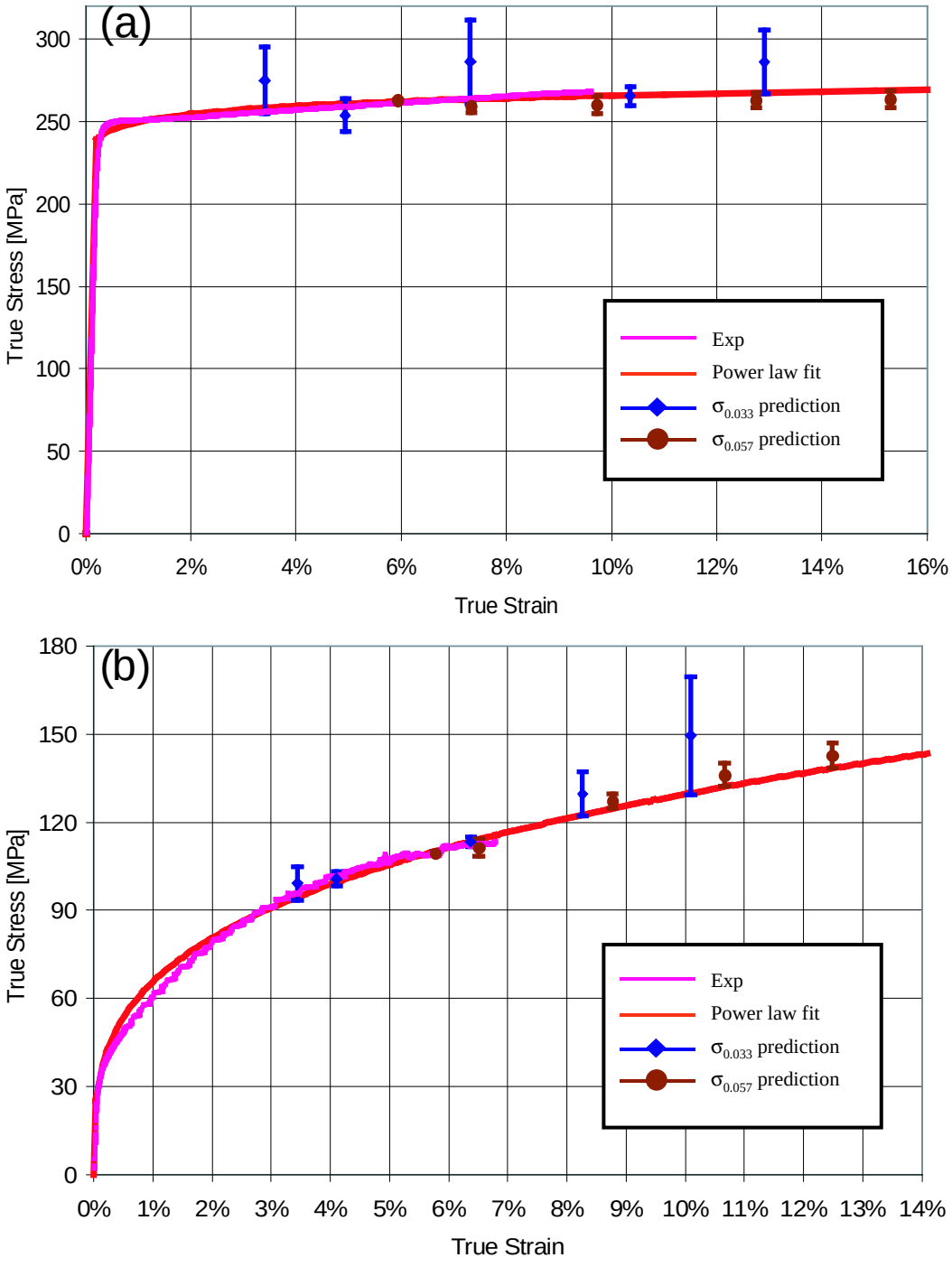

Figure 4-4: Experimental uniaxial tension true stress-true strain responses of (a) copper and (b) aluminum samples with the best power law fit and reverse algorithms prediction of $\sigma_{0.033}$ and $\sigma_{0.057}$. Each prediction illustrated by the average with the error bar indicating the standard deviation.

or more indenter tips, provided that each indentation is performed at different levels of previously plastic-strained specimens.

Chapter 5

Computational Modeling of Nanocrystalline Materials

In this chapter*, the effects of rate sensitivity and grain size upon mechanical properties of nanocrystalline materials are investigated by recourse to the continuum modeling within the context of finite element analysis. Systematic experiments have been performed to investigate the rate-sensitivity of deformation in fully dense nanocrystalline Ni using two different experimental techniques: depth-sensing indentation and tensile testing. Results from both types of tests revealed that the strain-rate sensitivity was a strong function of grain size. Specifically microcrystalline and ultra-fine crystalline pure Ni, with grain size range of > 1 μm and 100-1000 nm, respectively, exhibited essentially rate-independent plastic flow over the range 3×10^{-4} to 3×10^{-1} s^{-1}, whereas nanocrystalline pure Ni with a grain size of approximately 40 nm, exhibited marked rate-sensitivity over the same range. A simple computational model, predicated on the premise that a rate-sensitive grain-boundary affected zone (GBAZ) exists, was shown to explain the observed effect of grain size on the rate-dependent plastic response. The same GBAZ model was further utilized in the parameter study of grain size effect on rate-independent plastic response (i.e., flow stress as a function of grain size at the quasi-static deformation rate). The results predicted inverse Hall-Petch-type relation at the similar grain size range observed in the literature.

*This article is published in *Acta. Mater.*, Vol. 51 (2003), p. 5159, with co-authors: R. Schwaiger, B. Moser, M. Dao and S. Suresh. [16]

5.1 Introduction

Nanocrystalline materials, with grain size typically smaller than 100 nm, are known to possess some attractive properties, such as high yield and fracture strengths [63–65], improved wear resistance [66, 67], and superplasticity at relatively low temperatures [14, 68], compared to their microcrystalline counterparts with grain size typically larger than 1 μm. Recently, there has been growing experimental evidence that nanocrystalline materials also exhibit highly strain-rate sensitive mechanical properties [7, 8]. However, experimental data available to date in the literature on the strain-rate sensitivity of nanocrystalline metals are very limited, and quantitative results are not conclusive.

Lu *et al.* [7] studied the effects of strain rate on the tensile flow and fracture behavior of nanocrystalline electrodeposited Cu specimens with a mean grain size of about 30 nm. The strain to failure was found to increase significantly with increasing strain rate, which is different from the behavior seen in conventional Cu where the fracture strain decreases slightly at higher strain rates. The flow stress was only mildly dependent on strain rate; within the strain rate range of 6×10^{-5} to 1.8×10^{3} s^{-1} the flow stress at 1% plastic strain increased from about 85 to roughly 150 MPa.

Dalla Torre *et al.* [8] studied nanocrystalline electrodeposited Ni with a mean grain size of about 20 nm over a wide range of strain rates. Their results partly contradicted the results of Lu *et al.* [7] in that the ductility decreased with increasing strain rate for strain rates ranging from 5.5×10^{-5} to 5.5×10^{-2} s^{-1}. The tensile strength was observed to be approximately 1500 MPa and essentially constant for strain rates between 7×10^{-5} and 5.5×10^{-2} s^{-1}, but increased significantly for strain rates of 10^{1} to 10^{3} s^{-1} to values as high as 2600 MPa. The same trends shifted to slightly higher strain rates were observed on coarser-grained Ni [8]. Wang *et al.* [13] observed a loading-rate sensitivity in electrodeposited nanocrystalline Ni subjected to tensile and creep tests. Enhanced strain-rate sensitivity at room temperature with decreasing grain size was also found in nanoindentation experiments on nanocrystalline oxides, such as TiO_2 and ZnO [69, 70].

Many of the results available in the literature cannot easily be compared. The different techniques used to produce the materials result in widely different internal struc-

tures and processing-induced artifacts, such as contamination, porosity, and residual stress. These differences render it difficult to identify the mechanisms responsible for differences in mechanical properties. Another common problem is that only a limited amount of material is typically available to conduct experiments, often with sub-sized specimens. Furthermore, experiments at different strain rates generally involve different specimen designs, loading methods, displacement and strain monitoring techniques, and precision of data. Lu *et al.* [7] and Dalla Torre *et al.* [8], for instance, compare results from quasi-static tensile tests with data obtained from high strain rate dynamic loading. Using different instruments, test techniques and loading methods, often requires use of a differently sized specimen [7], which may influence the mechanical response measured [8]. Most theoretical/computational studies, including atomistic simulations [71, 72], and continuum-micromechanics based models (e.g. [73, 74]), focus on yield strength and related deformation mechanisms, but do not describe the rate-dependent mechanical behavior of nanocrystalline materials under realistic load or strain rates.

There is a critical need for examining the strain-rate sensitivity of nanocrystalline metals and alloys through consistent and systematic data obtained over a wide range of strain rates using a single experimental technique in a fully dense, high purity, and well-characterized material. These results should then be confirmed using a different, independent method on the same materials. Indentation is the preferable method, since the tested volume of material is scaleable with respect to the microstructure. In this manner, strain-rate sensitivity of nanocrystalline (nc), ultra-fine crystalline (ufc), and microcrystalline (mc) specimens of the same material can be studied using a single specimen geometry and loading configuration over a wide strain-rate range where the deformed volume of the material in each case samples a sufficient number of grains for extraction of reliable data. The present study investigated electrodeposited nc and ufc Ni, which was fully dense and well characterized. Parallel tensile tests at different loading rates were also performed to verify independently the trend extracted from the indentation experiments. The results from the electrodeposited nc and ufc Ni were compared with conventionally produced mc Ni. In order to provide a rationale for interpreting deformation mechanisms, a simple computational model was proposed. The computational results were consistent with both the indentation and tensile experiments.

Using the proposed model, the parameter study of grain size effect on flow stress in nc-Ni exhibited the inverse Hall-Petch-type relation, where the flow stress decreased with decreasing grain size opposing the conventional Hall-Petch relation [75, 76] typically observed in the microcrystalline counterpart. The predicted critical grain size for the transition from Hall-Petch to inverse Hall-Petch-type relations was consistent with the experimental observation and the atomistic simulation reported the literature [5, 65, 77–88].

5.2 Experimental details

5.2.1 Materials and specimen preparation

Nickel specimens of different grain sizes were investigated. Fully dense, nanocrystalline Ni sheets were procured from Integran Technologies Inc. (Toronto, Canada). They were produced by electrodeposition and were of 99.8% and 99.9% purity and nominal grain sizes of 20 and 200 nm, respectively. The foils had a thickness of about 150 μm. The electrodeposited materials of nominal 20 and 200 nm grain size will henceforth be denoted as nc and ufc Ni, respectively. These foils were ground and polished on one side using SiC paper of 500, 1200, 4000 grain size and diamond suspensions of 6, 3, 1, and 0.25 μm grain size. The thickness of the specimens after the polishing procedure was about 100 μm. For comparison, microcrystalline Ni foils of commercial purity were polished following the same procedure.

The specimens used for indentation testing were rectangular with about 10 mm side length. They were glued onto Al cylinders using a standard cyanoacrylate glue ("superglue"). For tensile tests, sub-sized dog-bone specimens were cut from the Ni foils by electrical discharge machining. The width and length of the specimen gage section were 5 and 20 mm, respectively. The shoulder radius was 6 mm and the shoulder width 2 mm. The specimen thickness was equal to the foil thickness.

5.2.2 Indentation test methods

Two different indenters were used in order to test the electrodeposited Ni foils over a wide range of loads and load or strain rates. This approach also facilitated a comparison of the effects of different indenter designs on the experimental scatter seen for the different grain sizes. The indenters used were: MTS NanoXP system (MTS Systems Corporation, Eden Prairie, MN, USA) for probing the specimens to a depth of 1 μm (maximum load capability: 500 mN, maximum indentation depth: 500 μm), and Micromaterials Microindenter (Micro-Materials Ltd., Wrexham, UK), which is capable of applying loads in the Newton-range, for indenting samples to depths of 3 μm. In all tests, diamond Berkovich tips with a pyramidal tip shape and a tip radius of approximately 150 nm, were used.

The Nanoindenter XP uses a coil-magnet assembly for loading a probe, and measures the displacement into the sample with a capacitance gage. In addition to load and displacement data, the instrument provides continuous measurement of the contact stiffness via a superimposed AC signal during loading [27]. Constant loading rate experiments as well as tests at a constant indentation strain rate [89] can be performed. Details of this instrument can be found elsewhere [27, 90].

In these experiments, the specimens were tested at different constant indentation strain rates. The indentation strain rate ($\dot{\varepsilon}_{\mathrm{ind}}$) is defined as the rate at which the indenter penetrates into the material $\frac{\dot{h}}{h}$, where h is indentation depth. From the hardness definition, $H = \frac{P}{A} = \frac{P}{\mathrm{B}h^2} \rightarrow P = \mathrm{B}h^2H$, where B is a proportionality constant relating the projected area of indentation to its depth squared. The indentation strain rate is then given by

$$\frac{\dot{P}}{P} = \frac{\mathrm{B}(2h\dot{h}H + h^2\dot{H})}{\mathrm{B}h^2H} = 2\frac{\dot{h}}{h} + \frac{\dot{H}}{H} \tag{5.1}$$

With the assumption of constant hardness throughout the indentation depth (no size effect), $\dot{H} \approx 0$ simplifies Eq. (5.1) to

$$\frac{\dot{h}}{h} = \frac{1}{2}\frac{\dot{P}}{P} = \dot{\varepsilon}_{\mathrm{ind}} \tag{5.2}$$

The Nanoindenter XP is then applying the loading rate and adjust the load according to the feedback unit such that the ratio of $\frac{1}{2}\frac{\dot{P}}{P}$ equals to the indentation strain rate $\frac{\dot{h}}{h}$ prescribed by the user.

The specimens were first loaded to a depth of 1 μm, and the maximum load was held constant for 10 s. Then the specimens were unloaded to 20% of the maximum load and the load was held constant for a period of 60 s while the displacement was monitored to determine the displacement rate produced by thermal expansion in the system. Finally, the load was removed completely. The displacement data were corrected assuming a constant drift rate throughout the test. In all experiments, the contact stiffness was recorded continuously during the loading segment. Indentation strain rates of 0.01, 0.025, and 0.1 s^{-1} were applied. For each strain rate 5 and 10 indents were performed for the nc and ufc Ni, respectively.

The Microindenter is a pendulum-based depth-sensing indentation system with the load applied horizontally through a coil-magnet assembly. The tip displacement is measured with a parallel plate capacitor. The machine is mounted in an enclosure held at a constant temperature to minimize thermal drift effects in the displacement sensing system. Experiments at constant loading rates of 3.8, 12.0, 40.5, and 186.1 mN/s were performed. The loading sequence was as follows: the tip was brought into contact with the material and held there at a load of 100 μN for 60 s while the displacement was monitored. The measured displacement rate was attributed to thermal drift in the system and used to correct the displacement data. Subsequently, the specimen was indented at a constant loading rate to a depth of 3 μm. The load was held constant at its maximum value for 10 s. Finally, the samples were unloaded at the respective loading rates. For each foil and load rate, 10 indents were performed

The indentation hardness was extracted from indentation data. For the strain-rate controlled experiments, the hardness was determined continuously throughout the depth of indentation. The results obtained from load-rate controlled indentation were analyzed according to the procedure outlined by Oliver and Pharr [27]. The unloading curves, however, were shifted to the end of the loading segments, in order to compare the hardness at the applied maximum loads. This procedure allows for capturing the influence of load

or strain rate on indentation hardness, since creep effects during the hold segment would partially eliminate hardness changes due to the applied strain or load rate. Although this procedure introduces a certain error as the contact stiffness slightly increases during creep due to the depth increase, the hold segment is required to reduce the effect of creep on the unloading curve, particularly at higher load or strain rates [91]. However, it was found that the error introduced by this procedure was negligible compared to the experimental scatter. The unloading curves were then fitted with a power law for the data points lying between 20% and 80% of the maximum load.

5.2.3 Tensile test methods

The trends extracted from indentation tests were verified by using another independent experimental method, i.e. the tensile test. All tensile tests were performed on a computer-controlled hydraulic testing machine (Instron Dynamight, Instron Corporation, Canton, MA, USA) with a load cell capacity of 1 kN. Position-controlled experiments with three different stroke displacement rates were performed. Strain was measured with an extensometer (10 mm gage length) to a maximum strain of 2.5%. The strain data obtained from the extensometer was used to correct the stroke displacement data for machine compliance by comparing the two stress-strain curves in the elastic regime. Since the samples were strained to fracture (strains $> 2.5\%$), the strain derived from the corrected stroke displacement was used for further analysis.

5.3 Results

The nc Ni investigated in this study has been extensively characterized in an earlier study [92], which revealed a narrow grain size distribution with a mean grain size of approximately 40 nm. Growth twins were found to be prevalent. The grain interior appeared to be clean and devoid of dislocations. The grain boundaries showed no evidence of second phase particles or films. The grain size distribution on the surface of the ufc Ni was not unimodal and a number of grains were significantly larger than the average grain size of 320 nm, which was estimated from quantitative image analysis.

5.3.1 Constant strain-rate indentation experiments

Figures 5-1(a) and (b) show $P-h$ curves obtained from the ufc and nc specimens, respectively. In both cases three different indentation strain rates were applied. The curves obtained from the ufc Ni show considerable scatter, Fig. 5-1(a). Within the experimental scatter, no difference between the different indentation strain rates was observed. The $P-h$ curves given in Fig. 5-1(b) for the nc material, however, show a distinct and experimentally detectable effect of indentation strain rate. With increasing strain rate, a higher indentation force is required in order to impose the same displacement. The loads applied during the experiments on the nc material were considerably larger than those for the ufc material for a given indenter penetration depth (Fig. 5-1).

In Fig. 5-2, the hardness is plotted versus the depth of indentation as determined continuously during indentation for both the ufc and nc specimens. The hardness of the nc Ni is significantly higher than that of the ufc Ni. The scatter in the ufc Ni data is considerably larger than in the data obtained from the nc Ni. Within the scatter a clear strain rate effect on the indentation response of the ufc Ni cannot be inferred. In case of the nc Ni, however, the hardness increases with increasing indentation strain rate. The hardness values of the nc Ni are between 5.8 and 6.4 GPa at maximum indentation depth, whereas the hardness of the ufc Ni is almost a factor of two smaller. The slight hardness decrease of the nc Ni with increasing indentation depth was attributed to the compliance of the experimental setup.

5.3.2 Constant load-rate indentation experiments

The $P-h$ curves of the ufc and nc Ni at constant load rates for larger indentation depths are shown in Fig. 5-3. Four different load rates were applied. The unloading portion of the curves was shifted to the depth achieved at the end of the loading segment. Hardness versus load rate is plotted in Fig. 5-4 at $h = 2800$ nm. In case of the ufc Ni, the hardness is constant, whereas in case of the nc Ni the hardness increased with increasing load rate.

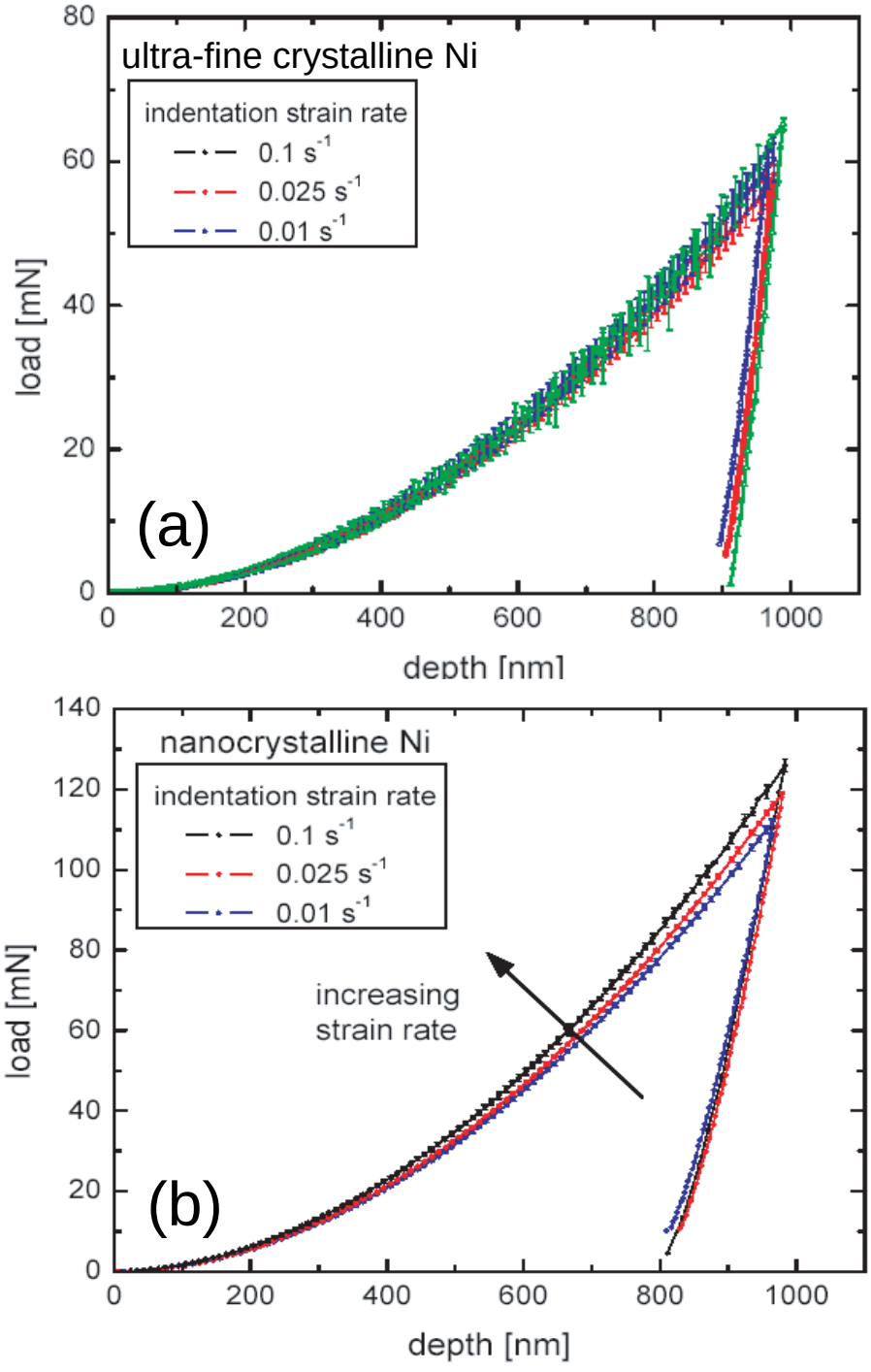

Figure 5-1: Load-displacement ($P-h$) curves of the (a) ufc Ni (320 nm grain size) and (b) nc Ni (40 nm grain size). The average curve including error bars (95% confidence interval) of 10 and 5 curves, respectively, at three different indentation strain rates is shown.

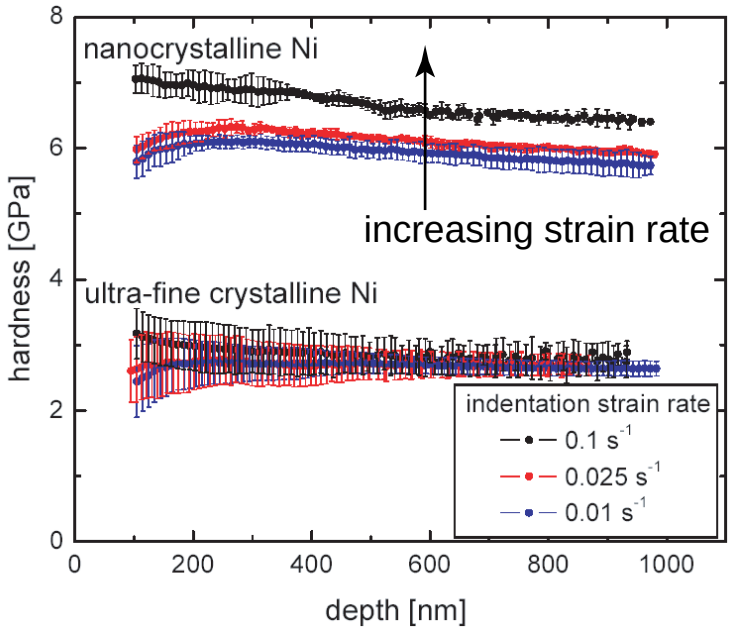

Figure 5-2: Hardness versus indentation depth for nc and ufc Ni. The hardness was determined continuously during indentation for three different indentation strain rates. The average of 10 and 5 indents for ufc and nc Ni, respectively, are shown.

5.3.3 Tensile tests

Stress versus strain calculated from the compliance-corrected stroke displacement for $\dot{\varepsilon} = 3 \times 10^{-1}$ s^{-1} for the different materials tested is shown in Fig. 5-5(a). Yield strength as well as tensile strength (TS) increase with decreasing grain size. For the mc Ni foil only the beginning of the curve is shown, as fracture occurred at about 30% strain. Figure 5-5(b) shows stress-strain curves obtained from the nc Ni deformed at three different strain rates. The flow stress increases with increasing strain rate.

5.4 Discussion

5.4.1 Experimental Trends

In both indentation and tensile tests, a strengthening effect due to grain size reduction was consistently observed. The indentation hardness of nc Ni is almost twice as high as

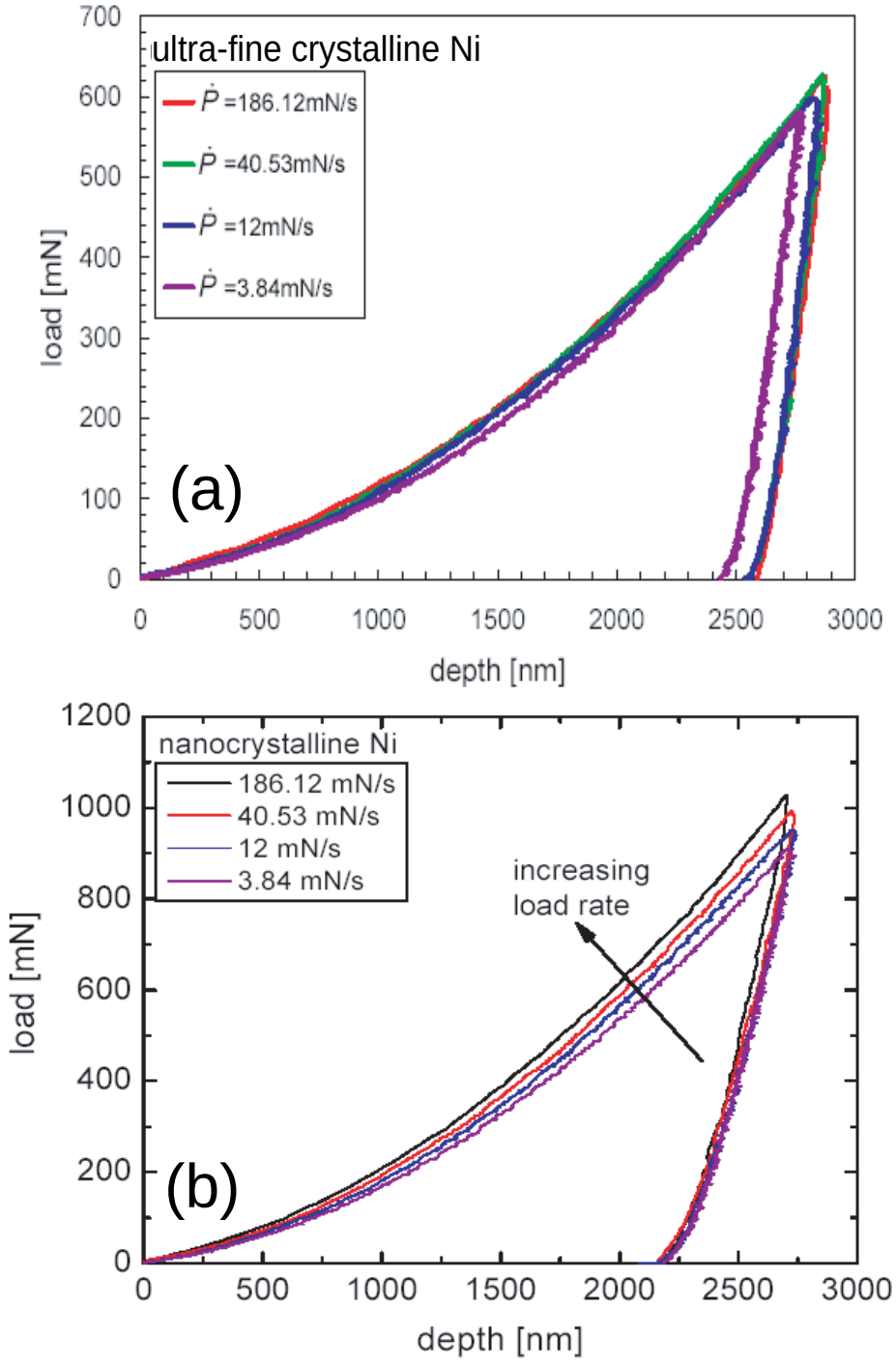

Figure 5-3: Load-displacement ($P-h$) curves of the (a) ufc Ni (320 nm grain size) and (b) nc Ni (40 nm grain size). The average curves of 10 and 5 curves, respectively, at four different load rates are shown.

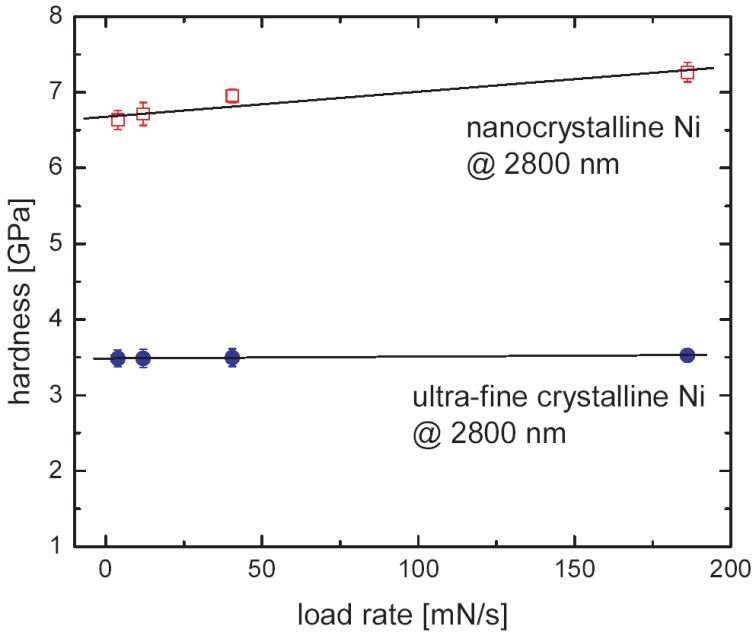

Figure 5-4: Hardness versus load rate for nc and ufc Ni at $h = 2800$ nm. The hardness was determined at the indentation depth at maximum load for four different load rates (3.84, 12.0, 40.53, and 186.12 mN/s). The average of 10 indents for ufc and nc Ni are shown.

the hardness of ufc Ni. In the tensile tests, the TS of the three types of materials tested increased from about 450 MPa for mc (grain size: 10 μm) to about 920 MPa for ufc (grain size: 320 nm) and to more than 1600 MPa for nc Ni (grain size: 40 nm). However, this increase in strength was accompanied by a significant ductility reduction; the strain at TS is reduced from 30% for the mc Ni to only about 2-3% for the nc and the ufc Ni foils. Generally, the strength as well as the hardness values compare well with the values presented by Dalla Torre *et al.* [8]. However, the overall trends observed in the present experiments are different and can be well described by a simple computational model, which is based on recent experimental observations and simulations.

Ex-situ transmission electron microscopy (TEM) studies of nc metals have revealed that grains are essentially dislocation-free [92, 93]. The authors argue that the grain boundaries act as dislocation sinks due to image forces. However, during in-situ straining experiments in the TEM dislocation activity in the grain interior has generally been observed for grain sizes larger than 100 nm [94–97].

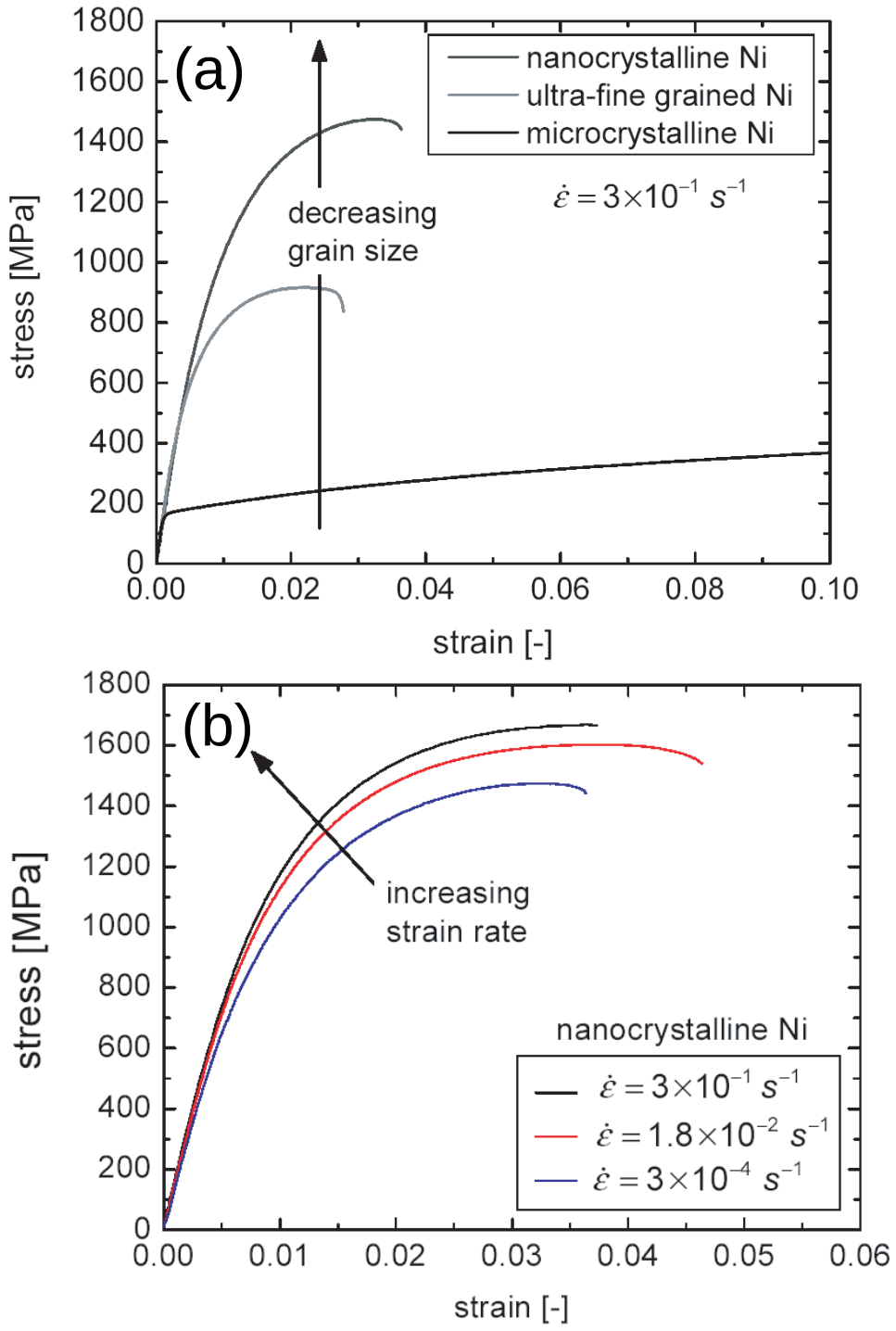

Figure 5-5: Stress versus strain (a) for nc, ufc, and mc Ni at a strain rate $\dot{\varepsilon} = 3\times10^{-1}$ s^{-1} and (b) for nc Ni at three different strain rates.

Kumar *et al.* [92] performed TEM on the same material investigated in the present study and found that the grain boundaries were atomically sharp and that no amorphous phase was present at the grain-boundary regions, as suggested by Keblinski *et al.* [98]. High-resolution TEM studies revealed that in electrodeposited nc materials, crystallinity is maintained up to the grain boundary [92]. These studies also included in-situ TEM on nc Ni where dislocation activity within grain boundaries was observed at grain sizes as low as 30 nm.

5.4.2 Computational Model

Molecular dynamics simulations of mechanical deformation of nc Cu [71, 72] and nc Ni [99] suggest that grain-boundary atoms as well as atoms up to 7-10 lattice parameters away from the grain boundary are heavily involved in plastic deformation. Deformation was mostly found to be taken up by atoms at and nearby grain boundaries. It was further suggested that the material near grain boundaries was easier to deform [71, 72] and that the associated deformation mechanisms are likely to be rate-sensitive [71, 72]. However, the specific deformation mechanisms have not yet been identified and more investigations are necessary. Here, the present study proposes the concept of a grain-boundary affected zone (GBAZ), which broadly refers to a region adjoining the grain boundaries in nc metals where the crystalline lattice is elastically strained despite the ostensible absence of any point defects. Atoms within this GBAZ are more likely to be involved in the deformation process. However, atomistic simulations are still very limited by the time-scale and consequently the strain-rate sensitivity of nc materials under realistic strain rates has not yet been studied.

In the available continuum-mechanics based models (e.g. [73, 74]), the change in mechanical properties as a function of grain size is based on a change in the volume fraction of a grain-boundary phase that is often assumed to be amorphous. A rate-dependent version was developed [100] also assuming a significant volume fraction of an amorphous grain-boundary phase.

Assuming a three-dimensional cubic grain structure, the volume percentage of the GBAZ can be estimated as:

Table 5.1: Estimation of the volume percentage of the GBAZ.

Grain size (nm)	Width of GBAZ (vol%)	
	Ten lattice parameters[a]	Seven lattice parameters[a]
20	44.1	32.6
30	31.3	22.7
40	24.2	17.4
50	19.7	14.1
300	3.5	2.4
400	2.6	1.8

[a] Lattice parameter for Ni: 0.352 nm [101]

$$\text{GBAZ vol\%} = \ 100\% - \frac{(d_{\text{GS}} - d_{\text{GBAZ}})^3}{d_{\text{GS}}^3} \tag{5.3}$$

where d_{GS} is the average grain size, and d_{GBAZ} is the thickness of the GBAZ from the grain boundary. A simple spherical grain model would result in the same equation as Eq. (5.3). Table 5.1 lists the estimated volume percentage of the GBAZ in nc and ufc Ni with different grain sizes. Considering a GBAZ of 10 lattice parameters, the volume percentages of GBAZ are estimated to be 44.1 vol% at $d_{\text{GS}} = 20$ nm and 2.6 vol% at $d_{\text{GS}} = 400$ nm.

The following assumptions are made in the GBAZ model:

i. A GBAZ in a nc or ufc material spans a distance of about 7-10 lattice parameters away from the grain boundary.

ii. The GBAZ is plastically much softer than the grain interior.

iii The GBAZ deforms with a positive rate sensitivity.

iv Under tensile loading conditions, a strain-based material damage criterion is introduced to capture the onset and progression of failure.

A simple power-law type rate-dependent constitutive response is used for the GBAZ:

Table 5.2: Materials parameters used in the model. Refer to Eq. (5.4) and Fig. 5-6

	E (GPa)	ν	Initial σ_y (GPa)	θ	m
Grain interior nc Ni	200	0.3	2.8	0	–
Grain interior ufc Ni	200	0.3	0.95	0	–
GBAZ	200	0.3	0.55	0	0.03

local damage initiation strain $\varepsilon_r = 100\%$; damage duration strain $\Delta\varepsilon_f = 1\%$; residual strength $\sigma_r = \frac{\sigma_y^{GBAZ}}{1000}$

$$\dot{\varepsilon}_p = \dot{\varepsilon}_o \left(\frac{\sigma}{\sigma_o} \right)^m \tag{5.4}$$

where $\dot{\varepsilon}_p$ is the plastic strain rate, $\dot{\varepsilon}_o$ is the reference strain rate, $\sigma_o = \sigma_o(\varepsilon_e)$ is the effective von Mises stress at the reference strain rate, ε_e is the effective strain, σ is the effective material strength at the current strain rate $\dot{\varepsilon}_p$, and m is the rate sensitivity exponent. Computational parametric studies were performed using a simple linear hardening constitutive behavior for both the grain interior and the GBAZ (see Fig. 5-6(a)), with the initial yield stress defined by σ_y and a strain-hardening rate defined by θ. For tensile loading conditions, a simple strain-based failure/damage criterion was postulated as the following. The material failure/damage initiates at $\varepsilon_p = \varepsilon_f$, and the material strength drops linearly to a residual strength of $\sigma_r(\sim 0)$ within an additional strain of $\Delta\varepsilon_f$. The accumulated plastic strain is considered to be decisive for material failure. No damage is introduced when material is deformed under compression, because void formation, the most dominant failure mechanism for the present material [92], is suppressed during compression.

For modeling uniaxial tensile tests of nc Ni, two-dimensional grains of hexagonal shape were separated by a finite border region of GBAZ, as shown schematically in Fig. 5-6(b). A unit cell model with periodic boundary conditions was used. Different GBAZ volume fractions can be studied by varying the GBAZ depth (d_{GBAZ}) in relation to the size of the grain interior. Meshes were designed such that the element size was comparable to the typical atomic diameter assuming that the grain size is tens of nanometer. Computational

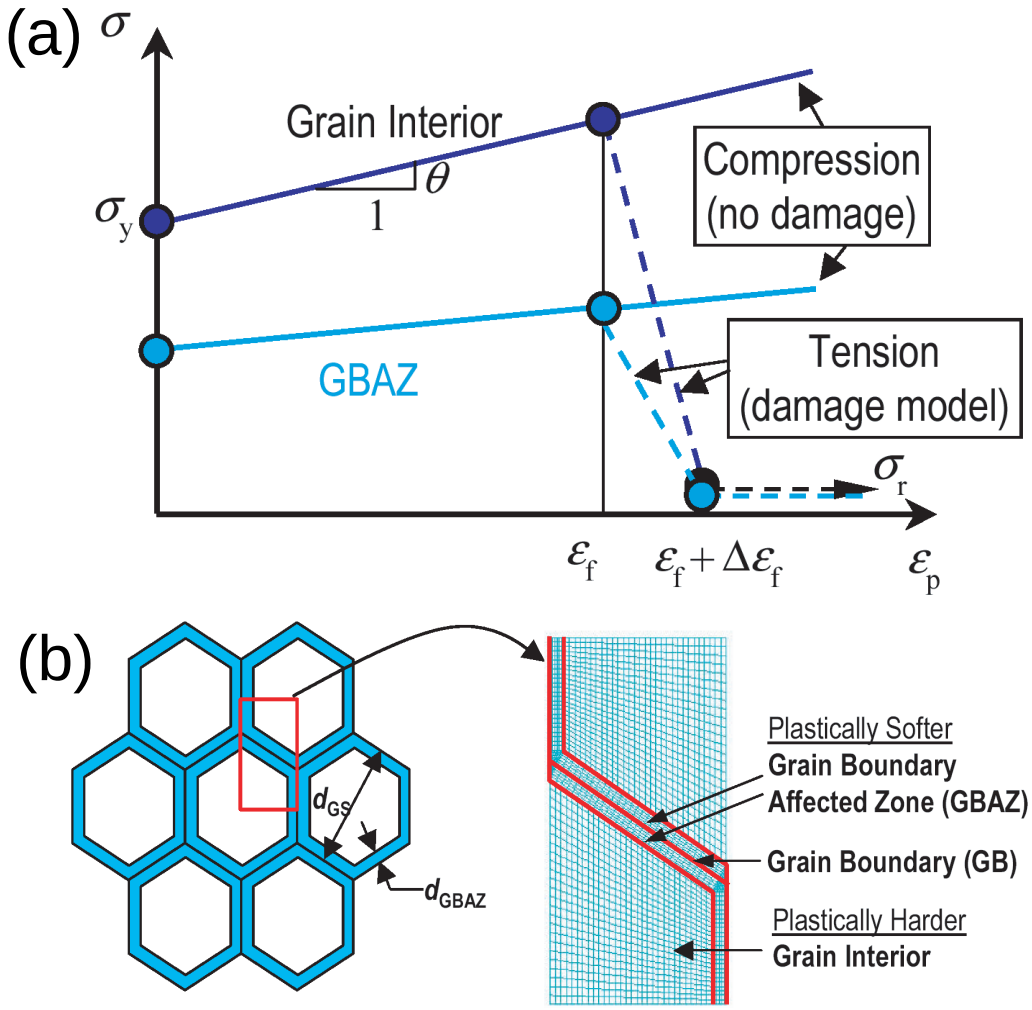

Figure 5-6: Schematic illustration of the computational model. (a) Linear hardening constitutive behavior for both the grain interior and the GBAZ with the initial yield stress σ_y and a strain-hardening rate θ. Material failure/damage under tension is assumed to initiate from $\varepsilon_p = \varepsilon_f$, and the material strength drops linearly to a residual strength of $\sigma_r(\sim 0)$ within an additional strain of $\Delta\varepsilon_f$. (b) Two-dimensional grains of hexagonal shape separated by the GBAZ preserving crystallinity to the atomically sharp grain boundary. Periodic boundary conditions were applied and a unit cell model was used in all computations.

results using two volume fractions of GBAZ, 2% (representing a grain size of 300-400 nm) and 25% (representing a grain size of 30-40 nm), will be presented. About 2500 elements were used in the computations. The material's parameters used in the calculations are summarized in Table 5.2.

For modeling indentation experiments, the following procedure was adopted. Computational tensile experiments without damage were conducted. The calculated effective tensile stress-strain curves at different strain rates were fitted using Eq. (5.4) in order to extract the material properties, which were used to calculate the load-displacement ($P-h$) response during indentation. Tensile as well as indentation behavior were consequently obtained using the same set of parameters describing the GBAZ and the grain interior. A commercial general-purpose finite element package, ABAQUS (version 6.3, ABAQUS Inc., Pawtucket, RI) was used. A user sub-routine was constructed in order to integrate the rate-sensitive hardening behavior.

Figures 5-7(a) and (b) show the computational stress-strain curves of ufc Ni and nc Ni, respectively; the results include the TS as well as failure predictions. For the ufc Ni almost no difference can be seen (Fig. 5-7(a)), whereas in case of the nc Ni, the TS as well as the strain at TS increase significantly with increasing strain rate (Fig. 5-7(b)). The flow stress and the TS of the ufc Ni can be seen to slightly increase with increasing strain rate, whereas the strain at TS decreased, which is different compared to the nc Ni.

Figures 5-8(a) and (b) show the predicted indentation curves of nc Ni at different indentation strain and load rates, respectively. The computed results capture the experimentally determined trend and show a similar magnitude of separation between different loading conditions (compare with Figs. 5-1(b) and 5-3(b)). Computational indentation results for ufc Ni are not illustrated here and showed vanishingly small differences between different strain rates, which is consistent with the experimental curves shown in Figs. 5-1(a) and 5-3(a).

Figure 5-9 shows the experimental and computational results from tensile tests for the nc and ufc Ni. For nc Ni, the offset yield stress at 1% plastic strain (open squares) increases from an average of about 1390 MPa to about 1540 MPa for a strain-rate increase from about 3×10^{-4} s^{-1} to 3×10^{-1} s^{-1}. No such strain rate effect was found in Ref. [8]

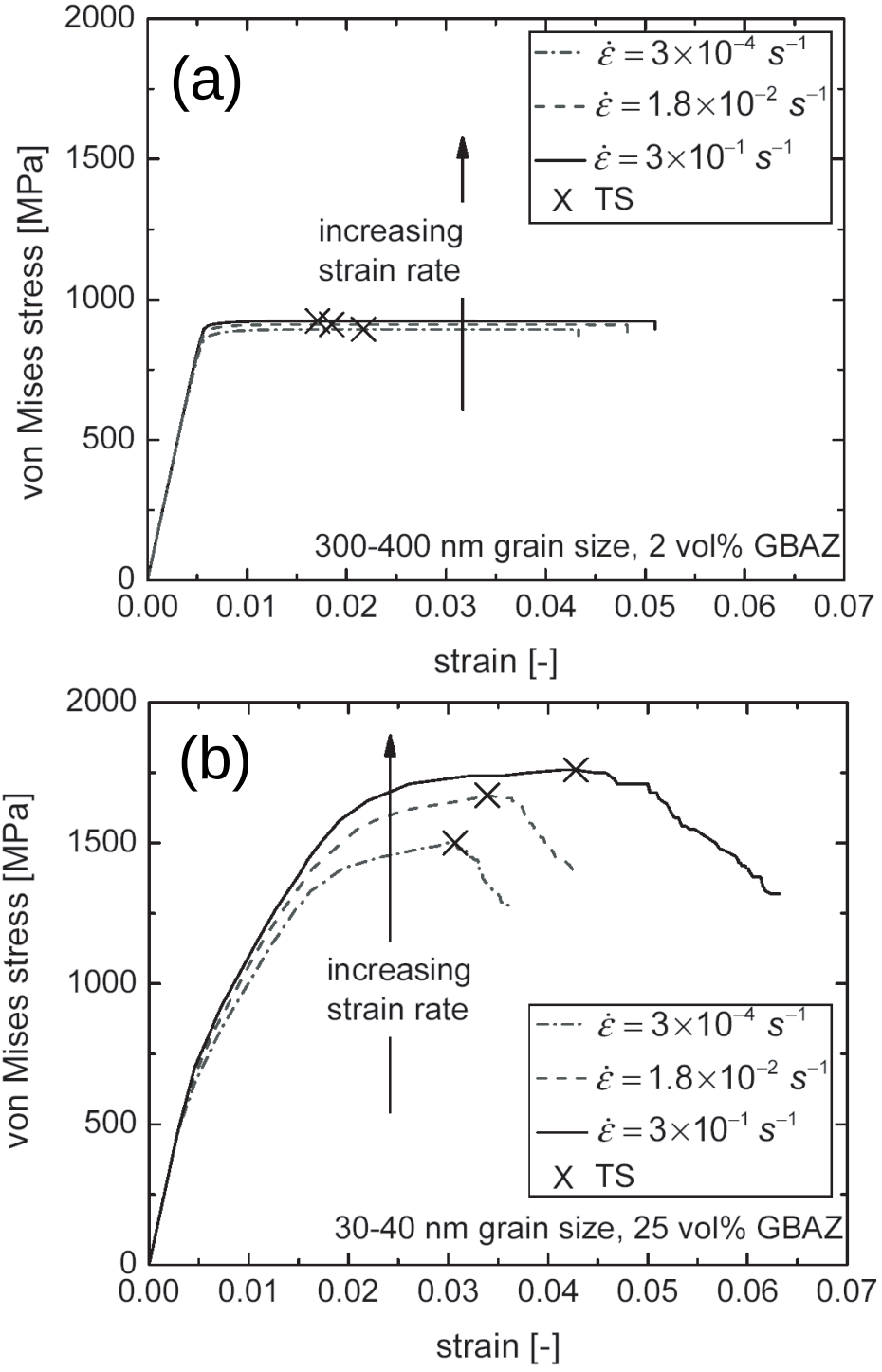

Figure 5-7: Computational stressstrain curves at three different strain rates for (a) ufc Ni and (b) nc Ni.

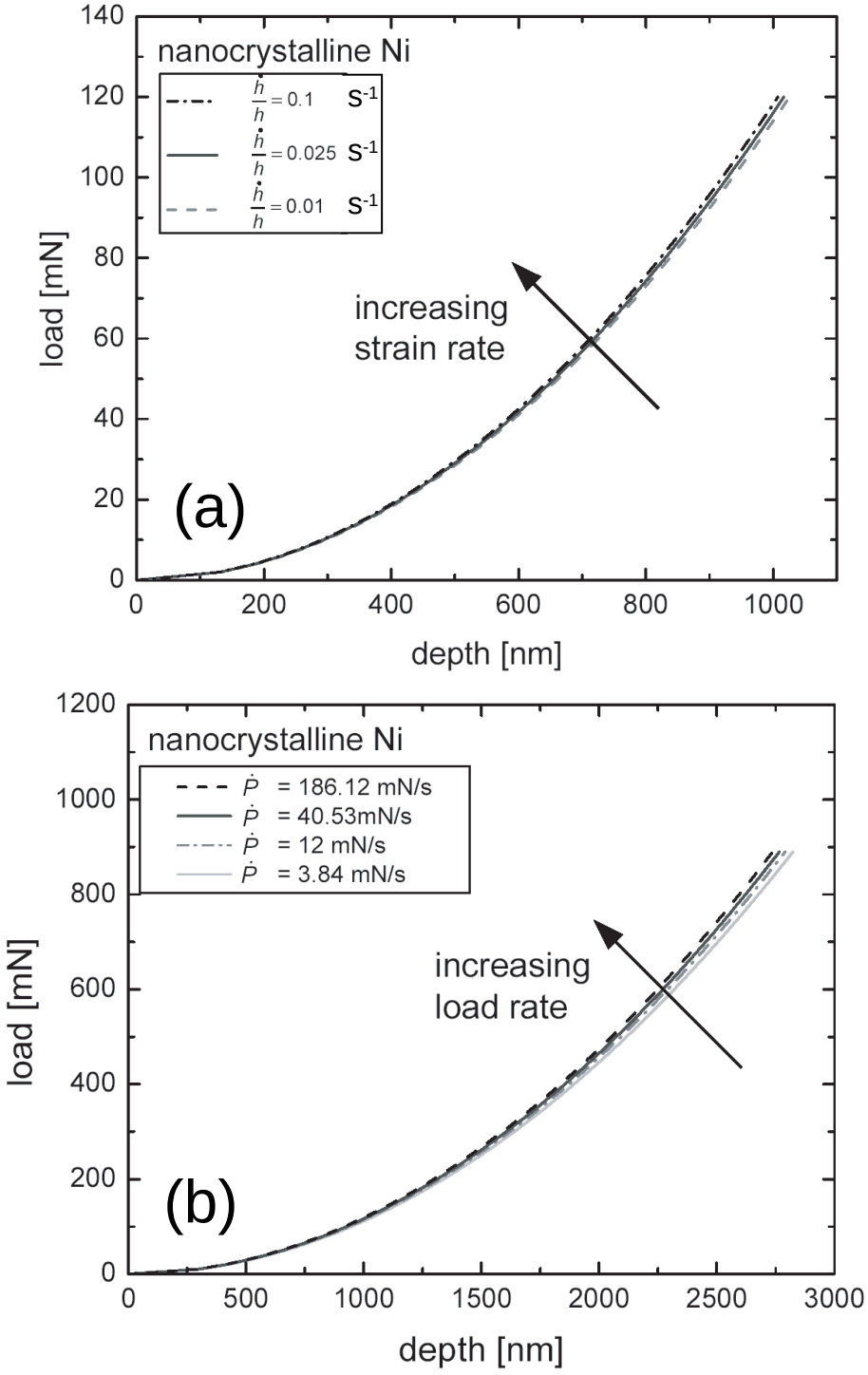

Figure 5-8: Computational $P-h$ curves for nc Ni obtained at (a) three different indentation strain rates and (b) four different load rates.

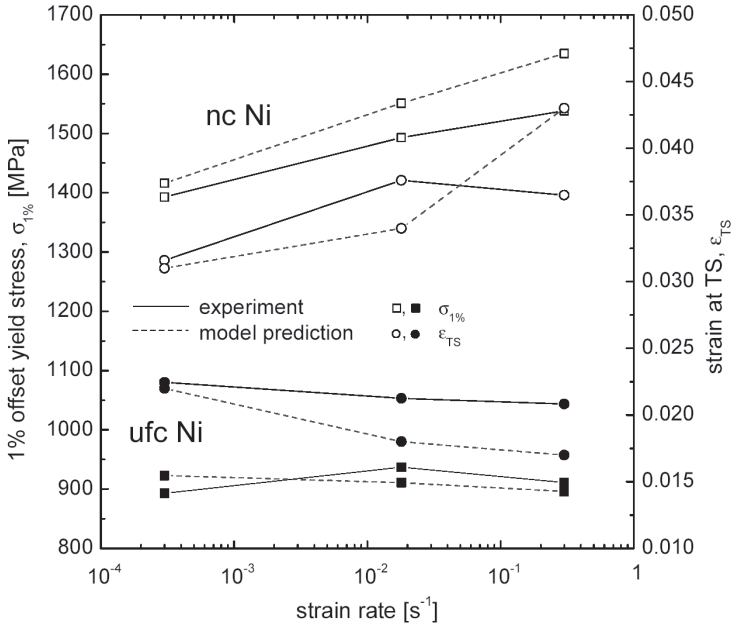

Figure 5-9: Comparison of experimental and computational results for tensile tests of nc and ufc Ni. The 1% offset yield stress and the strain at TS are shown versus strain rate.

for the same strain rates, although it has to be noted that the authors evaluated the TS rather than flow stress. Thus, the strength reported in Ref. [8] could be influenced by the onset of necking and therefore not necessarily comparable to the effect on flow stress at 1% plastic strain. In ufc Ni, an increase in flow stress with increasing strain rate could not be clearly identified (compare Fig. 5-9, filled squares). The experimentally found trends are also reflected in the computational results: the 1% offset yield stress is essentially constant in case of ufc Ni and increases with strain rate in case of nc Ni. It is further noted that the absolute values obtained from experiments and computations compare pretty well for the assumptions invoked in the model. Simultaneously, in nc Ni the strain at TS increased by about 0.5% from 3.16% to 3.65% indicating a slight ductility increase (Fig. 5-9, open circles). A grain size reduction from 320 to 40 nm resulted in an increase in strain at maximum stress from about 2% to more than 3% (Fig. 5-9), which is consistent with the computational results. In the case of the ufc as well as of the mc Ni tested, there was no significant changes of the stress-strain behavior with the applied strain rate within the scatter of the experimental data. Dalla Torre *et al.* [8] compared the failure strains and observed different behavior. For their nc material, the strains decreased with increasing

strain rate. However, the present results showed failure strain to be highly defect-sensitive and, hence, not to be sufficiently reliable to determine strain rate effects.

The indentation response of nc Ni is strongly affected by the applied strain or load rates, whereas no such behavior was found for the ufc specimens (Figs. 5-1-5-4). The indentation hardness at 1 μm depth increased from 5.7 GPa at $\dot{\varepsilon}_{\text{ind}} = 0.01\ s^{-1}$ to 6.4 GPa at $\dot{\varepsilon}_{\text{ind}} = 0.1\ s^{-1}$. A similar trend was observed at higher loads: the hardness increased by almost 10% when the loading rate was increased from 3.8 to 186.1 mN/s. This general behavior could be reasonably well captured by simulating the indentation response using the simple computational model introduced above. As the nc and ufc Ni foils have been produced by the same method, with comparable density and purity, it is likely that the observed rate sensitivity is a consequence of the grain size only. The fact that no strain-rate effect was observed in ufc Ni is not related to the smaller number of grains deformed during indentation. This was ensured by indenting to a depth of 2.8 μm where a significantly larger number of grains have been sampled, and still no such strain-rate effect occurred. However, a potential rate effect in the ufc material may be hidden due to the large scatter in experimental data. In particular, the $P-h$ curves to 1 μm depth of the ufc Ni show considerable variations. These variations could be related to the inhomogeneous grain structure at the specimen surface or variations in texture within the sampled volume. Furthermore, a deformation layer at the surface due to mechanical polishing is likely to be responsible for larger scatter. However, a strain-rate sensitive deformation behavior was not observed in the 2.8 μm deep indents or in the tensile tests, where the influence of the surface is negligible. Therefore, it was reasonable to attribute the hardness increase with increasing indentation strain rate in the nc Ni to the small grain size.

It is obvious from the present experimental results shown in Figs. 5-1-5-5 that the overall plastic deformation of nc Ni is highly rate-sensitive. Due to the lack of dislocation sources, the grain interior of the nc material is expected to deform at stress levels close to the theoretical strength. If the grain interior contributes only little to the overall plastic deformation, the rate-sensitivity observed in nc Ni would be expected to arise from the grain boundaries and the nearby regions, i.e. the GBAZ. Recent molecular dynamics simulations [102] suggest that thermally activated single atomic jumps near the grain boundaries in nc metals play a major role in plastic deformation corroborating the positive strain-rate

sensitivity of the GBAZ postulated in the model.

In the literature, conflicting trends of the dependence of failure strain on strain rate have been reported [7, 8]. The proposed computational as well as present experimental results show that in nc Ni the strain at TS increases with increasing strain rate. Note that the computed results represent the material's constitutive behavior assuming uniform deformation "everywhere" in the sample. However, this assumption is not valid beyond TS, since inhomogeneous deformation becomes dominant once necking occurs. Hence, the failure strain is very sensitive to material and sample imperfections. This could be a possible reason for the inconsistent trends reported in the literature.

5.5 Inverse Hall-Petch-Type Phenomenon

To further verify the proposed GBAZ model, additional parametric studies on grain size were conducted by recourse to the unit cell model developed in Section 5.4.2. The goal is to correlate the variation in flow stress to grain size variation in the nanometer range. Using the GBAZ concept, two competing factors are identified in nc materials.

i. Grain interior: as grain size decreases, the yield strength increases approaching the theoretical limit for the critical grain size too small to accommodate a single dislocation.

ii. GBAZ: as grain size decreases, the GBAZ volume percentage increases resulting in a decrease in yield strength because GBAZ is plastically softer than grain interior.

By properly invoking plastic behavior of grain interior and GBAZ at various grain size, the critical grain size can be attained. The grain size was determined by varying the GBAZ volume fraction in Eq. 5.3, with the assumption of three-dimensional cubic grain structure. To study the effect of grain structure assumption, a two-dimensional columnar structure of hexagonal cross-section was introduced in the parameter study, where grain size can be calculated from the volume percentage of the GBAZ via the simple geometrical relation,

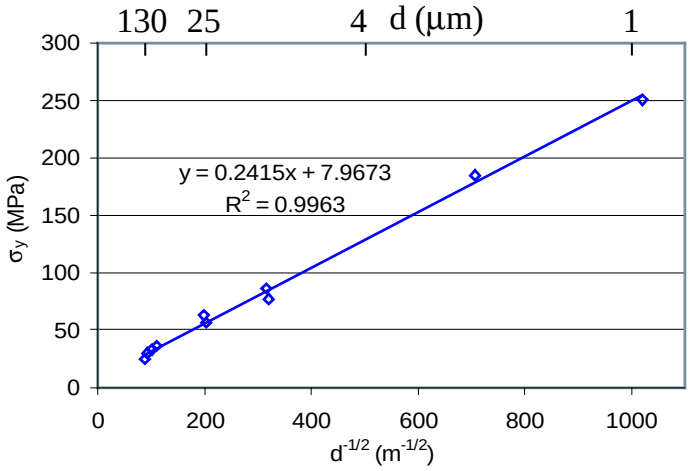

Figure 5-10: Literature data for microstructured Nickel superimposed with Hall-Petch relation.

$$\text{GBAZ vol\%} = \ 100\% - \frac{(d_{\text{GS, hex}} - \frac{2}{\sqrt{3}}\ d_{\text{GBAZ}})^2}{d^2_{\text{GS, hex}}} \tag{5.5}$$

The same constitutive relation for GBAZ is assumed, as shown in Table 5.2. Nonetheless, that for grain interior is grain size dependent. As discussed in Section 5.4.2, when the grain size is below the critical grain size geometrically necessary to accommodate a single dislocation (nc), the yield strength should approach the theoretical yield strength, as shown in Table 5.2. For the larger grain size (mc or ufc), the grain interior is able to accommodate dislocations, and thus the yield strength should follow the Hall-Petch relation described by

$$\sigma_{\text{HP}} = \sigma_{\text{yo}} + k_{\text{HP}} d^{-\frac{1}{2}} \tag{5.6}$$

$$\sigma_{\text{HP}} = 7.967 + 0.2415 d^{-\frac{1}{2}} \qquad \text{MPa } (d \text{ in meter}) \tag{5.7}$$

Figure 5-10 shows the Hall-Petch plot [103, 104] for pure nickel at grain size larger than 1 μm because the deviation from Hall-Petch relation becomes significant at grain size smaller than 1 μm (see Fig. 4 of [103]). Least-square fitted with Eq. (5.6), Fig. 5-10 yields the frictional stress (σ_{yo}) and Hall-Petch slope (k_{HP}) of 7.967 MPa and 0.2415 MPa·m$^{1/2}$ (or

Table 5.3: FEM parameter study for size effect.

Parameters	Values
GBAZ vol%	0.02, 0.05, 0.1, 0.15, 0.2, 0.25, 0.3, 0.35, 0.4, 0.45, 0.5
Grain size (d_{GS})	Eqs. (5.3) and (5.5)
Grain interior yield strength	σ_{TH} from Table 5.2 and σ_{HP} from Eq. (5.7)
GBAZ mechanical properties	Same as in Table 5.2
Strain rate	4.2×10^{-4}, 1.7×10^{-2} and 0.5 s^{-1}

7.636 GPa·$nm^{1/2}$) respectively (see Eq. (5.7)). As discussed in [105], the unusually low frictional stress from Fig. 5-10 agrees well with the hardness Hall-Petch data, provided that the Vickers hardness was approximately three times the compressive flow stress at 7.5% strain. It was later confirmed by another hardness experiment [106].

A systematic parameter study was performed on the grain size and grain interior plasticity. The grain sizes were varied from a few hundreds nanometer to tenths of nanometer by changing the GBAZ fraction in Eqs. (5.3) or (5.5). The grain interior plasticity assumed Hall-Petch or theoretical yield strengths for a given grain size. In addition, the simulation was performed at three different strain rates. Table 5.3 summarizes the model description for the current parameter study. As a result, the total number of simulations are 11 (GBAZ fraction) × 2 (grain structure assumption) × 2 (grain interior yield strength assumption) × 3 (strain rate) = 132 cases totally.

The simulations were performed using the general purpose finite element package ABAQUS Standard. Different strain rates were implemented in the similar fashion to the previous section. The resulting effective FEM stress-strain curves were collected, and the 1% offset flow stress was determined for each case. The choice of 1% offset strain was chosen rather than 0.2% because of a gradual deviation from the elasticity in the initial plastic regime of the FEM stress-strain curves. Figure 5-11 shows the normalized 1% offset flow stress with the shear modulus versus the logarithmic grain size from all cases in the parameter study. For the assumption of the theoretical yield strength within the grain, the weakening effect with decreasing grain size was observed. As the grain size began to

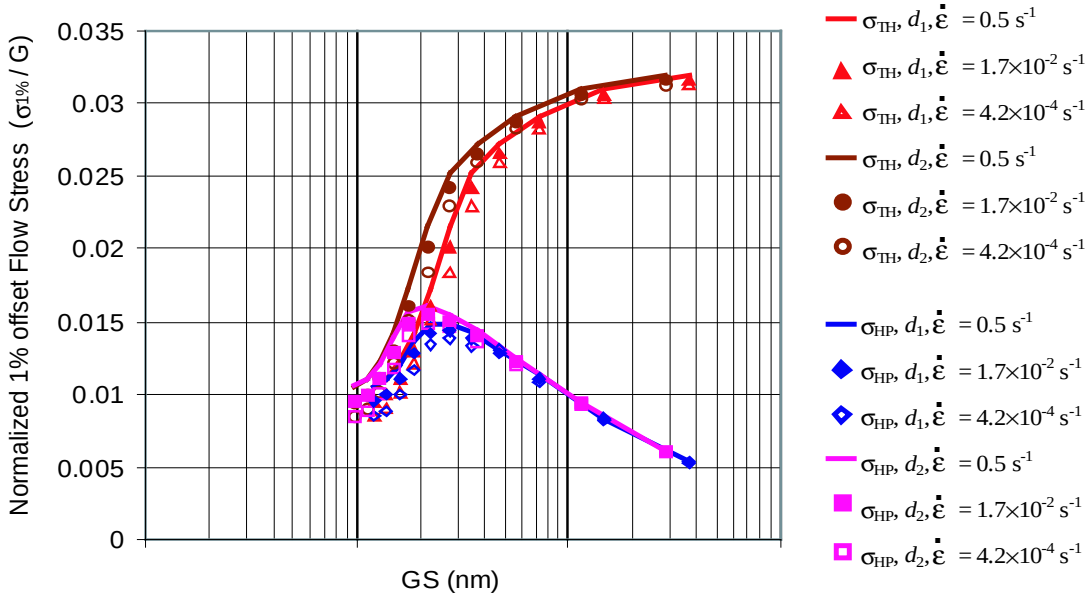

Figure 5-11: Normalized 1% offset flow stress versus grain size for various assumptions and strain rates.

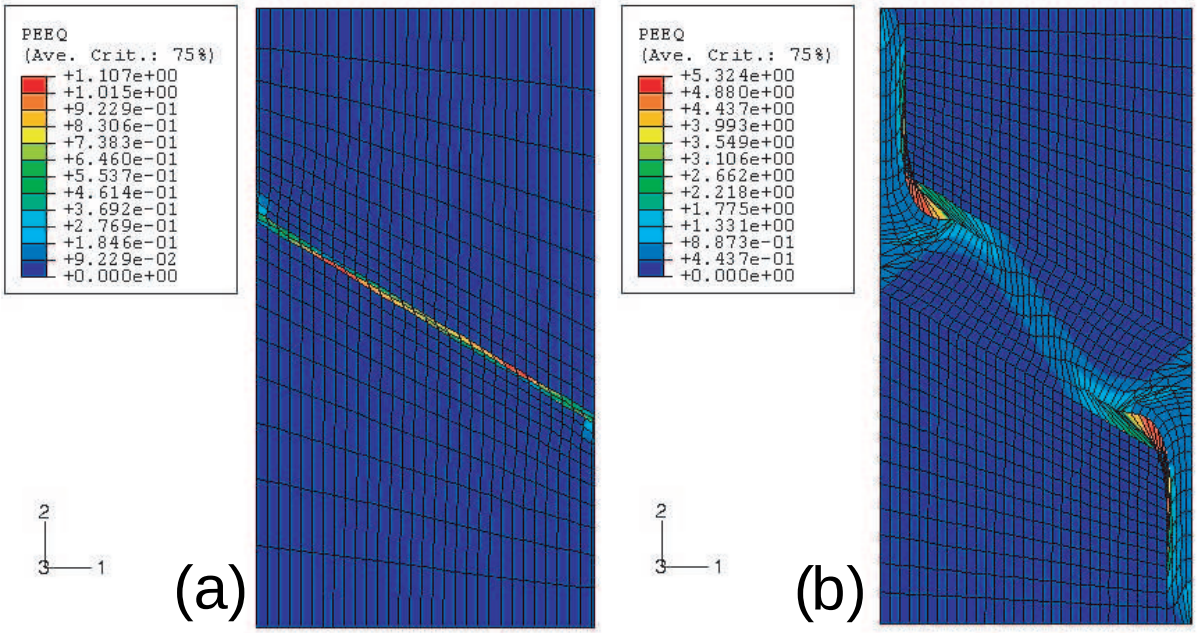

Figure 5-12: Contour plot of equivalent plastic strain assuming theoretical strength for grain interior with GBAZ fractions of (a) 2% and (b) 25%, both at a strain rate of 4.2×10^{-4} s^{-1}.

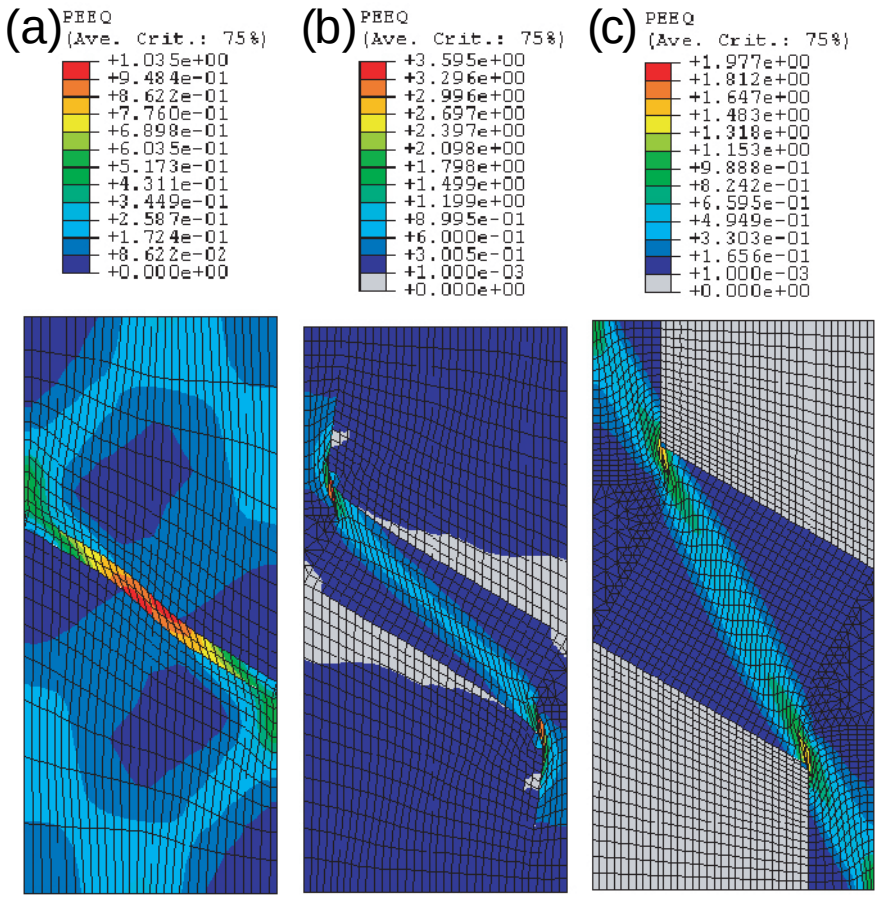

Figure 5-13: Contour plot of equivalent plastic strain assuming Hall-Petch yield strength for grain interior with GBAZ fractions of (a) 5%, (b) 25% and (c) 50%, all shown at a strain rate of 4.2×10^{-4} s^{-1}. Note the gray region denotes PEEQ < 0.001.

decrease from a few hundred nanometers, the 1% offset flow stress slightly decreased due to a small GBAZ fraction. At this end, the much stronger grain interior sustained most of the deformation elastically and dominated the overall response of the unit cell, as shown in Fig. 5-12(a). Due to localization within GBAZ, the overall normalized 1% offset flow stress was below (not exactly equal to) the normalized theoretical yield strength of the grain interior ($\frac{\sigma_{TH}}{G} \approx 0.04$). As the grain size decreased further below 100 nm, the 1% offset flow stress started to drop quickly because of the increasing contribution from the GBAZ region. Figure 5-12(b) depicts the heavily deformed mesh in the relatively large GBAZ region. In this range, the plastically weaker GBAZ region began to dominate the overall deformation of the unit cell, and thus lower the 1% offset flow stress dramatically.

For the assumption of the Hall-Petch yield strength within the grain, Fig. 5-11 shows that there is a transition from strengthening to weakening effects with decreasing grain size. The grain size at which this transition occurred was in the range of 20 - 30 nm, depending on the assumptions of the strain rate and the grain structure (Eqs. (5.3) and (5.5)), in accordance with the value reported in the literature [5, 65, 77–88]. As the grain size started to decrease from a few hundred nanometers, the 1% offset flow stress increased due to the increasing yield strength within the grain as predicted by Hall-Petch relation Eq. (5.7). Unlike the theoretical yield strength case above, Fig. 5-13(a) shows that both grain interior and GBAZ deform plastically. Since the GBAZ yield strength is fixed at 550 MPa (see Table 5.2) and the grain interior yield strength increases with decreasing grain size (Eq. (5.7)), the plastic deformation begins to localize in the GBAZ region as the grain size decreases. Figure 5-13(b) shows the contour plot of the equivalent plastic strain at 25% GBAZ fraction where the normalized 1% offset flow stress is maximized (open diamond symbol in Fig. 5-11). The fact that the gray region in the mesh experienced less than 0.1% equivalent plastic strain implies that the plastic deformation begins to conform within the GBAZ region. This conclusion is further confirmed in Fig. 5-11(c) where the entire grain interior experienced less than 1% equivalent plastic strain (gray region) for the case of 50% GBAZ fraction.

Figure 5-11 also indicates that below the transition grain size, the normalized 1% offset flow stress curves overlap regardless of the assumption in grain interior yield strength. As mentioned previously, the assumption of theoretical yield strength within the grain is favored below the critical grain size whereas that of Hall-Petch yield strength is favored above the critical grain size. Although the two curves overlap, it does not necessary mean that both underlying assumptions are the correct mechanisms. The Hall-Petch response happens to overlap the theoretical curve plausibly because once the grain interior yield strength exceeds the GBAZ yield strength by certain amount, all the plastic deformation is confined in the GBAZ region. Hence, the global yielding of the unit cell is dominated by the GBAZ plasticity regardless of the grain interior yield strength.

The strain rate effect is also captured in Fig. 5-11. In spite of the assumption in grain interior yield strength, the normalized 1% offset flow stress increases with increasing strain rate (from open symbol, filled symbol to line) because the faster strain rate strengthens the

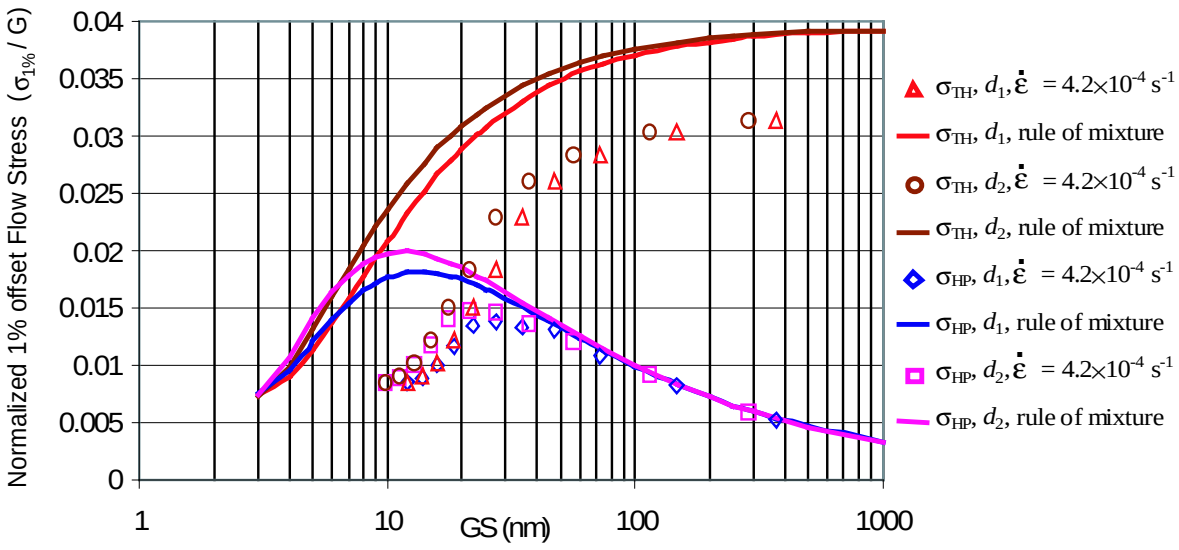

Figure 5-14: Comparison of strength predicted by rule of mixture and GBAZ unit cell model.

GBAZ region as explained in Section 5.4.2. The strain rate effect is more pronounced as the grain size decreased due to a larger GBAZ fraction. The upward shift in the normalized 1% offset flow stress also shifts the transition grain size in the Hall-Petch case to the left by about 10 nm.

In comparison with the FEM results, the present study follows a simple rule of mixture approach [74, 100, 107, 109–112] that envisages the nanocrystalline materials as a composite structure of two phases: grain interior and GBAZ. The yield strength is estimated via the following equation.

$$\sigma = f_{\mathrm{GBAZ}}\sigma_{\mathrm{GBAZ}} + (1 - f_{\mathrm{GBAZ}})\sigma_{\mathrm{Grain}} \tag{5.8}$$

where σ_{Grain} assumes theoretical or Hall-Petch yield strength, and f_{GBAZ} is determined from Eq. (5.3) or (5.5) depending on the grain structure assumption. Therefore, the total of four analytical expressions are constructed. Since the rule of mixture prediction Eq. (5.8) has no rate-dependent term, it is fair to compare the rule of mixture result to the unit cell result at the slowest strain rate (quasi-static approximation), as shown in Fig. 5-14.

It is obvious that rule of mixture result has the similar trend as the GBAZ result but the absolute values are different. This discrepancy directly reflects the underlying assumption in the rule of mixture model. The damage distribution within each phase is predetermined from the volume fraction; whereas, such distribution is determined from inter- and intra-phase interaction in GBAZ model. No matter how many phases (e.g. crystallite, grain boundary, triple junction and quadruple node) [100, 113, 114] are identified in the composite model Eq. (5.8) (volume percentage weighted sum), phase interaction is not accounted for unless there is a product term between different phases. For a large grain size, the rule of mixture predicts a yield strength close to the theoretical value ($\frac{\sigma_{\mathrm{TH}}}{G} \approx 0.04$); whereas, the localization predicted by GBAZ model lowers an estimate for the yield strength. The same reason can be used to explain the relative shift of the rule of mixture curve to the left.

5.6 Conclusions

In this chapter, strain-rate sensitivity of nanocrystalline nickel was investigated by recourse to systematic well-controlled experiments and continuum-micromechanics based model (i.e. GBAZ model). The GBAZ model was further utilized in the parameter study of grain size dependent flow stress in the mc, ufg and nc ranges. The key results can be summarized as follows.

1. Nanocrystalline pure nickel was found to exhibit a positive strain-rate sensitivity in flow stress, an effect that was not found in ufc and mc nickel. This rate sensitivity was confirmed by two independent experimental methods, namely depth-sensing indentation and tensile testing. The strain-rate sensitivity was observed to be related to the grain size.

2. A simple computational model with a strain-rate sensitive GBAZ that is softer than the grain interior has been introduced. The model, implemented in conjunction with finite element analysis, captures the general trends observed in the present experiments.

3. Two competing grain size dependent factors were identified and modeled quantitatively using GBAZ model in the finite element analysis.

4. The proposed GBAZ model predicts consistent critical transition grain size with literature values ($\approx$ 10-30 nm).

5. For the same set of constitutive description, consistent results obtained for both rate effect and size effect in nanocrystalline nickel.

Chapter 6

Concluding Remarks and Suggestions for Future Work

The key contributions of this thesis, as a result of experimental, analytical and computational approaches, are the following.

1. Comprehensive parameter studies of indentation simulation within the context of large deformation finite element analysis establish the forward and reverse algorithms. The forward algorithms predict indentation response from a given set of elasto-plastic properties; whereas, the reverse algorithms extract the empirical constitutive relation from a single set of indentation response. Experimental verifications show improvement over other methods previously proposed in the literature. The uniqueness issue is discussed and the conditions leading to unique predictions are identified. The representative strain of 3.3% plastic strain proposed herein is illustrated in consistency with previously proposed values in the literature. Extensive sensitivity analyses of tip angle, forward and reverse algorithms are conducted and the results are statistically analyzed. The extracted plastic properties are markedly sensitive to even small variation in the indentation response.

2. Based on the robustly predicted stress at representative strain proposed for single indentation, the forward and reverse algorithms are extended to indentation using

two or more tip geometries (tip half angle of between 50° and 80°). Experimental verifications, using a 60° cone equivalent three-sided pyramid tip, illustrate improved accuracy over the previously proposed algorithms for single indentation with Vickers/Berkovich tip. The representative strain is correlated with the indenter tip half angle. Significant reduction in the scattering is illustrated for reverse algorithm sensitivity; whereas, a similar result is obtained for forward algorithm. The non-uniqueness issue is completely resolved, at least for the range of parameter study, with a second tip geometry, as clearly illustrated by a non-uniqueness example suggested in the literature.

3. The experimental assessment of the stress at representative strain, predicted in reverse algorithms, is illustrated with possible avenues for utilization of the representative stress concept to predict an entire stress-strain curve more accurately and less sensitive.

4. Based on the evidences provided by *in situ* and *ex situ* transmitted electron microscope and detailed atomistic calculation of nanocrystalline materials, a simple analytical model is proposed to capture the observed trend in rate-sensitive deformation. The model is predicated upon the premise that grain boundary is atomically sharp; atoms nearby grain boundary (Grain-Boundary-Affected-Zone) is likely to move upon deformation and possesses positive rate-sensitivity constitutive relation. Finite element analysis integrating this GBAZ model well captures trends in rate-dependent mechanical properties observed in both micro-tension and indentation experiments. With the concept of GBAZ model, two competing grain size dependent factors are identified and modeled quantitatively using GBAZ-integrated finite element analysis. Using the same set of GBAZ model parameters, critical transition grain size is predicted to be consistent with literature values.

5. Interactive computer software is constructed to facilitate the implementation of the proposed forward and reverse algorithms for both single and dual indentations. The forward algorithms interface is often used to estimate the maximum load range required to achieve desired indentation depth in a load-controlled indentation apparatus, if the mechanical properties of the samples are approximately known. On the other hand, the reverse algorithms interface is particularly beneficial for analysis of large

amount of indentation data. The software is also capable of performing comprehensive sensitivity analysis of forward/reverse algorithms and machine compliance.

With an ever-increasing utilization of depth-sensing instrumented indentation technique as an experimental tool to extract and study mechanical properties of small-volume materials, the fundamental and technological development established in this thesis has laid out explicitly the step-by-step methodology in solving complex multi-stress state indentation problem. For instance, this indentation methodology can be extended to (i) materials with additional dimensional/geometrial constraints (e.g. passivated/unpassivated thin film, line and island), (ii) materials with other constitutive laws (e.g. visco-elastic/plastic, pressure-sensitive and temperature-dependent), (iii) materials under various deformation mode (e.g. dynamic impact, creep and fatigue), and of course any combination of these situations. Some of these extensions have already been attempted by various researchers and the results can be found in the literature. Each complication introduces additional degrees of freedom and variables in the calculation, which would require larger amount of parametric study cases to ensure the accuracy of the prediction.

Appendix A

Dimensionless Functions

A.1 Single Indentation Algorithms

In this section, six of the dimensionless functions identified in Chapter 2, i.e. Π_1, Π_2, Π_3, Π_4, Π_5, and Π_6, are listed explicitly.

$$\Pi_1 = \frac{C}{\sigma_{0.033}} = -1.131\left[\ln\left(\frac{E^*}{\sigma_{0.033}}\right)\right]^3 + 13.635\left[\ln\left(\frac{E^*}{\sigma_{0.033}}\right)\right]^2 - 30.594\left[\ln\left(\frac{E^*}{\sigma_{0.033}}\right)\right] + 29.267 \tag{A.1}$$

$$\begin{aligned}\Pi_2\left(\frac{E^*}{\sigma_{0.033}}, n\right) &= \frac{1}{E^* h_\mathrm{m}} \left.\frac{\mathrm{d}P_\mathrm{u}}{\mathrm{d}h}\right|_{h_\mathrm{m}} = \\ &(-1.40557n^3 + 0.77526n^2 + 0.15830n - 0.06831)\left[\ln\left(\frac{E^*}{\sigma_{0.033}}\right)\right]^3 + \\ &(17.93006n^3 - 9.22091n^2 - 2.37733n + 0.86295)\left[\ln\left(\frac{E^*}{\sigma_{0.033}}\right)\right]^2 + \\ &(-79.99715n^3 + 40.55620n^2 + 9.00157n - 2.54543)\left[\ln\left(\frac{E^*}{\sigma_{0.033}}\right)\right] + \\ &(122.65069n^3 - 63.88418n^2 - 9.58936n + 6.20045)\end{aligned} \tag{A.2}$$

$$\Pi_3\left(\frac{\sigma_{0.033}}{E^*}, n\right) = \frac{h_\mathrm{r}}{h_\mathrm{m}} = (0.010100n^2 + 0.0017639n - 0.0040837)\left[\ln\left(\frac{\sigma_{0.033}}{E^*}\right)\right]^3 + (0.14386n^2 + 0.018153n - 0.088198)\left[\ln\left(\frac{\sigma_{0.033}}{E^*}\right)\right]^2 + (0.59505n^2 + 0.034074n - 0.65417)\left[\ln\left(\frac{\sigma_{0.033}}{E^*}\right)\right] + (0.58180n^2 - 0.088460n - 0.67290) \quad \text{(A.3)}$$

$$\Pi_4\left(\frac{h_\mathrm{r}}{h_\mathrm{m}}\right) = \frac{p_\mathrm{ave}}{E^*} \approx 0.268536\left(0.9952495 - \frac{h_\mathrm{r}}{h_\mathrm{m}}\right)^{1.1142735} \quad \text{(A.4)}$$

$$\Pi_5\left(\frac{h_\mathrm{r}}{h_\mathrm{m}}\right) = \frac{W_\mathrm{p}}{W_\mathrm{t}} = 1.61217\left\{1.13111 - 1.74756^{\left[-1.49291\left(\frac{h_\mathrm{r}}{h_\mathrm{m}}\right)^{2.535334}\right]} - 0.075187\left(\frac{h_\mathrm{r}}{h_\mathrm{r}}\right)^{1.135826}\right\} \quad \text{(A.5)}$$

$$\Pi_6 = \frac{1}{E^*\sqrt{A_\mathrm{m}}}\left.\frac{\mathrm{d}P}{\mathrm{d}h}\right|_{h_\mathrm{m}} = c^* \quad \text{(A.6)}$$

where values of c^* are tabulated in Table 2.3

A.2 Dual Indentation Algorithms

In this section, four of the dimensionless functions identified in Chapter 3, i.e. $\Pi_{1\mathrm{b}}$, $\Pi_{1\mathrm{c}}$, $\Pi_{1\mathrm{d}}$, and $\Pi_{1\theta}$, are listed explicitly. Note that the subscript "a" denotes the single indenter equation with apex angle of 70.3^o (i.e., $\Pi_{1\mathrm{a}} = \Pi_1$ from Eq. (A.1), $\Pi_{2\mathrm{a}} = \Pi_2$ from Eq. (A.2), ...)

$$\text{For } \theta = 60^o, \quad \Pi_{1\mathrm{b}} = \frac{C_\mathrm{b}}{\sigma_{0.057}} = -0.154\left[\ln\left(\frac{E^*}{\sigma_{0.057}}\right)\right]^3 + 0.932\left[\ln\left(\frac{E^*}{\sigma_{0.057}}\right)\right]^2 + 7.657\left[\ln\left(\frac{E^*}{\sigma_{0.057}}\right)\right] - 11.773 \quad \text{(A.7)}$$

$$\text{For } \theta = 80^o, \qquad \Pi_{1c} = \frac{C_c}{\sigma_{0.017}} = -2.913\left[\ln\left(\frac{E^*}{\sigma_{0.017}}\right)\right]^3 + 44.023\left[\ln\left(\frac{E^*}{\sigma_{0.017}}\right)\right]^2 - 122.771\left[\ln\left(\frac{E^*}{\sigma_{0.017}}\right)\right] + 119.991 \tag{A.8}$$

$$\text{For } \theta = 50^o, \qquad \Pi_{1d} = \frac{C_d}{\sigma_{0.082}} = 0.0394\left[\ln\left(\frac{E^*}{\sigma_{0.082}}\right)\right]^3 - 1.098\left[\ln\left(\frac{E^*}{\sigma_{0.082}}\right)\right]^2 + 9.862\left[\ln\left(\frac{E^*}{\sigma_{0.082}}\right)\right] - 11.837 \tag{A.9}$$

For any θ in [50^o,80^o], the general fit function for $\Pi_{1\theta}$ is

$$\begin{aligned}\Pi_{1\theta} = \frac{C_\theta}{\sigma_{\epsilon_r}} = {} & (-2.3985\times10^{-5}\theta^3 + 6.0446\times10^{-4}\theta^2 + 0.13243\theta - 5.0950)\left[\ln\left(\frac{E^*}{\sigma_{\epsilon_r}}\right)\right]^3 + \\ & (0.0014741\theta^3 - 0.21502\theta^2 + 10.4415\theta - 169.8767)\left[\ln\left(\frac{E^*}{\sigma_{\epsilon_r}}\right)\right]^2 + \\ & (-3.9124\times10^{-3}\theta^3 + 0.53332\theta^2 - 23.2834\theta + 329.7724)\left[\ln\left(\frac{E^*}{\sigma_{\epsilon_r}}\right)\right] + \\ & (2.6981\times10^{-3}\theta^3 - 0.29197\theta^2 + 7.5761\theta + 2.0165)\end{aligned} \tag{A.10}$$

Appendix B

Microsoft® Excel Program for Automatic Forward/Reverse Analysis

This chapter aims to provide a detailed explanation of the Microsoft® Excel Macro program constructed to facilitate the automatic analysis of forward/reverse algorithms proposed in Chapters 2 and 3. For reverse algorithms (that enable the extraction of elasto-plastic properties from a given set of indentation data), the program also incorporated those methods proposed by Doerner and Nix [25], Oliver and Pharr [27] and Suresh *et al.* [38, 41, 42] for comparison. In addition, the algorithms to extract fracture toughness [115] and residual stress [43, 44] from instrumented sharp indentation have been implemented for broader usage of the current program. This chapter is intended not to explore in depth into these two topics; therefore, the readers may refer to the wealth of literature (e.g. [115–130] for fracture toughness and [31, 43, 44, 131–133] for residual stress determinations, among many others)

Although the Visual Basic based optimizer toolbox "Solver" in Microsoft Excel may not be as accurate as the optimization toolbox in Matlab, the current Macro program has been extensively verified and tested against various higher-level numerical solving tools (e.g. Matlab, Maple and Fortran language) to ensure the accuracy within the scope of the

computation involved in forward/reverse algorithms. The obvious advantages of choosing Microsoft Excel for numerical solving are the user-friendly (Point-and-Click) interface, easy transferability and worldwide availability of Microsoft Office. The current capabilities of the Macro program are

- the forward algorithms for Berkovich (or Vicker, 70.3^o cone) indenter [3, 4, 22, 35, 38, 39, 41, 42] and for 60^o cone (or the 3-sided equivalent pyramid) indenter [59];
- the reverse algorithms for Berkovich (or Vicker, 70.3^o cone) indenter [3, 4, 22, 25, 27, 35, 38, 39, 41, 42] and for dual (Berkovich and 60^o cone) indenters [59];
- sensitivity analyses of machine compliance and single/dual forward/reverse algorithms;
- single/batch calculation of single/dual forward/revese algorithms;
- fracture toughness estimation*; and
- tensile/compressive elastic residual stress and plastic residual strain determination†.

B.1 Requirement

In order to use this Macro program, the computer must have Microsoft Excel installed with the Solver Add-in‡. In addition, ensure that Microsoft Visual Basic is aware of Solver library as follows. On Microsoft Visual Basic toolbar, Tools → References → check the SOLVER BOX. If it shows "MISSING: SOLVER", highlight it and click Browse. Search for Microsoft Excel solver library (typically C:\Program Files\Microsoft Office\Office\Library\Solver\Solver.xla).

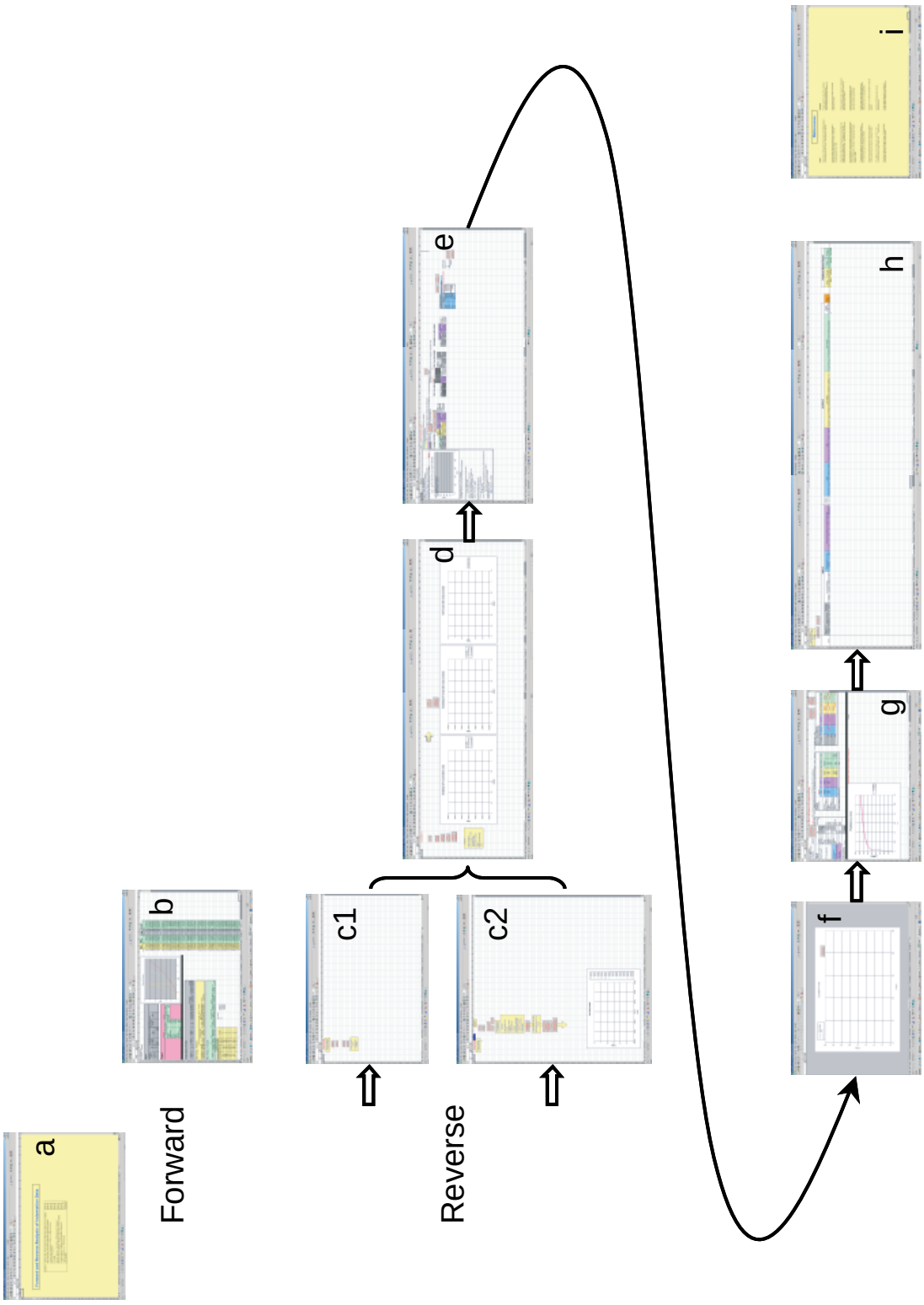

Figure B-1: Schematic overview of Microsoft Excel Macro program coded for Forward/Reverse algorithms: a) front introductory page, (b) forward analysis, (c)-(h) reverse analysis and (i) last reference page

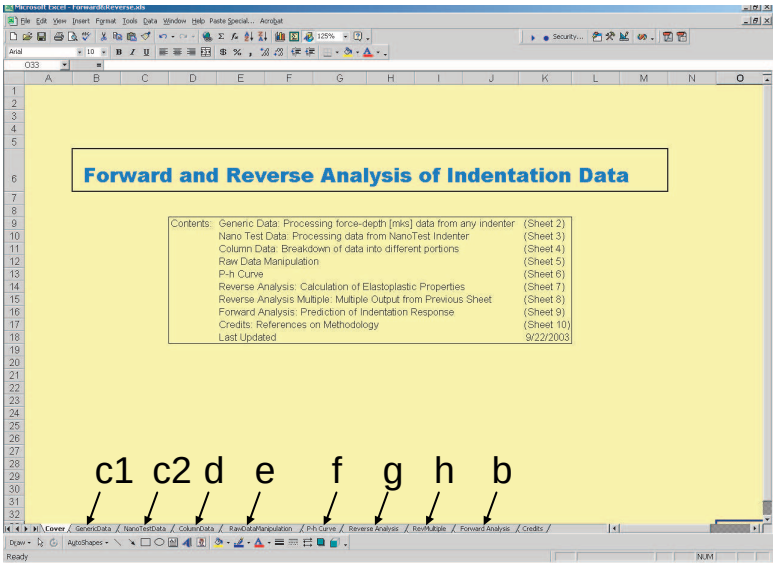

Figure B-2: Zoom in of Fig. B-1(a) showing the worksheet "Cover" of the Macro program

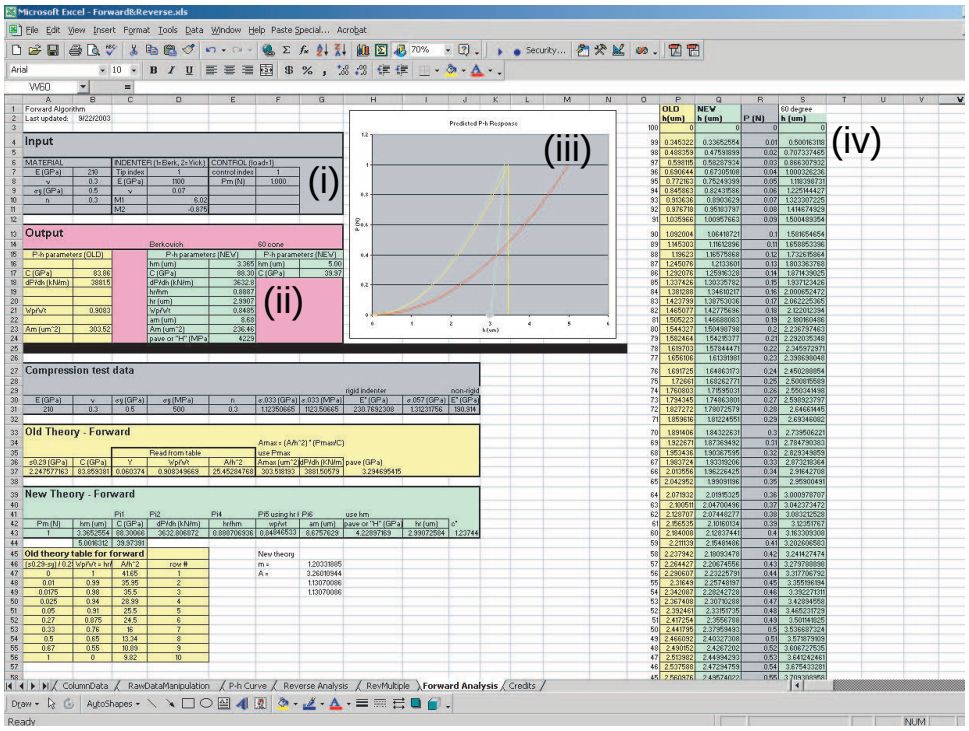

Figure B-3: Zoom in of Fig. B-1(b) showing the worksheet "Forward Analysis" of the Macro program

B.2 Forward Algorithms

The schematic overview of the Macro program is shown in Fig. B-1. Figs. B-1(a) and B-1(i) are the first and last worksheets in the Excel file, and do not have any program code (see a magnified version in Fig. B-2 and Fig. B-11). Fig. B-1(b) is the stand-alone worksheet used in forward algorithms, which is magnified and shown in Fig. B-3 with the following details.

(i) The input region for elasto-plastic properties of the material ($E, \nu, \sigma_{\mathrm{y}}$ and n), elastic properties of the indenter tip ($E_{\mathrm{i}} and \nu_{\mathrm{i}}$) and maximum indentation load (P_{m}).

(ii) The output region for the predicted indentation characteristics (C, $\frac{h_{\mathrm{r}}}{h_{\mathrm{m}}}$, $\frac{W_{\mathrm{p}}}{W_{\mathrm{t}}}$, $\frac{\mathrm{d}P}{\mathrm{d}h}\big|_{h_{\mathrm{m}}}$, p_{ave}, a_{m}, A_{m}) for Berkovich and C_{b} for 60^o cone.

(iii) The predicted indentation response using the information shown in region (ii).

(iv) The data points used to construct the indentation curves shown in region (iii).

B.3 Reverse Algorithms

Figs. B-1(c) - B-1(h) are the worksheets used in the reverse analysis. The sequence of computation is as follows.

1. Indentation data (from $P-h$ curve) can be imported using worksheet "GenericData" (Fig. B-1(c1)) or worksheet "NanoTestData" (Fig. B-1(c2)) depending on the data format. Worksheet "NanoTestData" is customized for the data format obtained from the commercial nanoindenter (MicroMaterials, Wrexham, UK); otherwise, worksheet "GenericData" should be used for any other data format. Fig. B-1(c1) is magnified and shown in Fig. B-4 with the following details.

*requires a measurement of radial crack length after complete unloading
†requires an indentation response of the same material without residual stress
‡refer to Microsoft Excel manual.

(i) The input region for indentation data points obtained from any commercial indenter: force (Newton) and depth (meter) go to column A and B, respectively.

(ii) Manual machine compliance (meter/Newton) can be entered at the cell "C1".

(iii) Button "Initialize" is designed to clear all the data in this and subsequent worksheets; whereas, button "Clear" is designed to only clear the data in this worksheet. Button "Format" is designed to format indentation data point for further calculation. Once the indentation data is format, click button "Proceed" to go to next stage of calcuation (worksheet "ColumnData," as shown in Fig. B-6.

On the other hand, (for indentation data from MicroMaterials indenter) Fig. B-1(c2) is magnified and shown in Fig. B-5 with the following details.

(i) The input region for indentation data points obtained from MicroMaterials indenter (file extension .ldd).

(ii) Manual machine compliance (meter/Newton) can be entered singly at the cell "C1," or multiply as a column starting at cell "C6". The latter suggests the parametric study of machine compliance. By default, the program always looks for a machine compliance in either cell "C1" or column starting at cell "C6".

(iii) Button "Initialize" is designed to clear all the data in this and subsequent worksheets; whereas, button "Clear" is designed to only clear the data in this worksheet. Button "Separate" is designed to separate each individual indentation test from a raw data in columns A & B. Button "BatchCalc" is designed to automatically perform the complete reverse analysis on all indentation tests listed in columns A & B; whereas, button "BatchCalcMC" extends "BatchCalc" to a series of machine compliance entered as the column starting at cell "C6".

(iv) Button "CopyHighlightedToNextPage" is designed to copy the highlighted column pair to the next step (worksheet "ColumnData," as shown in Fig. B-6).

(v) Button "BatchCalcIfAlreadySeparated" is designed to automatically perform the complete reverse analysis on all the already separated indentation pairs from columns H rightward; whereas, button "BatchCalcKicksOnlyIfAlreadySeparated" only performs Kick's fit (see Eq. (2.1)). Button "BatchCalcMCKicksOnly" limits "BatchCalcMC" to only the Kick's fit.

(vi) The indentation responses in column H rightward are previewed here.

2. Next step of reverse analysis is to identify the loading and the first 67% of the unloading portion for each indentation curve. Fig. B-1(d) is magnified and shown in Fig. B-6 with the following details.

   (i) Each indentation curve is copied from the previous step into columns A & B.

   (ii) Button "Clear" is designed to only clear the data in this worksheet. Button "BreakToColumn" is designed to section a single indentation curve into the loading portion, the first 67% of the unloading portion and the remaining 23% of the unloading portion. Button "CopyToNextPage" is designed to copy all three portions of the single indentation curve to the next step (worksheet "RawDataManipulation," as shown in Fig. B-7). Button "CreepCorrection" is designed to remove any creep remaining in the indentation curve during the hold at maximum load. Button "CopyCreepCorrectionToNextPage" is designed to copy all three portions of the single indentation curve that is already corrected for creep to the next step (worksheet "RawDataManipulation," as shown in Fig. B-7).

   (iii) The indentation curve showing three sections.

   (iv) Button "FullPhNoCreep" is designed to assemble three sections (with creep correction) of the indentation curve.

   (v) The indentation curve showing three sections after creep correction.

   (vi) The assembled indentation curve after creep correction.

3. Next step of reverse analysis is to fit the loading portion to Kick's law (Eq. (2.1)) and the first 67% of the loading portion to the power law $P = A(h - h_r)^m$ (see Section 2.3.2). Fig. B-1(e) is magnified and shown in Fig. B-7 with the following details.

   (i) Log-log plot of the loading portion (ignore the first 10%) superimposed with the best fit.

   (ii) The loading portion of the indentation curve is shown in columns H & I.

   (iii) Button "Reset" is designed to reset all fitting parameter in this worksheet. Button "Kickonly 2nd Indenter" is designed to only fit the loading portion with Kick's law. Button "Analyze" is designed to both fit the loading portion with

Kick's law and the first 67% of the unloading portion with a power law. Button "Analyze More" is designed to repeat "Analze" if the resultant fits are not satisfied by the user.

(iv) The first 67% of the unloading portion is shown in columns AA & AB.

(v) Button "Powerlaw" allows the user to perform additional power-law fit to the first 67% of the unloading

(vi) The remaining 23% of the unloading portion is shown in columns AK & AL.

(vii) Button "Overwrite" allows the user to directly input the value of indentation characteristics (C, $\frac{W_\mathrm{p}}{W_\mathrm{t}}$, $\frac{\mathrm{d}P}{\mathrm{d}h}\big|_{h_\mathrm{m}}$ and P_m) into the range (AS14:AS18). Button "ClearOverwrite" is designed to clear the range (AS14:AS18).

4. Next step of reverse analysis is to allow for a visual check of the fits for both loading and unloading portion. Fig. B-1(f) is magnified and shown in Fig. B-8 with the following details.

   (i) Button "Proceed" allows the analysis to proceed to the next step (worksheet "ReverseAnalysis," as shown in Fig. B-9).

5. Next step of reverse analysis is the main calculation of ($E^*, p_\mathrm{ave}, \sigma_\mathrm{r}, \sigma_\mathrm{y}$ and n) from (C, $\frac{W_\mathrm{p}}{W_\mathrm{t}}$, $\frac{\mathrm{d}P}{\mathrm{d}h}\big|_{h_\mathrm{m}}$) gathered in the previous worksheets. Fig. B-1(g) is magnified and shown in Fig. B-9 with the following details.

   (i) Button "SolveReverse" allows for the automatic execution of the reverse algorithms (Figs. 2-13 and 3-5). Button "ExportReverse" allows the prediction of material's elasto-plastic properties to be exported to the next worksheet as a single row (useful for batch calculation).

   (ii) The input region for elastic properties of the indenter tip ($E_\mathrm{i} and \nu_\mathrm{i}$), the tip index (Berkovich or Vickers) and estimate of material's poisson ratio (ν_i).

   (iii) The input region showing indentation characteristics (C, $\frac{W_\mathrm{p}}{W_\mathrm{t}}$, $\frac{\mathrm{d}P}{\mathrm{d}h}\big|_{h_\mathrm{m}}$) gathered in the previous worksheets. The radial crack length can be entered at cell "C19" for fracture toughness estimation.

   (iv) The output region for elasto-plastic properties of the material (E^*, E, p_ave, σ_r, σ_y and n) from various methodology.

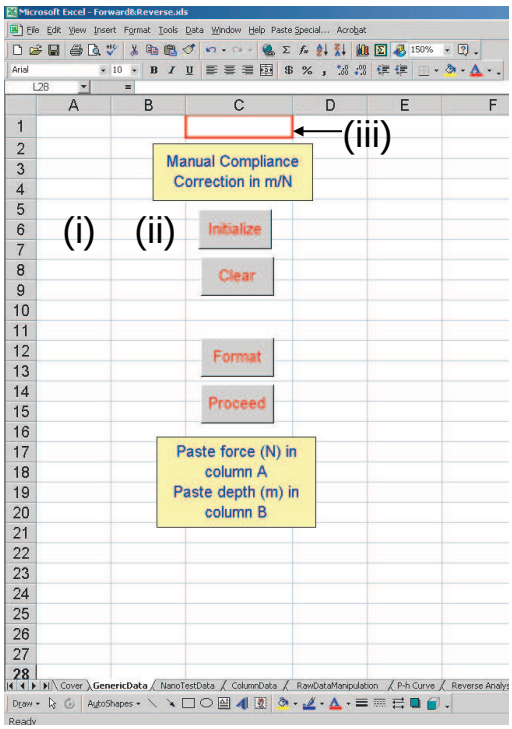

Figure B-4: Zoom in of Fig. B-1(c1) showing the worksheet "GenericData" of the Macro program

(v) Button "UnstressedMat'l" is similar to button "SolveReverse" except that the program remembers the results as the reference for residual stress calculation. Button "StressedMat'l" should be executed after the stressed indentation curve has been analyzed from Figs. B-1(c) to B-1(f). The determination of residual stress is shown at cell "BG11" of the next worksheet ("RevMultiple").

(vi) Button "Vickers/Berkovich" is similar to button "SolveReverse" except that the program remembers the results as the reference for dual reverse algorithms. Button "2nd indenter" should be executed after the 60^o cone indentation curve has been analyzed from Figs. B-1(c) to B-1(f). The plastic properties from dual indenter algorithms are shown at the range (K14:K16).

(vii) The predicted stress-strain curve from the reverse algorithm.

6. The results from reverse analysis are summarized within a single row for each indentation curve, as shown in Fig. B-1(h) or magnified in Fig. B-10.

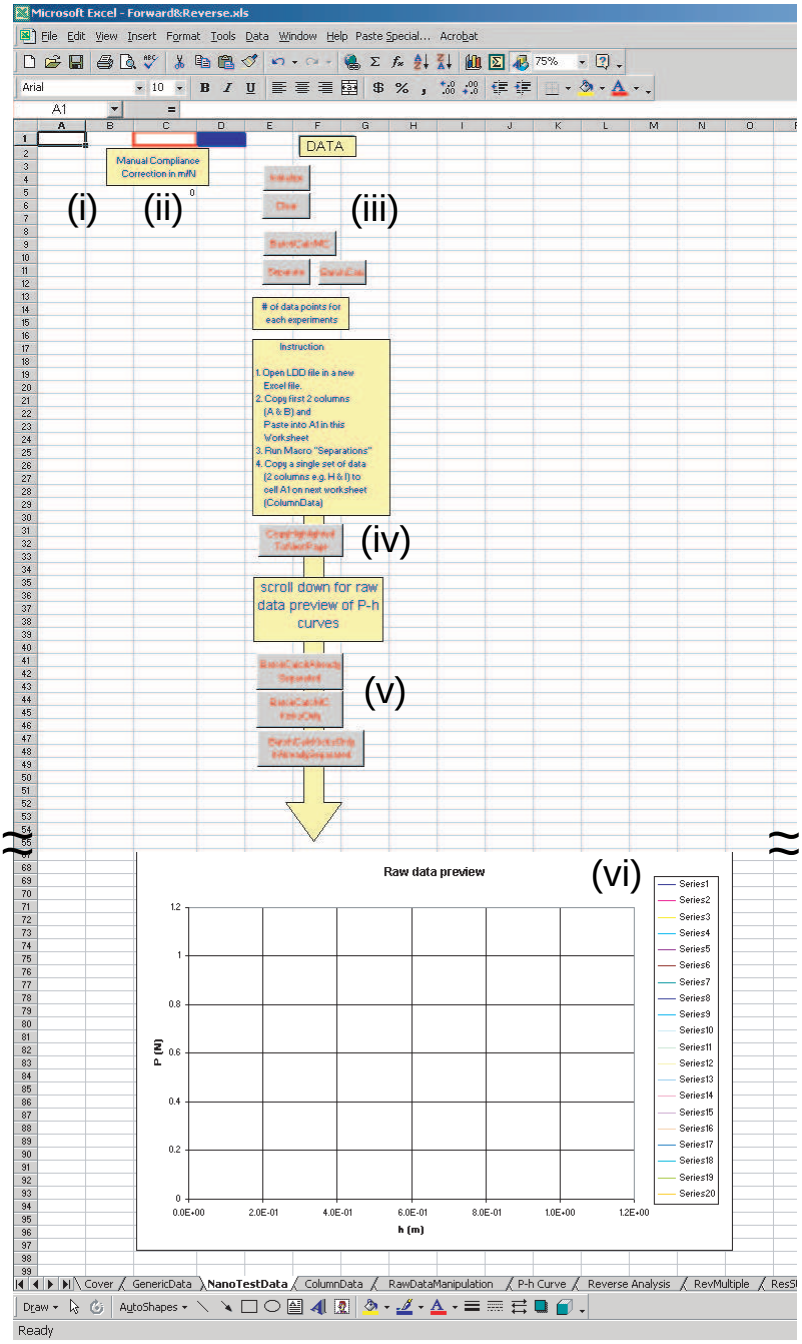

Figure B-5: Zoom in of Fig. B-1(c2) showing the worksheet "NanoTestData" of the Macro program

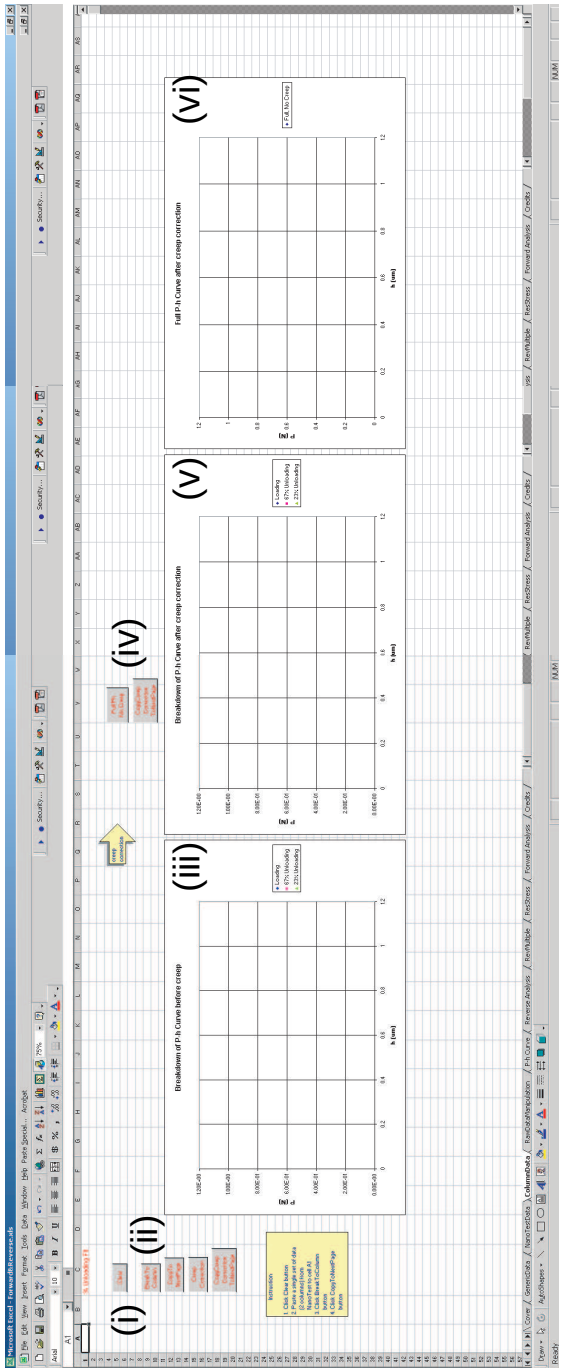

Figure B-6: Zoom in of Fig. B-1(d) showing the worksheet "ColumnData" of the Macro program

Figure B-7: Zoom in of Fig. B-1(e) showing the worksheet "RawDataManipulation" of the Macro program

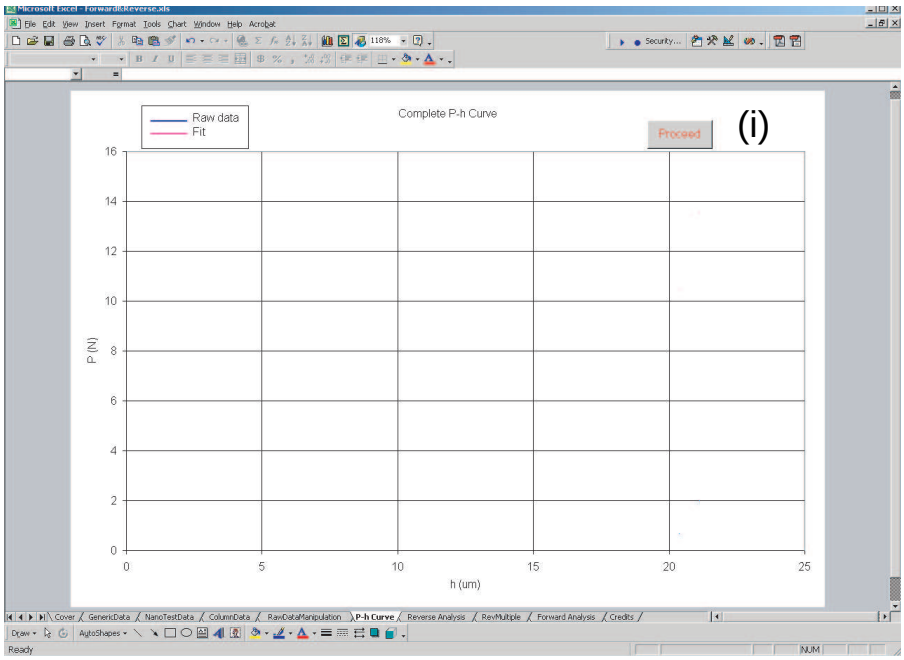

Figure B-8: Zoom in of Fig. B-1(f) showing the worksheet "P-h Curve" of the Macro program

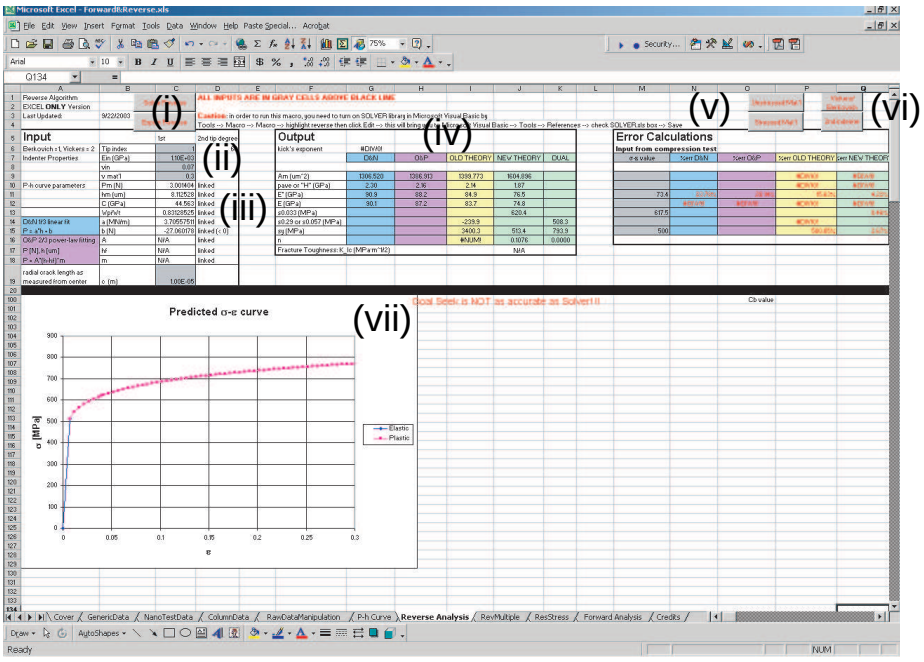

Figure B-9: Zoom in of Fig. B-1(g) showing the worksheet "Reverse Analysis" of the Macro program

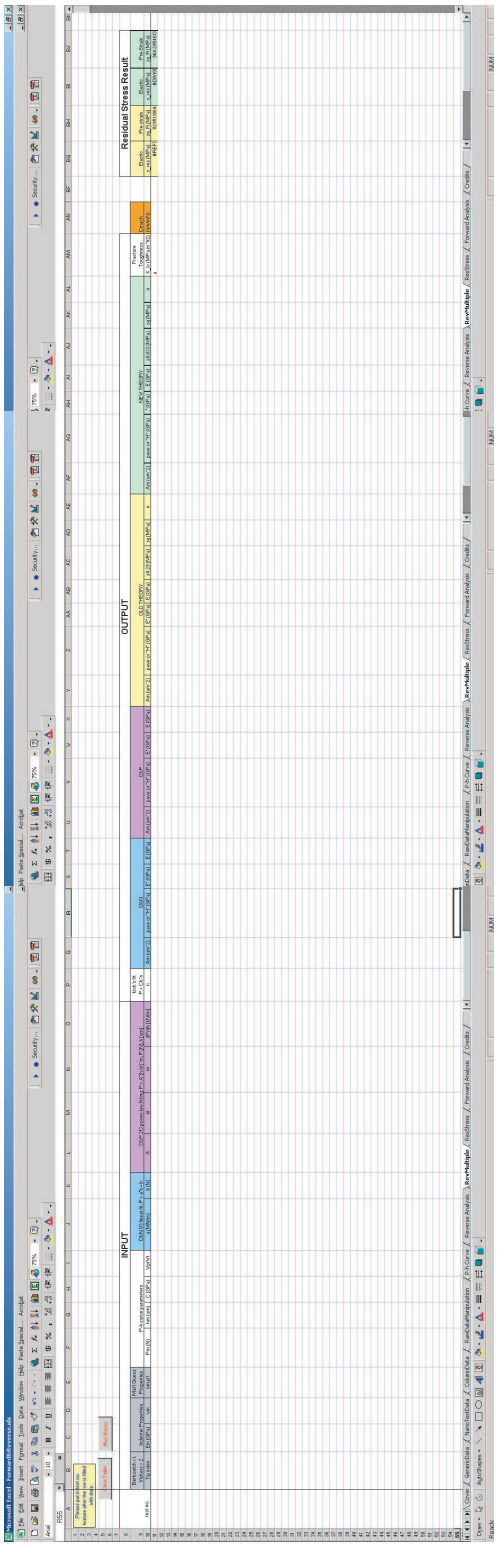

Figure B-10: Zoom in of Fig. B-1(h) showing the worksheet "RevMultiple" of the Macro program

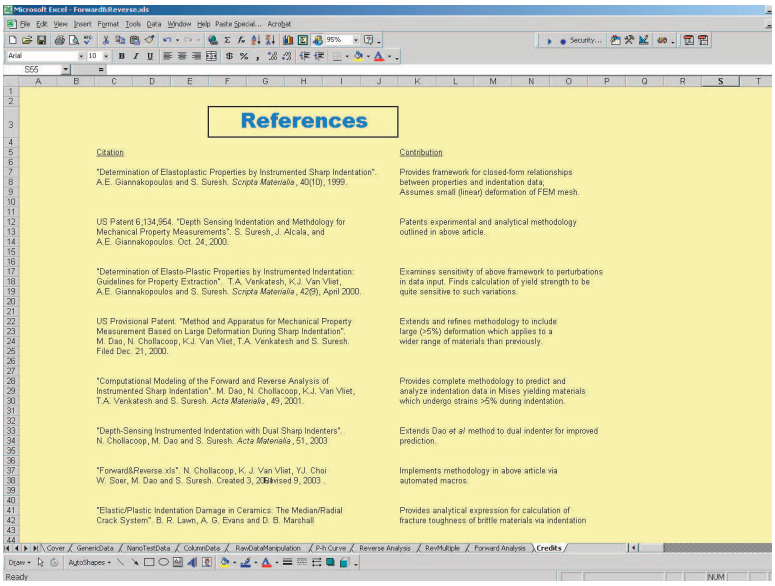

Figure B-11: Zoom in of Fig. B-1(i) showing the worksheet "Credits" of the Macro program

Bibliography

[1] Sneddon, I.N., Int. J. Eng. Sci., 1965, 3, 47.

[2] Hill, R., Storakers, B., and Zdunek, A.B., Proc. R. Soc. London Ser. A-Math. Phys. Eng. Sci., 1989. 423(1865): p. 301-330.

[3] Giannakopoulos, A.E., Larsson, P.L., and Vestergaard, R., Int. J. Solids Struct., 1994. 31(19): p. 2679-2708.

[4] Larsson, P.L., Giannakopoulos, A.E., Soderlund, E., Rowcliffe, D.J., and Vestergaard, R., Int. J. Solids Struct., 1996. 33(2): p. 221.

[5] Sanders, P.G., Eastman, J.A., and Weertman, J.R., Acta Mater., 1997. 45(10): p. 4019-4025.

[6] Ebrahimi, F., Zhai, Q. and Kong, D., Scripta Mater., 1998, 39, 315.

[7] Lu, L., Li, S.X., and Lu, K., Scripta Materialia, 2001. 45(10): p. 1163-1169.

[8] Dalla Torre, F., Van Swygenhoven, H., and Victoria, M., Acta Materialia, 2002. 50(15): p. 3957-3970.

[9] Ebrahimi, F., Bourne, G.R., Kelly, M.S. and Matthews, T.E., Nanost. Mater., 1999, 11, 343.

[10] Weertman, J.R., Mechanical Behaviour of Nanocrystalline Metals in Nanostructured Materials: Processing, Properties, and Potential Applications. (William Andrew Publishing, Norwich, 2002).

[11] Legros, M., Elliott, B.R., Rittner, M.N., Weertman, J.R. and Hemkar, K.J., Philos. Mag. A, 2000, 80, 1017-1026.

[12] Wang, Y.M., Wang, K., Pan, D., Lu, K., Hemker, K.J., and Ma, E., Scripta Mat., 2003, 48 1581.

[13] Wang, N., Wang, Z., Aust, K.T., and Erb, U., Materials Science and Engineering A, 1997. 237(2): p. 150-158.

[14] Lu, L., Sui, M.L., and Lu, K., Science, 2000. 287(5457): p. 1463-1466.

[15] Mukai, T., Suresh, S., Kita, K., Sasaki, H., Kobayashi, N., Higashi, K., and Inoue, A., Acta Mater., 2003, 51, 4197.

[16] Schwaiger, R., Moser, B., Dao, M., Chollacoop, N., and Suresh, S., Acta Mater., 2003. 51(17): p. 5159-5172.

[17] Mirshams, R.A., Xiao, C.H., Whang, S.H. and Yin, W.M., Mater. Sci. and Eng. A 2001, 315, 21.

[18] Agnew, S.R., and Weertman, J.R., Mater. Sci. and Eng. A 1998, A244, 145.

[19] Agnew, S.R., Vinogradov, A.Y., Hashimoto, S. and Weertman, J.R., Jour. of Elec. Mater., 1999, 28, 1038.

[20] Mughrabi, H. and Höppel, H.W., Mater. Res. Symp. Proc., 2001, vol. 634, B2.1.1.

[21] Hanlon, T., Kwon, Y.-N., and Suresh, S., Scripta Mater., 2003, 49, 675.

[22] Dao, M., Chollacoop, N., Van Vliet, K.J., Venkatesh, T.A., and Suresh, S., Acta Mater., 2001. 49(19): p. 3899-3918.

[23] Tabor, D. Hardness of Metals, (Clarendon Press, Oxford, 1951).

[24] Tabor, D. Rev. Phys. Technol 1, 145 (1970).

[25] Doener, M.F. and Nix, W.D., J. Mater. Res., 1986. 1: p. 601.

[26] Pharr, G.M. and Cook, R.F., J. Mater. Res., 1990. 5(4): p. 847-851.

[27] Oliver, W.C. and Pharr, G.M., J. Mater. Res., 1992. 7(6): p. 1564-1583.

[28] Field, J.S. and Swain, M.V., J. Mater. Res., 1993. 8(2): p. 297-306.

[29] Field, J.S. and Swain, M.V., J. Mater. Res., 1995. 10(1): p. 101-112.

[30] Gerberich, W.W., Nelson, J.C., Lilleodden, E.T., Anderson, P., and Wyrobek, J.T., Acta Mater., 1996. 44(9): p. 3585-3598.

[31] Bolshakov, A., Oliver, W.C., and Pharr, G.M., J. Mater. Res., 1996. 11(3): p. 760-768.

[32] Alcala, J., Giannakopoulos, A.E., and Suresh, S., J. Mater. Res., 1998. 13(5): p. 1390-1400.

[33] Cheng, Y.T. and Cheng, C.M., J. Appl. Phys., 1998. 84(3): p. 1284-1291.

[34] Cheng, Y.T. and Cheng, C.M., Appl. Phys. Lett., 1998. 73(5): p. 614-616.

[35] Suresh, S., Nieh, T.G., and Choi, B.W., Scr. Mater., 1999. 41(9): p. 951-957.

[36] Gouldstone, A., Koh, H.J., Zeng, K.Y., Giannakopoulos, A.E., and Suresh, S., Acta Mater., 2000. 48(9): p. 2277-2295.

[37] Johnson, K.L., J. Mech. Phys. Solids, 1970. 18: p. 115.

[38] Suresh, S., Alcala, J., and Giannakopoulos, A.E., US Patent No. 6,134,954, Date of Issue: October 24, 2000.

[39] Dao, M., Chollacoop, N., Van Vliet, K.J., Venkatesh, T.A., and Suresh, S., "Systems and Methods for Estimation and Analysis of Mechanical Property Data Associated with Indentation Testing," US Patent, filed with the US Patent Office on March 7, 2002.

[40] Cheng, Y.T. and Cheng, C.M., J. Mater. Res., 1999. 14(9): p. 3493-3496.

[41] Giannakopoulos, A.E. and Suresh, S., Scr. Mater., 1999. 40(10): p. 1191-1198.

[42] Venkatesh, T.A., Van Vliet, K.J., Giannakopoulos, A.E., and Suresh, S., Scr. Mater., 2000. 42(9): p. 833-839.

[43] Suresh, S. and Giannakopoulos, A.E., Acta Mater., 1998. 46(16): p. 5755-5767.

[44] Suresh, S. and Giannakopoulos, A.E., US Patent No. 6,155,104, Date of Issue: December 5, 2000.

[45] Bhattacharya, A.K. and Nix, W.D., Int. J. Solids Struct., 1988. 24(9): p. 881-891.

[46] Laursen, T.A. and Simo, J.C., J. Mater. Res., 1992. 7(3): p. 618-626.

[47] Tunvisut, K., O'Dowd, N.P., and Busso, E.P., Int. J. Solids Struct., 2001. 38(2): p. 335-351.

[48] Chaudhri, M.M., Acta Mater., 1998. 46(9): p. 3047-3056.

[49] Johnson, K.L., Contact Mechanics. 1985, London: Cambridge University Press.

[50] Fleck, N.A. and Hutchinson, J.W., J. Mech. Phys. Solids, 1993. 41(12): p. 1825-1857.

[51] Gao, H., Huang, Y., Nix, W.D., and Hutchinson, J.W., J. Mech. Phys. Solids, 1999. 47(6): p. 1239-1263.

[52] ABAQUS Theory Manual Version 6.1. Hibbitt, Karlsson and Sorensen Inc, Pawtucket 2000.

[53] King, R.B., Int. J. Solids Struct., 1987. 23(12): p. 1657-1664.

[54] MatWeb: http://www.matweb.com, 2001, by Automation Creations, Inc.

[55] Cheng, Y.T. and Cheng, C.M., Philos. Mag. Lett., 1998. 78(2): p. 115-120

[56] Chaudhri,M.M., and Winter,M., J. Phys. D, 1988, 21, 370.

[57] Bec, S., Tonck, A., Georges, J.-M., Georges, E., and Loubet, J.-L., Phil. Mag. A, 1996, 74, 1061.

[58] Ashby, M.F., Materials Selection in Mechanical Design. 1999, Boston: Butterworth Heinemann.

[59] Chollacoop, N., Dao, M., and Suresh, S., Acta Mater., 2003. 51(13): p. 3713-3729.

[60] Chollacoop, N., Dao, M., and Suresh, S., "Depth-Sensing Instrumented Indentation with Dual Sharp Indenters," US Provisional Patent, filed with the US Patent Office on October 31, 2002

[61] Bucaille, J.L., Stauss, S., Felder, E., and Michler, J., Acta Mater., 2003. 51(6): p. 1663-1678.

[62] Zeng, K., Soderlund, E., Giannakopoulos, A.E. and Rowcliffe, D.J., Acta Mater., 1996. 44(3): p. 1127-1141

[63] Suryanarayana, C., Int. Mater. Rev., 1995. 40(2): p. 41-64.

[64] Gleiter, H., Prog. Mater. Sci., 1989. 33(4): p. 223-315.

[65] Masumura, R.A., Hazzledine, P.M., and Pande, C.S., Acta Mater., 1998. 46(13): p. 4527-4534.

[66] Farhat, Z.N., Ding, Y., Northwood, D.O., and Alpas, A.T., Mater. Sci. Eng. A, 1996: p. 302-313.

[67] Jeong, D.H., Gonzalez, F., Palumbo, G., Aust, K.T., and Erb, U., Scripta Materialia, 2001. 44(3): p. 493-499.

[68] McFadden, S.X., Mishra, R.S., Valiev, R.Z., Zhilyaev, A.P., and Mukherjee, A.K., Nature, 1999. 398(6729): p. 684-686.

[69] Mayo, M.J., Siegel, R.W., Narayanasamy, A., and Nix, W.D., Journal of Materials Research, 1990. 5(5): p. 1073-1082.

[70] Mayo, M.J., Siegel, R.W., Liao, Y.X., and Nix, W.D., Journal of Materials Research, 1992. 7(4): p. 973-979.

[71] Yamakov, V., Wolf, D., Phillpot, S.R., and Gleiter, H., Acta Materialia, 2002. 50(1): p. 61-73.

[72] Schiotz, J., Vegge, T., Di Tolla, F.D., and Jacobsen, K.W., Physical Review B (Condensed Matter), 1999. 60(17): p. 11971-11983.

[73] Fu, H.-H., Benson, D.J., and Meyers, M.A., Acta Materialia, 2001. 49(13): p. 2567-2582.

[74] Carsley, J.E., Ning, J., Milligan, W.W., Hackney, S.A., and Aifantis, E.C., Nanostructured Materials, 1995. 5(4): p. 441-448.

[75] Hall, E.O., Proc. Phys. Soc., 1951. B64: p. 747.

[76] Petch, N.J., J. Iron. Steel Inst., 1953. 174: p. 25.

[77] Sanders, P.G., Youngdahl, C.J., and Weertman, J.R., Mater. Sci. Eng. A-Struct. Mater. Prop. Microstruct. Process., 1997. 234: p. 77-82.

[78] Witney, A.B., Sanders, P.G., Weertman, J.R., and Eastman, J.A., Scr. Metall. Materialia, 1995. 33(12): p. 2025-2030.

[79] Cheung, C., Djuanda, F., Erb, U., and Palumbo, G., Nanostruct. Mater., 1995. 5(5): p. 513-523.

[80] Chokshi, A.H., Rosen, A., Karch, J., and Gleiter, H., Scripta Metallurgica, 1989. 23(10): p. 1679-1683.

[81] Conrad, H. and Narayan, J., Appl. Phys. Lett., 2002. 81(12): p. 2241-2243.

[82] Takeuchi, S., Scr. Mater., 2001. 44(8-9): p. 1483-1487.

[83] Chattopadhyay, P.P., Pabi, S.K., and Manna, I., Z. Metallk., 2000. 91(12): p. 1049-1051.

[84] Zaichenko, S.G. and Glezer, A.M., Interface Sci., 1999. 7(1): p. 57-67.

[85] Volpp, T., Goring, E., Kuschke, W.M., and Arzt, E., Nanostruct. Mater., 1997. 8(7): p. 855-865.

[86] Schuh, C.A., Nieh, T.G., and Yamasaki, T., Scr. Mater., 2002. 46(10): p. 735-740.

[87] Schuh, C.A., Nieh, T.G., and Iwasaki, H., Acta Mater., 2003. 51(2): p. 431-443.

[88] Jeong, D.H., Erb, U., Aust, K.T., and Palumbo, G., Scr. Mater., 2003. 48(8): p. 1067-1072.

[89] Lucas, B.N. and Oliver, W.C., Metallurgical and Materials Transactions A (Physical Metallurgy and Materials Science), 1999. 30A(3): p. 601-610.

[90] Pethica, J.B. and Oliver, W.C., Thin Films: Stresses and Mechanical Properties Symposium, 1989: p. 13-23.

[91] Feng, G. and Ngan, A.H.W., J Materials Research, 2002. 17(3): p. 660-668.

[92] Kumar, K.S., Suresh, S., Chisholm, M.F., Horton, J.A., and Wang, P., Acta Materialia, 2003. 51(2): p. 387-405.

[93] Ranganathan, S., Divakar, R., and Raghunathan, V.S., Scripta Materialia, 2001. 44(8-9): p. 1169-1174.

[94] Ke, M., Hackney, S.A., Milligan, W.W., and Aifantis, E.C., Nanostructured Materials, 1995. 5(6): p. 689-697.

[95] Hackney, S.A., Ke, M., Milligan, W.W., and Aifantis, E.C., Processing and Properties of Nanocrystalline Materials; Published by Minerals, Metals and Materials Soc (TMS), 1996: p. 421-426.

[96] Youngdahl, C.J., Hugo, R.C., Kung, H., and Weertman, J.R., Structure and Mechanical Properties of Nanophase Materials - Theory and Computer Simulation vs. Experiment. Symposium (Materials Research Society Symposium Proceedings Vol.634), 2001: p. PageB1.2.1-5.

[97] Youngdahl, C.J., Weertman, J.R., Hugo, R.C., and Kung, H.H., Scripta Materialia, 2001. 44(8-9): p. 1475-1478.

[98] Keblinski, P., Wolf, D., Phillpot, S.R., and Gleiter, H., Scripta Materialia, 1999. 41(6): p. 631-636.

[99] Van Swygenhoven, H., Spaczer, M., Caro, A., and Farkas, D., Physical Review B (Condensed Matter), 1999. 60(1): p. 22-25.

[100] Kim, H.S., Estrin, Y., and Bush, M.B., Acta Materialia, 2000. 48(2): p. 493-504.

[101] Cullity, B.D., Elements of X-ray diffraction. 1956, Reading, MA: Addison-Wesley Publishing Company, Inc.

[102] Van Swygenhoven, H., Caro, A., and Farkas, D., Materials Science and Engineering A, 2001. 309-310: p. 440-444.

[103] Thompson, A.W., Acta Metallurgica, 1977. 25(1): p. 83-86.

[104] Meyers, M.A. and Chawla, K.K., Mechanical Metallurgy. 1984, Prentice-Hall, Inc.: New Jersey. p. 495.

[105] Hughes, G.D., Smith, S.D., Pande, C.S., Johnson, H.R., and Armstrong, R.W., Scripta Metallurgica, 1986. 20(1): p. 93-97.

[106] Elsherik, A.M., Erb, U., Palumbo, G., and Aust, K.T., Scr. Metall. Materialia, 1992. 27(9): p. 1185-1188.

[107] Benson, D.J., Fu, H.H., and Meyers, M.A., Mater. Sci. Eng. A-Struct. Mater. Prop. Microstruct. Process., 2001. 319: p. 854-861.

[114] Kim, H.S., Suryanarayana, C., Kim, S.J., and Chun, B.S., Powder Metall., 1998. 41(3): p. 217-220.

[109] Kim, H.S., Bush, M.B., and Estrin, Y., Mater. Sci. Eng. A-Struct. Mater. Prop. Microstruct. Process., 2000. 276(1-2): p. 175-185.

[110] Kim, H.S., Estrin, Y., and Bush, M.B., Mater. Sci. Eng. A-Struct. Mater. Prop. Microstruct. Process., 2001. 316(1-2): p. 195-199.

[111] Palumbo, G., Thorpe, S.J., and Aust, K.T., Scr. Metall. Materialia, 1990. 24(7): p. 1347-1350.

[112] Song, H.W., Guo, S.R., and Hu, Z.Q., Nanostruct. Mater., 1999. 11(2): p. 203-210.

[113] Kim, H.S. and Bush, M.B., Nanostruct. Mater., 1999. 11(3): p. 361-367.

[114] Kim, H.S., Scr. Mater., 1998. 39(8): p. 1057-1061.

[115] Lawn, B.R., Evans, A.G., and Marshall, D.B., J. Am. Ceram. Soc., 1980. 63(9-10): p. 574-581.

[116] Lawn, B. and Wilshaw, R., J. Mater. Sci., 1975. 10(6): p. 1049-1081.

[117] Evans, A.G. and Wilshaw, T.R., Acta Metallurgica, 1976. 24(10): p. 939-956.

[118] Evans, A.G. and Charles, E.A., J. Am. Ceram. Soc., 1976. 59(7-8): p. 371-372.

[119] Lawn, B.R. and Evans, A.G., J. Mater. Sci., 1977. 12(11): p. 2195-2199.

[120] Marshall, D.B. and Lawn, B.R., J. Mater. Sci., 1979. 14(8): p. 2001-2012.

[121] Anstis, G.R., Chantikul, P., Lawn, B.R., and Marshall, D.B., J. Am. Ceram. Soc., 1981. 64(9): p. 533-538.

[122] Chiang, S.S., Marshall, D.B., and Evans, A.G., J. Appl. Phys., 1982. 53(1): p. 298-311.

[123] Chiang, S.S., Marshall, D.B., and Evans, A.G., J. Appl. Phys., 1982. 53(1): p. 312-317.

[124] Marshall, D.B., Lawn, B.R., and Evans, A.G., J. Am. Ceram. Soc., 1982. 65(11): p. 561-566.

[125] Marshall, D.B., J. Am. Ceram. Soc., 1983. 66(2): p. 127-131.

[126] Cook, R.F., Pascucci, M.R., and Rhodes, W.H., J. Am. Ceram. Soc., 1990. 73(7): p. 1873-1878.

[127] Cook, R.F. and Pharr, G.M., J. Am. Ceram. Soc., 1990. 73(4): p. 787-817.

[128] Lawn, B.R., Deng, Y., Miranda, P., Pajares, A., Chai, H., and Kim, D.K., J. Mater. Res., 2002. 17(12): p. 3019-3036.

[129] Field, J.S., Swain, M.V., and Dukino, R.D., J. Mater. Res., 2003. 18(6): p. 1412-1419.

[130] Kruzic, J.J. and Ritchie, R.O., J. Am. Ceram. Soc., 2003. 86(8): p. 1433-1436.

[131] Carlsson, S. and Larsson, P.L., Acta Mater., 2001. 49(12): p. 2179-2191.

[132] Carlsson, S. and Larsson, P.L., Acta Mater., 2001. 49(12): p. 2193-2203.

[133] Larsson, P.L., Int. J. Mech. Sci., 2001. 43(4): p. 895-920.